COMMUNAUTÉ FRANÇAISE DE BELGIQUE
UNIVERSITÉ DE LIÈGE - GEMBLOUX AGRO BIO-TECH

CASE OF A HYDRAULIC SPLASHING NOZZLE: EFFECT OF THE DISK GEOMETRY ON THE SHEET BREAKUP

Sofiene Ouled Taleb Salah

Dissertation originale présentée en vue de l'obtention du grade de docteur en sciences agronomiques et ingénierie biologique

Supervisors: Stéphane Dorbolo
Frédéric Lebeau

2018

Declaration of Authorship

I, Sofiene Ouled Taleb Salah, declare that this thesis titled, CASE OF A HYDRAULIC SPLASHING NOZZLE: EFFECT OF THE DISK GEOMETRY ON THE SHEET BREAKUP and the work presented in it are my own. I confirm that:

- This work was done wholly or mainly while in candidature for a research degree at this University.
- Where any part of this thesis has previously been submitted for a degree or any other qualification at this University or any other institution, this has been clearly stated.
- Where I have consulted the published work of others, this is always clearly attributed.
- Where I have quoted from the work of others, the source is always given. With the exception of such quotations, this thesis is entirely my own work.
- I have acknowledged all main sources of help.
- Where the thesis is based on work done by myself jointly with others, I have made clear exactly what was done by others and what I have contributed myself.

Sofiene Ouled Taleb Salah

Abstract

In the agricultural field, conventional farmers use Plant Protection Products (PPP) to control crop enemies as for instance weeds, diseases and pests. In practice, PPP application techniques are based on droplet clouds to carry the spray mixture containing the active ingredient and the adjuvant to the surface target. The PPP application efficiency consists in maximizing the deposition of the mixture on the target while reducing the environmental losses. However, the droplet characteristics within the spray affect drastically the treatment efficiency. For instance, small droplets ($< 200\ \mu$m) are prone to drift while big droplets ($> 300\ \mu$m) have the tendency to splash on a specific target surface. The widely used agricultural nozzles produce a liquid sheet (using the pressure) that disintegrates into ligaments leading to droplets with various diameters and velocities. Hence, the generated spray is characterized by a wide droplet size distribution ($RSF = 1$) resulting in potential drifting or efficiency losses due to splashing phenomena. The spray must deliver an optimal droplet distribution in term of diameters and velocities by reducing the extent of the droplet size distribution. The design of new agricultural nozzles is a challenge for the practitioners in the field of agricultural nozzles.

As the simplicity, the robustness, the low cost and the high flow rate ranges are required for the agronomic application, the Savart configuration namely a round jet impacting vertically a motionless disk is the ideal candidate for the massive production of droplets. The Savart sheet develops in the air (outside the disk) and it results in random breakup leading to wide droplet size distribution as in the case in hydraulic nozzles. As the used flow ranges are high in the PPP application, the obtained sheet on the disk is turbulent. The challenge is to tame the turbulent sheet. I propose to split the sheet into individual jets using textured disks by acting on the semi-free film or by inserting the right structures directly in the free sheet. Then, the jets break up according the Plateau-Rayleigh mechanism and lead to a narrower droplet size distribution. Therefore, this thesis aims to study

experimentally the effect of the disk geometry on the sheet break up. This study is seen as a practical guide for specialists in fluid mechanics who desire developing the generation of drops with controlled sizes.

In the chapter 1, one firstly establishes an overview of the challenges facing the PPP application with respect to the efficiency and the environmental sides. Then, one detailed the configuration of Savart that will be adopted in the present thesis. One also focused on the techniques used to create local disturbances in the sheet and to control its shape and its dynamics.

In the chapter 2, one detailed the experimental setup based on the impact of a turbulent jet on a non-textured disk. The disk configuration constitutes our reference case to which results on textured disks are to be confronted. The sheet was characterized through several parameters: The mean velocity U, the mean thickness h and the ejection angle ϕ that depends on the disk geometry and on the flow rate Q. For low Q values, the sheet is subject to gravity and it adopts a closed / semi-opened bell. As Q increases, the water bell progressively opens because of the inertia. As the jet flow is turbulent at the impact, local disturbances in the film triggered downstream the disk edge the appearance of random holes at a distance R' (from the jet axis) in the liquid sheet. These holes amplified and lead to the disintegration of the sheet into droplets. Furthermore, the produced droplets are characterized in term of diameters. The droplet size distribution is clearly wide (RSF values are close to 1) that is similar to the case of hydraulic nozzles.

In the chapter 3, one perturbed the semi-free film evolving on the disk surface. The case of a turbulent round water jet impacting a disk engraved along its circumference by a number N of radial grooves is addressed. By the insertion of grooves, one controls the turbulent flow and the film splits into a number n of liquid jets before reaching the disk edge. The phase diagrams presented as a function of the inside gap between grooves $d1$ and the flow rate Q illustrate the transition between jet regimes: $n = 2N$, $n = N_1^*$, $n = N$ and $n = N_2^*$. The jet number n can either be stable as in the case of $n = 2N$ and $n = N$ or unstable as in the case of $n = N_1^*$ and $n = N_2^*$. The $n = N$ regime is found when $d1$ is close to the capillary length. In the case of $n = 2N$, the jets are emitted in two different planes what permits to avoid jet coalescences. The regimes $n = N_1^*$ and $n = N_2^*$ are characterized by the elastic merging of jets. The reduction of the groove length L generates a large number of jets. However, it increases elastic coalescences between main and secondary jets. The droplets were characterized in term of their diameters and velocities. For all configurations

including an engraved disk, the obtained droplet size distribution is narrower compared to the ungraved disk and to the standard flat fan nozzle Teejet TP 65 15. The V_{50} is reduced towards smaller droplets in the case of the engraved disk configurations but it is still coarse compared to that of the Teejet nozzle. With the current designs (L = 5 mm), only 72 jets are generated over 360° that are too little compared to agricultural requirements in term of jet numbers (= 111 jets corresponding to a Q = 1.66 10^{-5} $m^3.s^{-1}$). In practice, one may increase the jet number either by reducing the width of the groove or by increasing the radial distance from the inlet. However, in the latter case, one is facing to the quick flow deceleration induced by the surface friction.

In the chapter 4, one perturbed directly the Savart sheet, i.e. the free sheet evolves in the air. A number N of triangular prisms are set in the sheet at a radial distance R_p from the jet axis. This radial distance is strictly greater than $\frac{D}{2}$ (D = disk diameter) and less than or equal to R' (for which the holes appear in the sheet). Once the number of prisms N and the distance from the injector is fixed, the geometry is determined by the size of the prism and the distance b between two successive prisms. When increasing the flow rate Q, the jet numbers are n = 0 (for low Q where the sheet does not impact the textures), $n = N$ and $n = N^*$ (elastic coalescence of jets) for large Q. One used a geometrical model that explains the generation of individual jets through these structures. Then, the emitted droplets are characterized in term of diameters and velocities. The droplet size distribution is narrower compared to the non-textured disk and the hydraulic nozzle TP 65 15 with the same spray class. The V_{50} decreased by decreasing the external gap b between two neighboring textures at the same radial distance R_p from the jet axis. Also, the V_{50} decreased by increasing the radial distance from the jet axis as the sheet thickness decreases $\frac{a^2}{2r}$ (a = the jet radius). However, we are limited by R' due to holes appearances that trig the disintegration of the sheet. With the current design, the droplet size distribution is narrow with a V_{50} close to 500 μm and droplet velocities are 4 $m.s^{-1}$. The generated jets are 140 over 360° that is better than in the case of the engraved disks. The present methodology is a promising alternative as one reduces the flow deceleration and increases the jet numbers.

In the chapter 5, one discussed the disk configurations used to taylor the turbulent sheet and to split it individual jets and their performance to meet the agronomic objective in term of droplet diameters and velocities and jet numbers.

Finally, the chapter 6 concludes on the fundamental findings and on the role that the developed nozzle could play in applications. Also, one proposed some original perspectives to the present thesis such as testing the triangular prism textures in the case of the liquid sheet produced by a standard hydraulic nozzle.

Résumé

Dans le domaine agricole, l'usage des produits phytopharmaceutiques (PPP) reste privilégié par les agriculteurs conventionnels pour le contrôle des nuisibles notamment les adventices, les maladies et les ravageurs. En pratique, les techniques d'application de PPP sont basées sur l'utilisation d'un nuage de gouttes pour transporter la bouillie agricole contenant la matière active et l'adjuvant vers la surface cible. L'efficacité de l'application des PPP consiste à maximiser les dépôts sur la cible tout en réduisant les pertes environnementales. Cependant, les caractéristiques des gouttes affectent drastiquement l'efficacité du traitement. Par exemple, les petites gouttes de diamètres $<$200 μm sont sensibles à la dérive tandis que les grosses gouttes de diamètre $>$ 300 μm ont tendance à se fragmenter sur les surfaces cibles. Les buses hydrauliques agricoles se servent de la pression pour générer une nappe liquide qui se désintègre en ligaments, conduisant à des gouttes ayant différents diamètres et vitesses. Par conséquent, le spray généré est caractérisé par une large distribution de taille des gouttes (RSF = 1), ce qui entraîne des pertes potentielles sous forme de dérive ou d'efficacité dues aux fragmentations. Aussi, le spray doit être caractérisé par une distribution optimale de tailles des gouttes en termes de diamètres et de vitesses tout en réduisant l'étendue de cette distribution. La conception de nouvelles buses agricoles constitue un défi pour les praticiens dans le domaine des buses agricoles.

Comme la simplicité, la robustesse, le faible coût et les débits élevés sont des éléments exigés par l'application de PPP, la configuration de Savart, qui consiste en un jet impactant verticalement un disque fixe, est le dispositif idéal pour la production massive de gouttes. La nappe de Savart se développe dans l'air (à l'extérieur du disque). Elle se rompt d'une maniére aléatoire pour générer un nuage de gouttes caractérisé par une large distribution des tailles, similaire à celle obtenue dans le cas des buses hydrauliques. Comme

l'application PPP exige des débits élevés, la nappe liquide obtenue est naturellement turbulente. Le défi est de contrôler cette nappe turbulente. Je propose d'induire la fragmentation en jets individuels à l'aide des structures additionnelles sur le disque ou directement placées dans la nappe de Savart. Les jets ainsi créés se rompent selon le mécanisme de Plateau-Rayleigh et conduisent à une distribution plus étroite de la taille des gouttelettes. Cette thèse vise à étudier expérimentalement l'effet de la géométrie du disque sur la rupture de la nappe liquide. Ce travail peut être considéré comme un guide pratique pour les spécialistes de la mécanique des fluides qui veulent développer la production de gouttes de tailles contrôlées à partir d'un dispositif simple et robuste.

Dans le chapitre 1, on montre une vue d'ensemble des défis auxquels l'application des PPP est confrontée en matière d'efficacité et d'exigences environnementales. Ensuite, on a détaillé la configuration de Savart qui a été adoptée dans la présente thèse. L'accent a été également mis sur les techniques utilisées pour créer des perturbations locales dans la nappe et pour contrôler sa forme et sa dynamique.

Dans le chapitre 2, le dispositif expérimental est détaillé. Il est basé sur l'impact d'un jet turbulent sur un disque non texturé. La configuration du disque non texturé constitue notre cas de référence auquel les résultats ultérieurs sont confrontés. La nappe liquide a été caractérisée par plusieurs paramètres: la vitesse moyenne U, l'épaisseur moyenne h et l'angle d'éjection ϕ qui dépend de la géométrie du disque et du débit Q. Pour des débits faibles, la nappe est influencée par la gravité et elle adopte une forme de cloche fermée / semi-ouverte. Lorsque Q augmente, cette dernière s'ouvre progressivement à cause de l'inertie. En outre, le jet turbulent à l'impact crée des perturbations locales dans le film qui déclenchent en aval du bord du disque des perforations aléatoires. Ces perforations apparaissent à une distance R' à partir de l'axe du jet. Elles s'amplifient et provoquent la désintégration de la nappe en gouttes. Ces gouttes sont caractérisées en terme de diamètres. La distribution de la taille des gouttes est étendue (les RSF sont proches de 1), qui est similaire à celle dans le cas des buses hydrauliques.

Dans un premier temps (chapitre 3), c'est le film semi-libre qui évolue radialement sur la surface du disque que l'on perturbe. Le film est perturbé par N gravures disposées radialement sur la circonférence du disque. L'insertion des gravures permet de contrôler l'écoulement turbulent et le film se divise en un nombre n de jets avant de quitter le bord du disque. Les diagrammes de phase sont présentés en fonction de l'écart $d1$ entre deux gravures successives et en fonction de débit Q. Différents régimes sont observés et sont

caractérisés par le nombre n des jets : $n = 2N$, $n = N_1^*$, $n = N$ et $n = N_2^*$. Le nombre de jets n peut être stable comme dans le cas de $n = 2N$ et $n = N$ ou instables comme dans le cas de $n = N_1^*$ et $n = N_2^*$. Le régime $n = N$ se produit lorsque la valeur de $d1$ est proche de celle de la longueur capillaire. Par contre, dans le cas de $n = 2N$, les jets sont émis dans deux plans différents permettant d'éviter la coalescence des jets. Les régimes $n = N_1^*$ et $n = N_2^*$ sont caractérisés par une fusion élastique des jets. La réduction de la longueur L de la gravure génère plus de jets. Cependant, cette réduction de longueur entraine plus de coalescences élastiques entre les jets principaux et secondaires. En outre, les gouttes sont caractérisées selon leurs diamètres et leurs vitesses. Les configurations comprenant des disques texturés présentent une distribution de taille des gouttes réduite comparée à celle du disque de référence (non gravé) et de la buse Teejet TP 65 15. Le V_{50} est réduit et la distribution est translatée vers des gouttes de tailles plus petites. Cependant, le V_{50} reste supérieur à celui de la buse Teejet. Avec les configurations actuelles de la gravure (L = 5 mm), seuls 72 jets sont générés sur 360°. Ce qui ne répond pas aux exigences agricoles en termes de nombre de jets (l'idéal est d'avoir 111 jets qui correspondent à un débit Q = 1,66 10^{-5} $m^3.s^{-1}$). En pratique, on peut augmenter le nombre de jets soit en réduisant la largeur de la gravure L, soit en augmentant la distance radiale sur la plaque à partir de l'axe du jet. Cependant, dans ce dernier cas, on est confronté à une décélération rapide de l'écoulement dû au frottement du liquide avec la surface.

Dans le chapitre 4, on a perturbé directement la nappe de Savart, c'est-à-dire la nappe libre qui évolue dans l'air. Un nombre N de prismes triangulaires sont placés dans la nappe à une distance radiale R_p de l'axe de l'injecteur. Cette distance est strictement supérieure à $\frac{D}{2}$ (D = diamètre du disque) et inférieure ou égale à R' (pour laquelle les trous apparaissent dans la nappe). Une fois le nombre de prismes et la distance R_p de l'injecteur sont fixés, la géométrie est déterminée par la taille du prisme et la distance b entre deux prismes successifs. En augmentant le débit Q, le nombre de jets est n = 0 (pour des Q faibles, la nappe n'impacte pas les textures), puis nous observons $n = N$ et $n = N^*$ (coalescence élastique des jets) pour des Q élevés. Un modèle géométrique a été développé afin d'expliquer la génération de jets individuels entre deux textures de prismes voisines. Ensuite, les gouttes générées ont été caractérisées en termes de diamètres et de vitesses. La distribution de la taille des gouttes est plus étroite que celle du disque de référence (non-texturé) et de la buse hydraulique TP 65 15. Le V_{50} diminue dans le cas où l'écart b entre deux textures voisines diminue pour la même distance radiale R_p de l'axe du jet. Aussi, le V_{50} diminue en augmentant la distance radiale R_p car l'épaisseur de la nappe

diminue selon $\frac{a^2}{2r}$ (a = rayon du jet). Toutefois, nous sommes limités par l'apparition des trous en R' qui résultent en la désintégration de la nappe. Dans le cas où les textures sont placés proche de la limite R', une distribution des taille des gouttes étroite centrée sur un V_{50} proche de 500 μm et des vitesses de gouttelettes de 4 m.s^{-1} sont obtenues. De plus, on note que 140 jets sont générés sur 360°, ce qui dépasse le nombre de jets obtenus dans le cas des disques munis de gravures. Face à ce constat, la méthodologie actuelle est une alternative prometteuse qui permet de réduire la décélération du liquide et d'augmenter le nombre de jets.

Dans le chapitre 5, on a discuté les différentes configurations des disques utilisées pour contrôler la nappe turbulente et la fragmenter en des jets individuels. Aussi, on a analysé leurs performances vis-à-vis des objectifs agronomiques en termes de diamètres et de vitesses des gouttes et de nombres de jets.

Enfin, le chapitre 6 conclut sur les résultats fondamentaux et l'accent a été mis sur la valeur ajoutée de la buse développée que pourra apporter dans l'application des PPP. En outre, on a proposé de nouvelles perspectives à la présente thèse. Par exemple, tester des textures de prismes triangulaires dans le cas d'une nappe liquide produite par une buse hydraulique standard.

Acknowledgements

First of all I would like to thanks the CARE TERRA for the funding of my PhD.

I would like to thanks Stéphane Dorbolo for his support and his supervision during these 4 years. You helped me to overcome my difficulties in fundamental physics. Your passion for research has given me the motivation to realize this PhD. Also, I would like to thanks Frédéric Lebeau for his continuous support during these 6 years. Your supervision, your comments and your advices helped to improve my background in the agricultural field.

I would like to offer my special thanks to Bruno Schiffers for his supervision during my first internship in 2012. Sharing this experience together help me to improve my skills in pesticide application.

My special thanks are extended to the members of my thesis jury for the comments during these four years: Hervé Caps, Sam Dehaeck, Alexis Duchesne and Bruno Schiffers.

I am particularly grateful for the support and good times given by my friend Nicolas De cock.

Advices given by Alexis Duchesne has been a great help to improve the quality of my work. Thank you very much for all skype discussions and the time you have devoted to me.

My special thanks goes to my colleagues in Gembloux and in GRASP: Mathieu Massinon, Sébastien Mawet, Galien, Martin, Hosni, Amine, Hbib...

To my family, Salem, Hafsia, Dhia, Sirine and Chayma. Thank you all for your support. I Love you all.

Contents

List of Figures

List of Tables

1

Introduction

Chapter 1

Introduction

1.1 Agricultural spray application and challenges

In the crop protection field, conventional farmers still use Plant Protection Products (PPP) to control crop enemies as for instance weeds, diseases and pests. In practice, the PPP application relies mainly on droplet clouds to carry the spray mixture containing the active ingredient and the adjuvant to the target surface [12]. The spray contains droplet with various diameters and velocities that depend essentially on the nozzle choice and its setting and the intrinsic physicochemical properties of the spray mixture. The spray quality is classified using standard reference nozzles and pressures to define limits between very fine / fine / medium / coarse / very coarse / extra coarse / ultra coarse classes [13]. The spray is also described by statistical volumetric parameters that are V_{10}, V_{50} and V_{90}. These parameters indicate respectively that 10 %, 50 % and 90 % of the spray volume is composed of droplets whose diameters are smaller than this value. The uniformity of the spray is described by the mean of the Relative Span Factor (RSF) defined as $\frac{V_{90}-V_{10}}{V_{50}}$. The higher the RSF value, the wider the drop size distribution and therefore the lower droplet spectrum uniformity [12].

The PPP application efficiency as a function of droplet sizes and velocities has been the subject of an extensive investigation during the last decade. Although some confounding publications due to the retention process complexity, some trends are well established. As

a rule of thumb, finer droplets ($< 150\ \mu$m) are known to ensure a better coverage on the surface target. However, they are prone to interactions with the wind which may cause their drift away from the target [14, 15]. On the other hand, bigger droplet follow a more predictable trajectory but may result in inadequate coverage. Droplets whose diameters exceed 270 μm may bounce or shatter at impact, what results in losses if adhesion at first interception is needed [16, 17]. Among others, the parameters determining the splash characteristics are the droplet kinetic energy and the surface properties. In addition, drift and the volume of droplet adhesion decrease with increasing V_{50}. A recent study showed that a spray with a V_{50} of 225 μm and a RSF of 0.6 released at 0.5 m at 10 m.s^{-1} above the crop produces low drift with moderate kinetic energy at the crop canopy level [18].

The widely used application techniques rely extensively on hydraulic nozzles. The operating mode of these nozzles is simple as it consists in forcing the passage of a pressurized spray mixture through a calibrated pore. As a result, a turbulent liquid sheet is produced and it disintegrates randomly into ligaments leading to droplets [19] (Figure 1.1a). These droplets are characterized by various diameters and velocities and different trajectories. The resulted droplet size distribution is wide and the RSF is fluctuating around 1 [12, 18, 20, 21]. In the case where the droplet size distribution is centered on a V_{50} that is optimal for spray retention, it may present a risk source of potential drifting or efficiency losses due to splashing phenomena. Moreover, the current trend in agricultural PPP application is to reduce the applied volumes for economic reasons. These reductions in applied volumes are made possible by decreasing the size of the hydraulic nozzle and the pressure and by increasing the forward speed during the PPP treatment. These modifications drastically affect the spray characteristics in particular the density, the size and the speed of the generated droplets [14] and therefore what may affect the efficiency of the treatment.

Much concerns are devoted to the environmental losses caused by the droplets airborne outside the spray pattern leading to their drift away from the target area. Decades of extensive investigations on the spray application field have led to the adoption of drift reduction technologies (DRT) such as shielded sprayers [22, 23] and air assisted sprayers [24]. Other DRT technologies also act on the droplet size distribution by altering the nozzle type and the operating pressure. Shifting the droplet size distribution towards coarse droplets (by increasing the V_{50}) reduce the risk of drift as the proportion of driftable droplets are reduced

as for instance in the case of anti-drift and air induction nozzles. However, such a practice decreases the treatment efficacy as the proportion of big droplets increases and may increase the splash percentage [17, 18]. As a result, in the case for which the secondary droplets will not be intercepted by the neighboring target canopies or airborne again. They eventually fall to the ground presenting a potential source of contamination. In addition, there is a limit in the droplet size distribution produced by the anti-drift nozzle, i.e. the shift of the spectrum towards big droplets in order to produce zero driftable droplets lead to ultra coarse sprays that may result in enough droplet impact. Consequently, an optimal droplet size range as narrow as possible (reduced *RSF*) is necessary, even for anti-drift nozzles, to minimize retention variability and to reduce drift hazard.

This statement motivated the researchers as early as in the 60's to develop an alternative spray technique namely the Controlled Droplet Application (CDA) using rotary atomizers. Its operation mode consists in an impact of a round jet on the center of a rotating disk. The liquid flows to the disk edge thanks to the centrifugal forces leading to the generation of either single droplets, ligament or sheet mode as the flow rate increases [25]. In the second scenario, the multiple jet ligaments breakup into droplets in the Rayleigh-Plateau regime depending on the jet velocity at the disk border (Figure 1.1b) [12]. The droplet size distribution is reduced and it is highlighted by a reduced *RSF* of 0.6 compared to that of the hydraulic nozzles [12, 20, 21] (Figure 1.2). The contrast in term of droplet size distribution between the hydraulic nozzles and the rotary atomizers derives from the different breakup modes occurring with the two atomizers types (Figure 1.1). Some mechanical designs have also resulted in a narrow range of droplet sizes for high flow output using grooves on the surface of a serrated cup as for instance the Micromax 120 where the *RSF* can be as low as 0.5 [21].

The CDA generator has the advantage of both reducing the extent of the droplet size distribution and decreasing the applied volume per hectare [12, 26]. In addition, the droplet diameters and velocities can be adjusted to the treatment under consideration through a range of rotational speeds and flow rates [12, 27–31]. The droplet diameter can be computed as follows [27]: $D_d = 3.8\ (\frac{\sigma}{\rho D \omega})^{0.5}$ (with D: disk diameter, σ: surface tension, ρ: the liquid density and ω: angular speed). Although the CDA devices have proven their performance in terms of efficacy and drift reduction in particular situations [31], they experienced a commercial failure. The bulkiness, the high cost and the bad setting use of

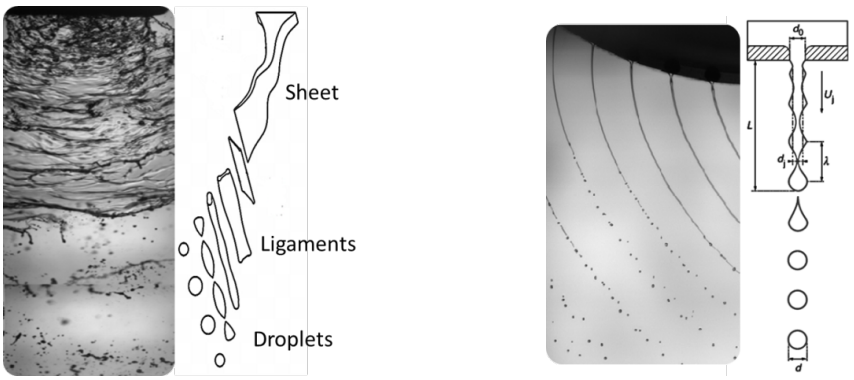

(a) (b)

Figure 1.1: Illustration of two breakup modes: (a) sheet breakup in the case of the hydraulic nozzle and (b) a jet ligament according to the Rayleigh-Plateau regime in the case of the rotary atomizer.

these devices in terms of V_{50} (i.e. centering the distribution on a V_{50} which is not favorable to adhesion relative to the surface target) and the direction of the spray (i.e. the horizontal release of droplets attenuates the downward velocity component that is a key component for drift reduction [15, 20]) have dramatically reduced their use. However, they remain an interesting case study as a way to produce sprays with a narrow drop size distribution.

As the pressure of environmental issues is increasing on the use of PPP, the European legal framework (2009/128/CE) becomes increasingly constraining about old and new PPP, spray application techniques and environmental safety. For instance, in the case of approval files of PPP, some new spray mixtures are no longer able to overcome the anti-drift trials even when a performant anti-drift nozzle is used (75% or 95% of drift reduction). Therefore, a more efficient nozzle which generates less driftable and controllable droplets is required. Furthermore, to meet the environmental requirements, much efforts were devoted to find other alternatives to reduce the *RSF* in addition to the application technique. It has been shown that the use of spray adjuvants such as emulsified oils can reduce the *RSF* and hence reduce the spray drift [32–34]. A best combination in the selection of spray nozzles and adjuvant are essential to avoid environmental contamination in term of drift and economic losses [34, 35].

To sum up, the PPP application has historically oscillated around environmental, efficiency and volume reduction constraints. The hydraulic nozzles were firstly developed and

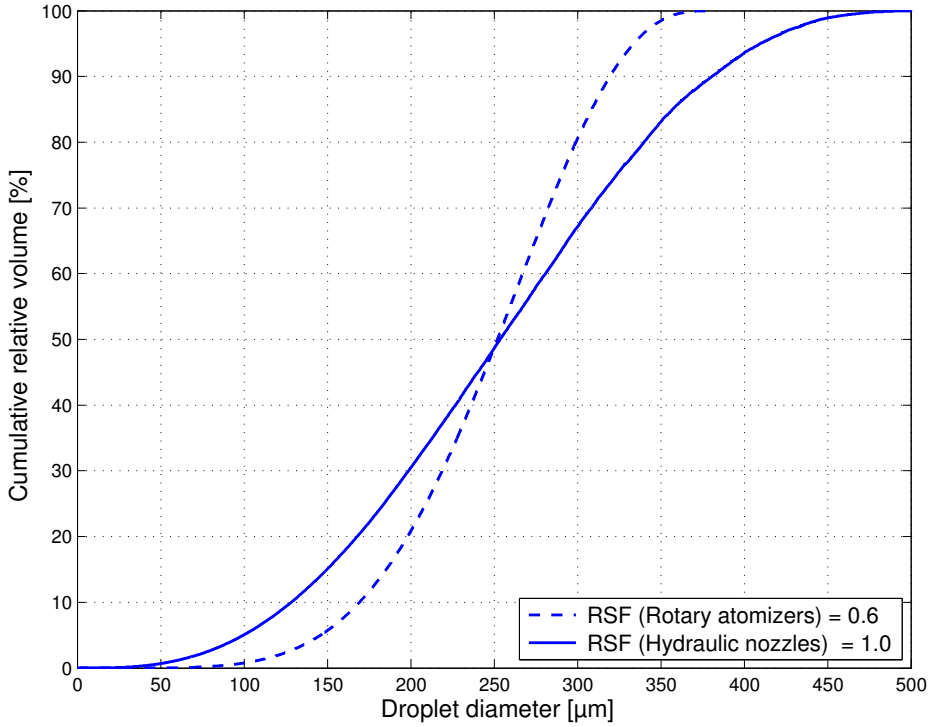

Figure 1.2: Cumulative relative volumes of droplets as a function of their diameters in the case of a hydraulic nozzle and a rotary atomizer. Both droplet size distribution are centered on a V_{50} of 250 μm but they have different RSF values.

generated a non-uniform spray that results in efficacy and environmental losses. Efforts were afterwards made to enhance the quality of PPP treatments by creating the CDA technology. The CDA approach has proven its relevance in terms of spray quality and efficacy. However, due to a lack of understanding of the parameters involved in spray retention and spray drift at a microscopic scale and the complexity of their devices, the technology had a commercial failure. Then, the pressure eased and research efforts were stopped around this thematic in the 90s. Finally, the hydraulic nozzles reappear and become the widely used nozzles in the crop protection field. Consequently, the environmental problems are kept going. The requirements of the European regulation related to the rational and the secure use of PPP have become more stringent. Therefore, the current nozzle characteristics are not able to meet these requirements. Finally, the pre-existence of CDA technology and the use of adjuvants to reduce the RSF justify and consolidate the research way for alternative solutions to enhance better spray uniformity.

The design of new nozzle that is able to generate a narrow droplet size distribution is a challenging path for the precision agriculture. The interesting way is to design the same nozzle as the CDA technology but based only on hydraulic pressure and without the rotating parts to generate narrow sprays. *Apriori*, this design could limit the barriers of the CDA technology as for instance it removes out the electrification and reduces the high weight on the boom sprayer. It would also be performant in the same application fields as the CDA and it can open new application fields. The configuration of Savart namely a jet impacting vertically on a disk constitues a technical solution as it meet the agronomic requirements that are the simplicity, the robustness, the low cost and the high flow rates. The characteristics of this promising configuration are detailed in the following.

1.2 Configuration of Felix Savart

In the application aim, the simplicity, the robustness and the low cost are required. Therefore, a round jet impacting vertically a horizontal smooth motionless disk is the ideal candidate for the massive production of droplets. The pioneer study on the subject was early conducted by Felix Savart (Figure 1.3), who observed many phenomena depending, among other parameters, on the ratio (X) : the impacted disk diameter D divided by the jet diameter d ($X = \frac{D}{d}$) [8–10, 36–38]. The limit case $\boldsymbol{X = 0}$ reveals the fate of a cylindrical jet discharge into a quiescent gaseous atmosphere. For $\boldsymbol{X \sim 1}$, the impacted jet deviates in an axisymmetric fashion and expands radially resulting in a sheet. Finally, in the limit, $\boldsymbol{X >> 1}$, one obtains the hydraulic jump. The case $\boldsymbol{X \sim 1}$ is obviously the best candidate as a droplet generator.

1.2.1 Jet breakup

In the case $\boldsymbol{X = 0}$, a circular orifice generates a cylindrical jet with a diameter d and an initial velocity U_0 defined as the volume flow rate Q divided by the exit section of the nozzle:

$$U_0 = \frac{4Q}{\pi d^2} \tag{1.1}$$

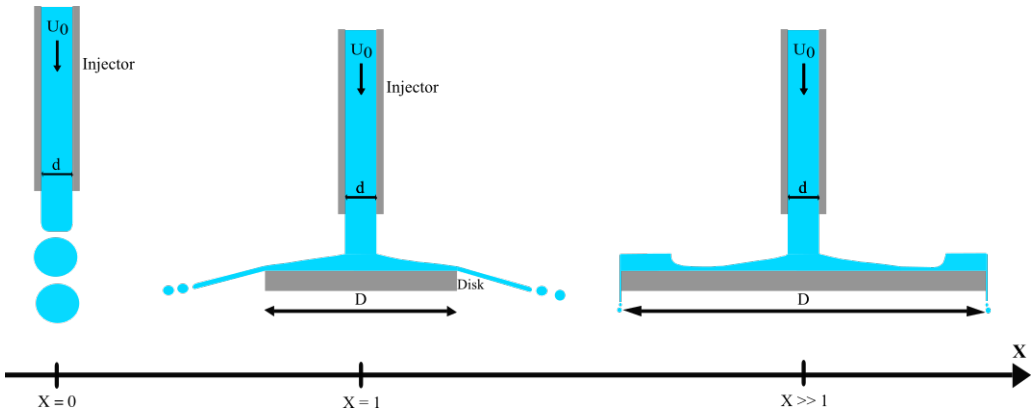

Figure 1.3: The Savart configuration consists in the impact of a round jet with a diameter d on a disk with a diameter D. Savart's observations depends on the ratio $X = \frac{D}{d}$: $\boldsymbol{X = 0}$ corresponds to the discharge of a cylindrical jet discharge into the atmosphere. For $\boldsymbol{X \sim 1}$, the impacted jet leads to a film that expands out radially and results in a sheet. In the limit, $\boldsymbol{X >> 1}$, the hydraulic jump is formed on the impactor.

The jet discharges then into a quiescent gaseous atmosphere. Possible deformations on the gas-liquid interface are likely to occur and lead to several fragmentation behaviors depending on U_0 and hence, to droplet formation. Using the stability jet curve that plots the breakup length of the jet (i.e the length of the continuous jet attached to the nozzle exit) as a function of U_0, five fragmentation regimes of the jet are identified: the dripping, the Rayleigh regime, the first wind-induced, the second wind-induced and the atomization (figure 1.4).

The dripping regime corresponds to a jet with a low inertia compared to the surface tension force. Consequently, the liquid jet accumulates at the orifice exit and it directly drips without the formation of a jet column. In the Rayleigh regime, the jet velocity increases and a laminar jet column is produced from the nozzle exit. The jet is disturbed by a single axisymmetric perturbation with a wavelength of the same order of magnitude the jet diameter. The breakup length is linearly dependent on the jet velocity. When the amplitude of the perturbation is equal to the jet radius, droplets with similar diameters are detached. The jet fragmentation occurs due to the capillary instability for which the most unstable perturbation breaks the jet in droplets of 1.89 times the jet diameter [39–41]. In the the first wind-induced regime, as the jet velocity increases, the perturbation is still axisymmetric and the shear between the jet interface and the surrounding gas (that

introduces aerodynamics forces) increases. This regime is reached when the surrounding force reached 10 % of the surface tension force. As a result, a decrease in the breakup length is observed. The droplet size distribution is wider than in the Rayleigh regime since satellite droplets between main drops are generated. In the second wind-induced, the liquid flow becomes turbulent by adopting a chaotic shape and aerodynamic forces and surface tension forces are of the same order of magnitude. Near the nozzle exit, small droplets are peeled off the interface. Further, the jet breaks up into random fragments that are subject to a secondary fragmentation and lead to droplets formation with various sizes. Finally, the atomization regime is defined as a complete jet fragmentation at the nozzle exit that lead to various size droplets. The produced droplets present average diameters much less than the jet diameter.

Boundaries between breakup regimes are usually described by a liquid Weber number We_L and a gaseous Weber number We_G, that are defined as follows [1, 41]:

$$We_L = \frac{\rho_L d U_0^2}{\sigma} \tag{1.2}$$

$$We_G = \frac{\rho_G d U_0^2}{\sigma} \tag{1.3}$$

with ρ_L and ρ_G (kg.m^{-3}) are respectively the liquid and the gas density, U_0 is the jet velocity (m.s^{-1}), d is the jet diameter (m) and σ is the liquid surface tension (N.m^{-1}). The critical We corresponding to the different boundaries are indicated on the figure 1.5. For instance, in the case of the Rayleigh regime that represents the ideal breakup to produce homogenous droplets, the We_L value has to be greater than 8 and the We_G has to be lower than 0.4.

The domain of existence of the five breakup regime can be distinguished in respect to the jet diameter and velocity as presented in the figure 1.5. The limits are computed using equations 1.2 and 1.3.

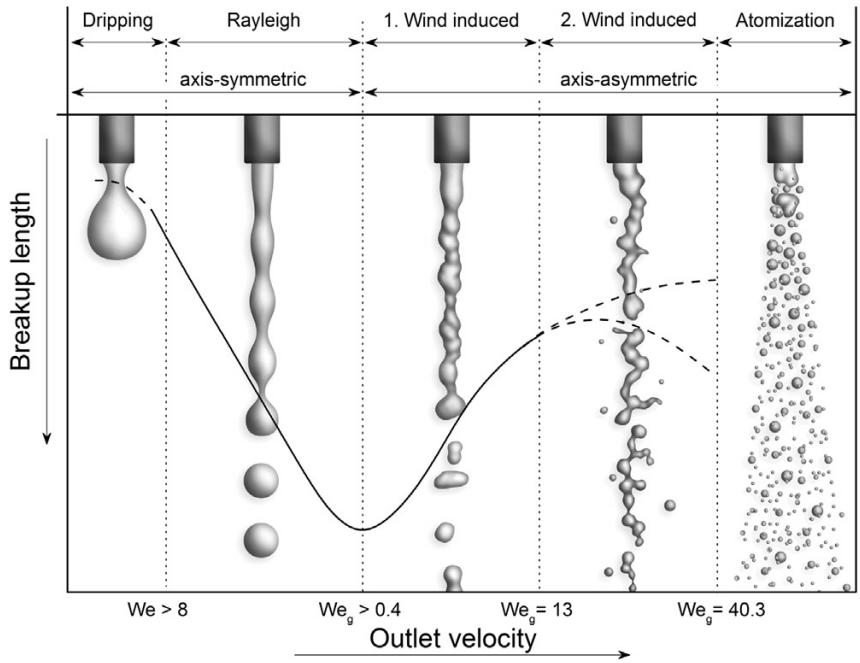

Figure 1.4: Illustration of the breakup regimes of a cylindrical water jet in still air at atmospheric pressure according to jet velocity U_0 [1].

1.2.2 What is happening on the disk

1.2.2.1 Case of $X \sim 1$

When $\boldsymbol{X \sim 1}$, the jet impacts the disk center with a velocity U_0 and is forced to spread out radially creating a liquid film. Much interest were devoted to the dynamics of the liquid film motion on the impactor [42, 43]. Watson provided in both laminar and turbulent motion regimes an analytical description of the liquid flow at the exit of the injector based on the boundary layer theory [42]. In the laminar regime, the boundary layer δ grows from the stagnation point on the jet axis until it diffuses the whole of the flow (i.e the volume flux through δ reaches Q) and that corresponds to a reference radial distance r_0. The speed outside the boundary layer which corresponds to the speed at the free surface U_∞, is unaffected by the viscosity and remains almost constant and its value is equal to U_0. The characteristic of the flow in this part are as follows:

$$r_0 = 0.31\ a\ Re^{\frac{1}{3}} \tag{1.4}$$

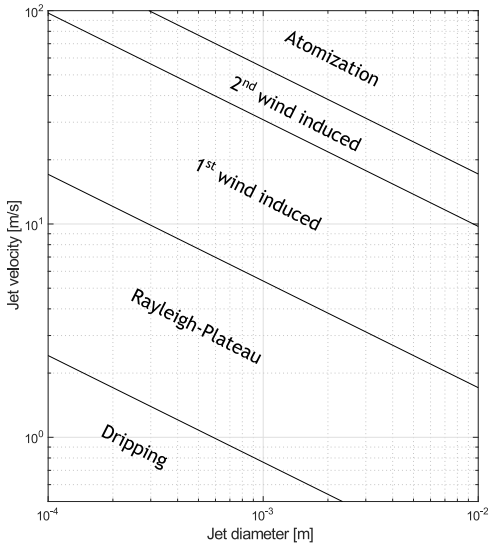

Figure 1.5: Field of existence of five breakup regimes of a water jet in the atmosphere. The limits are computed using the equations 1.2 and 1.3 [2].

$$h(r) = \frac{a^2}{2r} + (1 - \frac{2\pi}{3\sqrt{3}c^2})\delta \tag{1.5}$$

$$\delta(r) = \sqrt{\frac{\sqrt{3}c^3 \nu r}{(\pi - c\sqrt{3})U_0}} \tag{1.6}$$

where h is the total depth of the layer, ν is the cinematic viscosity and c is an analytical constant and is equal to 1.402 [42]. When the traveled radial distance r exceeds r_0, the whole flow passes through the boundary layer. The total depth of the layer h is equal to δ and U_∞ is inferior to U_0. The film thickness reaches its minimum at $r = 1.43r_0$, changes its direction and increases until obtaining an hydraulic jump. The expression of h in this part is as follows:

$$h(r) = \frac{2\pi^2 \nu (r^3 + l^3)}{3\sqrt{3}Qr} \tag{1.7}$$

In addition, a recent numerical investigation within a laminar flow, based on Watson theory, developed a new approach showing that the flow is accelerated close to the exit of the injector when the injector is put very close to the surface [43].

In the turbulent regime, the flow parts remain the same on the surface as described above. When $r < r_0$, the characteristic of the flow are as follows:

$$r_0 = 1.22\ a\ Re^{\frac{1}{9}} \tag{1.8}$$

$$h(r) = \frac{a^2}{2r} + \frac{k-A}{(80(A-\frac{2}{9}))^{\frac{4}{5}}}\frac{7\nu}{U_0}r^{\frac{4}{5}} \tag{1.9}$$

$$\delta(r) = (80(A-\frac{2}{9}))^{-\frac{4}{5}}k(\frac{7\nu}{U_0})^{\frac{1}{5}}r^{\frac{4}{5}} \tag{1.10}$$

with A and k are analytical constant and are respectively 0.239 and 0.260. When $r > r_0$, the expression of h follows the following law:

$$h(r) = \frac{9k}{200}(14\pi A)^{\frac{1}{4}}(\frac{\nu}{Q})^{\frac{1}{4}}\frac{r^{\frac{9}{4}}+l^{\frac{9}{4}}}{r} \tag{1.11}$$

with l is a constant length and is equal to $4.12\ a\ Re^{\frac{1}{9}}$.

1.2.2.2 Case of X $>>$ 1

Here the radial flow traveled a larger distance downstream and ended up being decelerated. Hence, the larger traveled distance, the larger deceleration and it results in an hydraulic jump. The hydraulic jump depends on the dimensionless Froude number $Fr = \frac{U}{\sqrt{gh}}$ (with U the mean flow velocity, g the gravity acceleration and h the mean liquid flow thickness). The hydraulic jump is characterized by an almost vertical liquid wall that shows the transition from a supercritical flow ($Fr > 1$) to a subcritical flow ($Fr < 1$) [42, 44, 45].

1.2.3 What is happening outside the disk

At the disk edge, the inertia force tends to detach the film whereas wetting forces try to keep the film on the disk. Once inertia forces exceeded capillary forces, the liquid film detaches at the disk edge and continues its radial expansion until reaching a maximum R at which the flow breaks up. The liquid sheet forms a self-suspended liquid sheet, called

Savart sheet. A competition between inertial and gravitational effects are involved in this phenomenon and are governed by the dimensionless Froude number $Fr = \frac{U}{\sqrt{gh}}$ (with U the mean flow velocity, g the gravity acceleration and h the mean liquid thickness). If Fr is higher than 1, the effect of the gravity on the liquid particle trajectory can be neglected and the liquid sheet remains relatively flat. Upon decrease of U_0, the curved Savart sheet progressively curved and closed onto the disk forming a closed liquid bell[46].

The behavior of the radial liquid sheet is described using the Weber number We_L criteria that is based on U_0 and d [3, 9]. This behavior is usually categorized by representing the non dimensional diameter $\frac{2R}{d}$ as a function of We_L (Figure 1.6). For low We_L (< 500), the liquid sheet is smooth and the action of the surrounding air on the dynamics of the sheet can be neglected. The radial position of breakup varies as $\frac{2R}{d} = 0.167\ We_L$ [3]. This law is fully compatible with Taylor's observations for which $\frac{2R}{d} = \frac{We}{8}$ [47]. At the sheet periphery, liquid beads attache a liquid film that breaks up under the capillary action. The beads are also subject to both gravitational and centrifugal acceleration. When acceleration effect overcomes the attachment capillary force, droplets detach. In the region of intermediate We_L ($500 < We_L < 2000$), cardioid wave pattern of Taylor [48] are firstly observed for $We_L < 800$ while the sheet adopts a flag flapping regime by increasing We_L. Cardioid wave pattern are induced by small amplitude disturbances at the jet impact. As a result, the sheet periphery becomes cusp-shaped that has no significant effects on the mechanism of the droplet production. In this transition region, Taylor's law is still respected and R reaches its maximum value for a critical We_L equal to 1200. For $We_L > 2000$, large amplitude Kelvin-Helmholtz instabilities predominate and grow on the liquid sheet leading to its disintegration. Here, the edge of the sheet is moving up and down like a flag flapping in the wind. The sheet radial breakup position R decreases with the increase of We_L and vary as $\frac{2R}{d} = 1250\ We_L^{-\frac{1}{3}}$. Moreover, the critical We_L to observe the Kelvin-Helmholtz instability depends on the surrounding density. For instance, in the case of water sheet in the air, the critical We_L varies from 1000 to 500 corresponding to an increase of ρ_G from 1.2 kg.m^{-3} to 6 kg.m^{-3} [9].

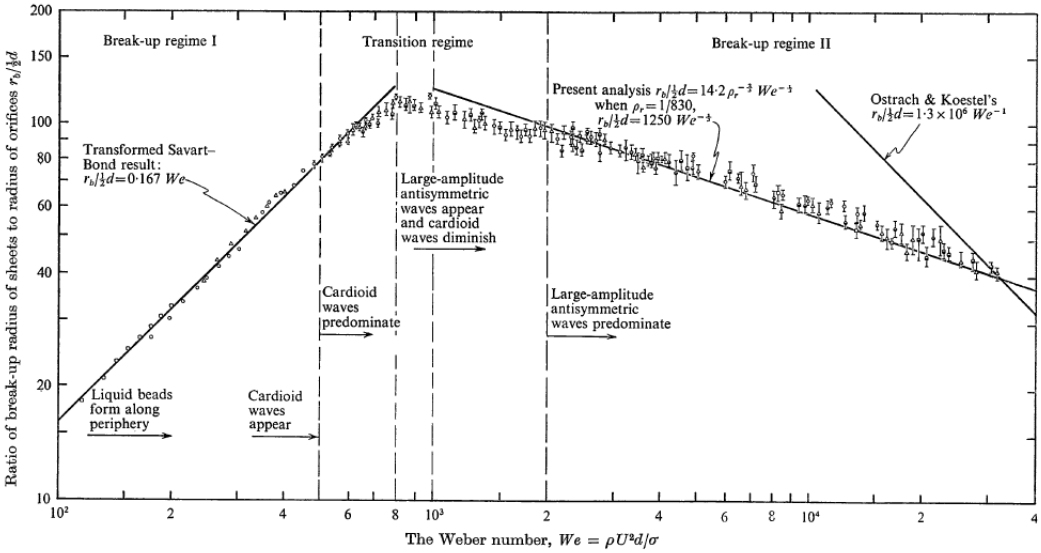

Figure 1.6: Illustration of Radial breakup position of a radial liquid sheet as a function of We_L [3]

1.2.4 Perturbation of the Savart sheet dynamics

The stability of the Savart sheet is questioned. The perturbations can be performed either on the disk surface by acting directly on the semi-free film or downstream the disk border by acting on the free sheet evolving in the air.

In the first scenario i.e. perturbing the semi-free film, several innovative studies were performed in order to control the shape and the stability of the Savart water bell using microtextured disks [4]. For instance, the presence of microposts regularly arranged on the disk surface created a local disruption. This latter will be advected downstream and resulted in a decrease of the water bell radius and the loss of axisymmetry as open water bells adopt polygonal shapes [4] (Figure 1.7). The macroscopic geometrical features in the bell rim reflect the geometry of the posts such as squares (Figure 1.7b) or hexagonals (Figure 1.7c). Compared to the standard Savart sheet where the droplets are emitted from the nodes (Figure 1.7c), the border of the sheet forms a rim. The rim presents the localized emission of bead ligaments that disintegrated into droplets. The droplet diameters are very big since the velocities of the jet ligament are very small. This sheet configuration presents

a promising technical way to applications related to atomization processes. When the microposts were inserted on a disk with $\boldsymbol{X >> 1}$, the local perturbations results downstream in a reduction of the radius of the hydraulic jump. However, this latter presents polygonal shapes as shown in the Figure 1.10 [5]. Other studies investigate the response of the film perturbed by a series of random sized grooves (knife cuts). They were engraved radially and regularly on the disk surface along its circumference but they did not destabilize the liquid film and resulted in a Savart sheet with cardioids forms at the surface [11].

In the second scenario i.e. perturbing the free Savart sheet, data relative to this kind of perturbation within the Savart configuration are scarce. A recent study showed that it is possible to modify locally the homogeneity of the free sheet. The experience consisted in approaching a drop of volatile liquid at a small distance from the film. As a result, a local decrease of the sheet surface tension leading to reduce the sheet radius (Figure 1.9). Moreover, much focus was devoted to the stability of liquid curtains (similar to the Savart sheet on the air). An obstacle put across the liquid sheet creates a steady hole in the sheet downstream that corresponds to a steady recession of a free edge of the sheet against the flow. The steadiness of the hole is obtained when both velocities of the flow and the receding are equal and it requires that the local Weber number is equal to 1 i.e $We_l = \frac{\rho h U^2}{2\sigma} = 1$ [11]. In addition, the case of the disturbance of a liquid curtain is quite interesting since asymmetric and symmetric blowing perturbations are applied against it. The pulsed asymmetric blowing of increasing amplitude results successively on sinuous wave, drop ejection, bubble ejection and hole opening. However, the case of a steady symmetric blowing leads to a steady hole downstream the wake [7].

To conclude, the both perturbations applied on the semi-free film and on the free sheet evolving in the air lead to a modification of the sheet dynamics downstream. The flow regime in these examples was laminar i.e the occurrence of puncturing within the flow is very low, what may facilitated the control of the sheet. However, data relative to the turbulent regime are scarce due to the complexity of sheet dynamics.

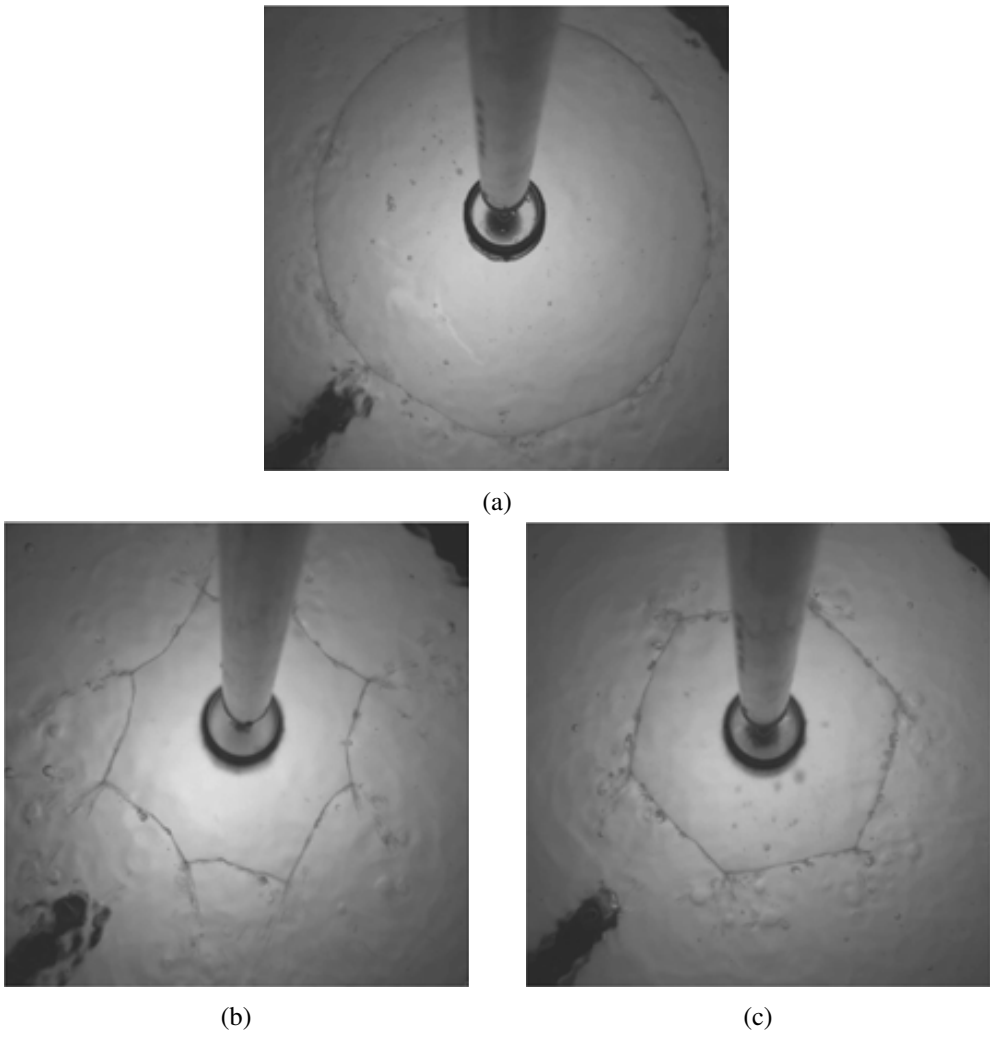

(a)

(b) (c)

Figure 1.7: The influence of microtextured disk on the shape and the stability of the savart sheet (a) case of a smooth disk: a standard Savart sheet is formed. By introducing of the microtextures on the disk, the sheet rim adopts polygonal shapes. The geometrical features in the rim reflect the geometry of the posts such as squares (b) or hexagonals (c) [4].

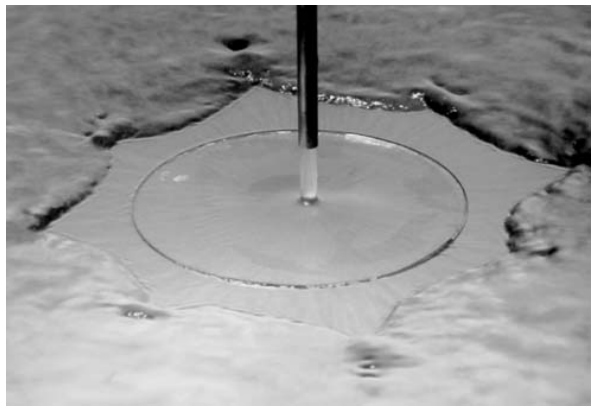

Figure 1.8: Polygonal shapes of the hydraulic jump [5]

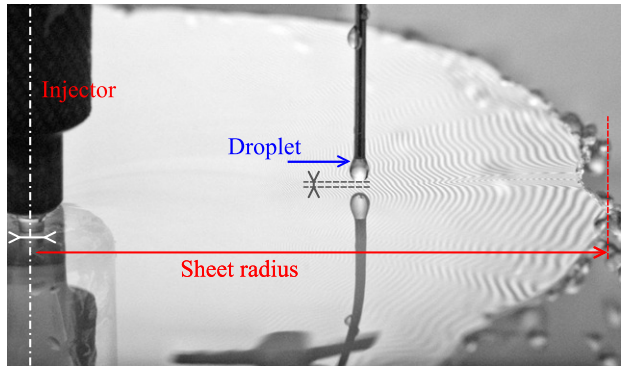

Figure 1.9: A disturbance for the film surface tension is performed by approaching a drop of volatile liquid at a small distance from the film. As a result, a decrease of the sheet radius is observed [6].

1.3 Thesis objective and methodology

The Savart configuration is the suitable design that meets the practical requirements of the PPP application. The Savart sheet expands radially in the air (outside the disk) and its breakup results in random ligaments and droplets leading to a wide droplet size distribution as in the case of hydraulic nozzles. As the used flow ranges are recommended to be high in the PPP spray application (the typical flow rate is 1.6 10^{-5} $m^3.s^{-1}$), the round jet is turbulent at the impact and hence the Savart sheet and its rim were turbulent by construction. The challenge is to tame the turbulent sheet. I propose to split the sheet into individual jets using textured disks by acting on the semi-free film namely on the disk

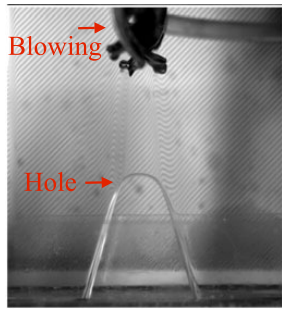

Figure 1.10: A steady hole downstream the blowing source within a liquid curtain [7].

or by inserting the right structures directly in the free sheet. Then, I will show that the jets break up according to the Plateau-Rayleigh mechanism and lead to a narrower droplet size distribution. Therefore, this thesis aims to study experimentally the effect of the disk geometry on the sheet break up. This study is seen as a practical guide for specialists in fluid mechanics who desire developing the generation of drops with controlled sizes.

The established methodology in this study is as follows. One firstly investigate the turbulent Savart sheet that results from the impact of a turbulent round jet on a non-textured disk. This constitute our reference case. Then, one perturbs the semi-free film. The case of a disk engraved by a radial grooves along its circumference is addressed. Finally, one breakups the sheet evolving in the air using radial triangular prisms.

An overview including the motivation to establish this thesis, the objective and the methodology followed to tame the turbulent sheet is presented in the Figure 1.11.

1.4 Thesis organisation

The thesis manuscript is organized as follows.

In the chapter 2, one detailed the experimental setup based on the impact of a turbulent jet on a non-textured disk. The disk configuration constitutes our reference case to which results on textured disks are to be confronted. One firstly investigates the semi-free film on the non-textured disk by characterizing its intrinsic parameters (The mean velocity, the mean thickness and the ejection angle). Then, the focus is made on the free Savart

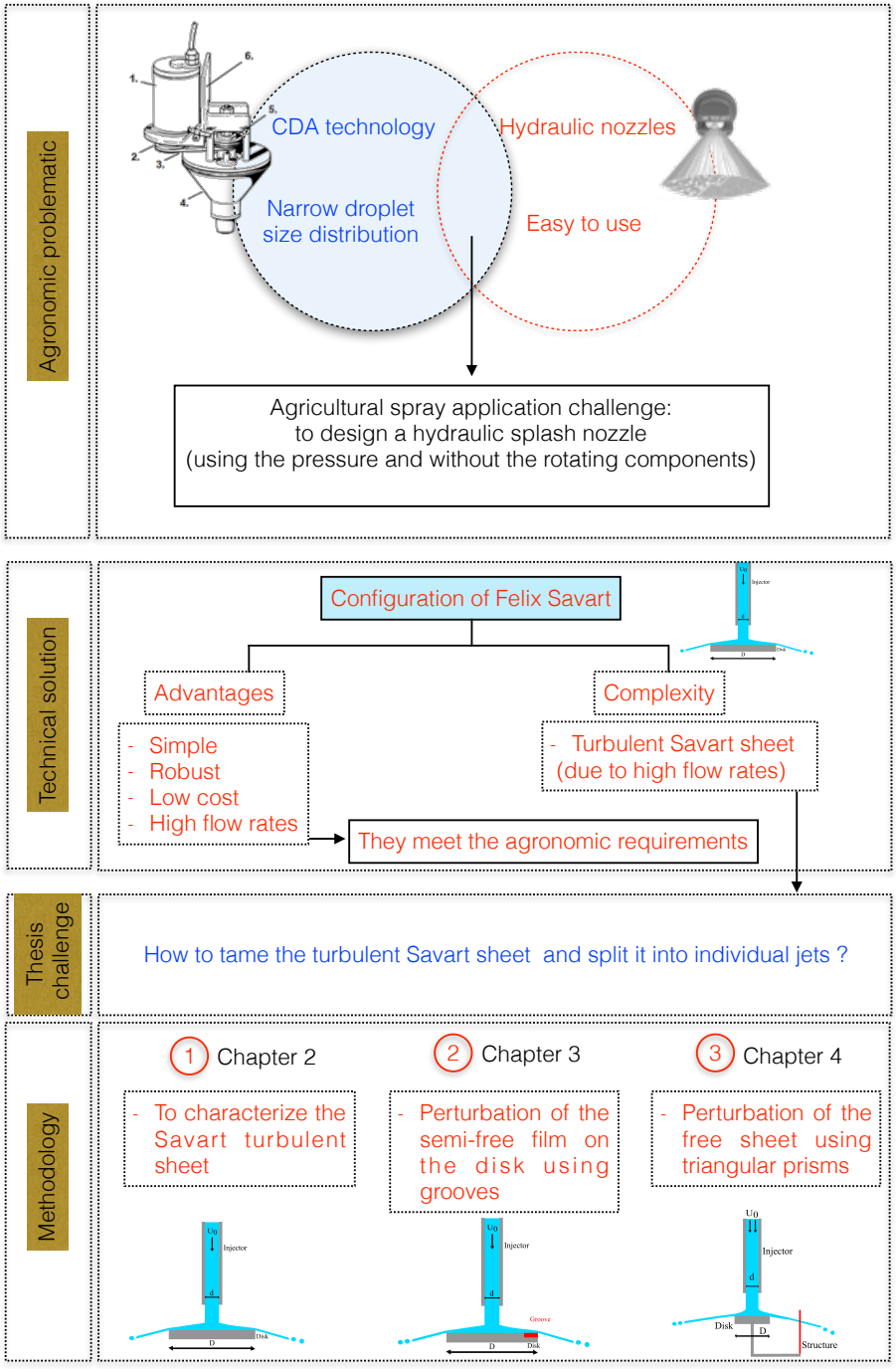

Figure 1.11: Overview of the thesis including the agronomic problem, the technical solution, the thesis objective and the methodology.

sheet evolving in the air. The sheet radius and the holes (due to the turbulent regime) are characterized. Finally, the droplet diameters are characterized in term of numbers and volumes.

In the chapter 3, one perturbed the semi-free film evolving on the disk surface. The case of a turbulent round water jet impacting a disk engraved along its circumference by a number N of radial grooves is addressed. The grooves are used to split the liquid sheet into multiple jets. The numbers of jets n are determined according to the incoming flow rate Q and to the geometry of the groove. Then, phase diagrams (Q,n) are established from measurements for different lengths of the groove. Finally, the droplets obtained from different jet regimes are characterized in term of diameters and velocities.

In the chapter 4, one perturbed directly the Savart sheet evolving in the air. A number N of triangular prisms are set in the sheet downstream the disk border. These structures are used to breakup the sheet into individual jets. One developed a geometrical model that explains the generation of individual jets through the gap between two neighboring structures. Different jet numbers n are defined according to the flow rate Q and to the geometry of the prism. Phase diagrams are then established as a function of Q and n. Then, the emitted droplets are characterized in term of diameters and velocities.

In the chapter 5, one established a benchmark between the disk configurations used to taylor the turbulent sheet and to split it individual jets. One also discussed their performances to meet the agronomic objective in term droplet diameters and velocities and jet numbers.

Finally, the chapter 6 concludes on the fundamental findings in spray applications and one proposed some original perspectives to the present thesis.

2

Turbulent Savart sheet

Chapter 2

Turbulent Savart sheet

This Chapter constitutes the basis case to which we refer along the thesis.

The Savart sheet that results from the impact of a round jet on a surface within a laminar regime was intensively investigated [8–10] (Figure 2.1). Depending on the Weber number *We*, the sheet edge presents different behaviors. For *We* inferior to 1000, it adopts a smooth regime by exhibiting cusp structures for which droplets are ejected [9]. For larger *We* values, the flapping regime is observed while the the edge behavior is moving up and down like a flag flapping in the wind [10]. This chaotic disintegration results in droplets (Figure 2.1c). To our knowledge, scarce data relative to the turbulent regime are reported in the literature.

In this chapter, the situation of a turbulent liquid jet impacting a non-textured disk is addressed. The disk configuration constitutes our reference case to which results on textured disks are to be confronted. This turbulent sheet regime is interesting with respect to our agronomic objective because:
- The used flow rate ranges are high and correspond to the ones used in PPP spray application.
- The design configuration is simple (splash nozzle) and robust.

The chapter is structured as follows: In the first part, one introduces the experimental setup that is generic for all experiences performed in the whole thesis. In the second part,

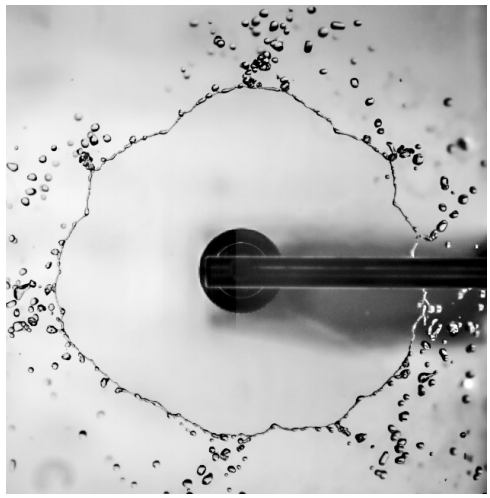

(a)

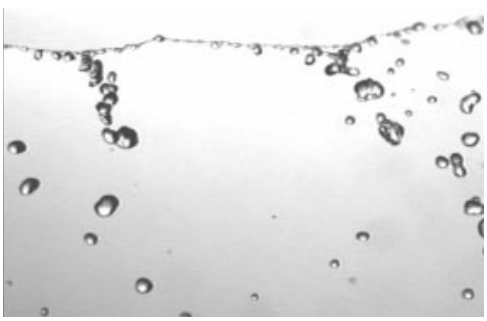

(b)

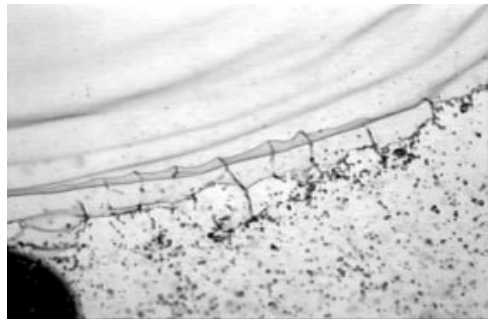

(c)

Figure 2.1: A free Savart liquid sheet resulting from the impact of a round jet on a disk is presented. (a) The Savart sheet is seen from the top view. It exhibits a typical cusp structure at the edge from which droplets are ejected (b)[8]. Zoomed view of the sheet edge (c): one can see vertical oscillations (flapping regime) [9, 10].

the turbulent Savart sheet is studied by focusing on its shape and its radial expansion. Then, experimental measurements of the mean flow velocity downstream the jet impact (1 mm before the disk edge) are performed in order to investigate the influence of the surface friction. Finally, the generated droplets are characterized in terms of diameters.

2.1 Experimental setup and used techniques

2.1.1 Setup

The experimental setup is presented in Figure 2.2. The nozzle consisted in a glass injector with an internal diameter of 3 mm set perpendicularly to a motionless disk fixed on a support in the middle of a 200 mm side cubic. The orifice of the injector generated a cylindrical liquid jet d = 3 mm which impacted the disk center with a mean velocity U_0. Much interest was devoted to the homogeneity of the injector exit that was carefully sanded to homogenize its surface regularity and flatness and hence, to standardize the flow thickness close to the injector exit. The gap H between the injector tip and the disk surface was set to 550 μm using a three axis precision displacement tool (XYZ). This H value represents the critical distance that can be achieved with regards to the gear pump.

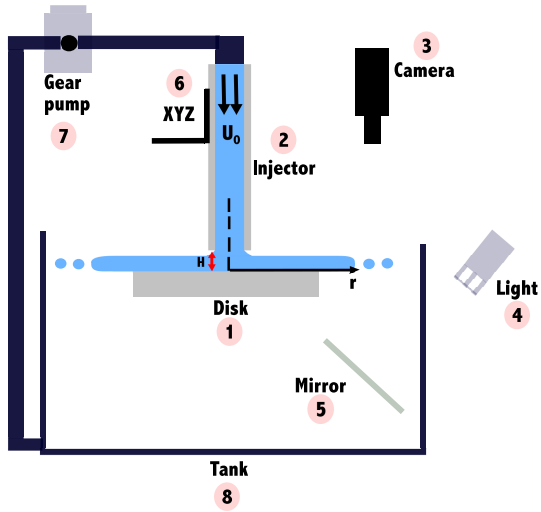

Figure 2.2: Experimental setup: An injector consisting of a glass pipe (2) generated a round jet d = 3 mm. The injected water impacted the center of a plexiglass disk (1) with a velocity U_0. The disk was placed in the middle of a 200 mm side cubic tank (8). The liquid flows radially and creates a Savart sheet. The gap H between the injector tip and the disk was fixed using a precision displacement tool XYZ (6). A high-speed camera (3) was mounted vertically to the disk border to acquire images of the liquid sheet and the emitted droplets. A mirror (5) was tilted by 45° to the camera optic axis in order to reflect the light towards the disk. The liquid was injected by the gear pump (7) connecting the tank to the injector (2).

The liquid flow was injected using a gear pump (Ismatec BVP-Z) combined with a pump head to reduce the flow pulsation and thus delivering steady liquid flows. The flow was measured by weighing the liquid poured into a graduated tank during 30 s. Three repetitions were performed for each flow measurement. By changing its rotation speeds, flow rates Q were varied from 1.5 10^{-5}m^3. s^{-1} to 4.1 10^{-5}m^3. s^{-1}. The Re numbers inside the glass injector range between 9000 and 16000 that correspond to a turbulent impact on the disk.

The used liquid was tap water at 20 °C. The surface tension was measured using an optical contact angle meter (CAM 200 KSV) based on the hanging droplet technique and one found σ = 73.5 $\pm$ 0.3 mN.m^{-1}. The liquid was also characterized by its density ρ = 1000 kg.m^{-3} and kinematic viscosity $\nu = 10^{-6}$ m^2.s^{-1}.

The core of our experimental setup is the disk surface. Two different disks in terms of matters and diameters were used. The first disk was a plexiglas plate cut with a laser cutter (Trotec Speedy 100 TM) (see also Chapter 3). The disk diameter D was fixed to 25, 30, 40 mm. The static wetting property of the tap water on the surface was characterized by a measured contact angle of 74° (static wetting) measured using an optical contact angle meter (CAM 200 KSV) (see also Chapter 4). On the other hand, the second disk was a 3D veroblue printed with a 3D printer (Objet30 Prime TM). The disk diameter D was fixed to 6 mm. The measured contact angle was 25° (static wetting).

The choice of the disk material is directly linked to the feasibility, the rigidity and the surface finish level of the structures used in the following chapters to perturb the Savart sheet. For instance, in the case of the engraved disk with radial grooves (Chapter 3), the homogeneity level of the grooves engraved by a numerically controlled CNC machine is better than that in the case of the 3D print. However, in the case of triangular textures put outside the disk circumference (Chapter 4), the textures were printed with a 3D printer because of a rigidity requirement.

Furthermore, the choice of the disk diameter depends on the strategy established in the sheet perturbation. In the case of the semi-free film perturbed using textures inserted on the disk circumference (Chapter 3), the disk diameter is of intermediary size (X = 10). It would be large enough to insert an adequate number of textures on the surface but not too large to keep an acceptable level of friction on the surface (a larger disk would increase

the solid friction and resulted in a hydraulic jump). In the other case, i.e. the free Savart sheet is perturbed using textures put outside the disk circumference (Chapter 4), the disk diameter is chosen to be the smallest possible with a ratio $X = 2$ in order to reduce friction on the surface and hence to permit the formation of an expanded Savart sheet.

In both disk configurations (plexiglass and veroblue disks), the disk horizontality was checked by a spirit level in order to ensure that the impacting jet is perpendicular to the disk. In so doing, the symmetry of the liquid sheet is optimal.

To resume, two disk characteristics were used as follows:
- A plexiglass disk with a $D = 30$ mm and a $X = 10$.
- A veroblue disk with a $D = 6$ mm and a $X = 2$.

2.1.2 Image acquisition

One used a high speed camera Y4 (IDT motion) to record images of droplets. A mirror was tilted by 45° to the optic axis and it reflected the light emitted from the source light which was set perpendicularly to the mirror. Images were acquired at a frequency of 2000 Hz and treated with a Particle Tracking Velocimetry Sizing (PTVS) algorithm developed in Matlab [49]. The droplets were measured as soon as they were detached from the sheet (60 mm from the disk edge) in order to avoid merged droplets.

2.1.3 Measurement of the film mean velocity on the disk

The mean velocity of the liquid film downstream the jet impact (1 mm before the plexiglass disk edge) is obtained through an experimental measurement of its thickness. One used a simple technique described by Azuma and Toshino [50]. The experimental setup is presented in the Figure 2.3. A thin needle driven by a three axis precision displacement tool (XYZ) was set 1 mm before the disk edge. The needle was lowered down and when it touched the liquid surface, a droplet was rapidly formed on the needle tip (Figure 2.4). Then, the liquid flow was stopped and the needle was lowered down to reaching the disk surface (Figure 3). The difference between both heights gives the liquid thickness. The measurement process was eye-guided using the images from the high-speed camera Y4

optic axis which was set perpendicularly to the needle axis, on the same plane as the disk surface (Figure 2). Using this film thickness measurement, the film mean velocity reads: $U(r) = \frac{Q}{2\pi rh}$ (with U: film mean velocity, Q: injected flow rate, r: flow radial distance and h: film thickness).

We only measured the film thickness in the case of the plexiglass disk because the considered disk diameters allow the application of the measurement technique using the needle.

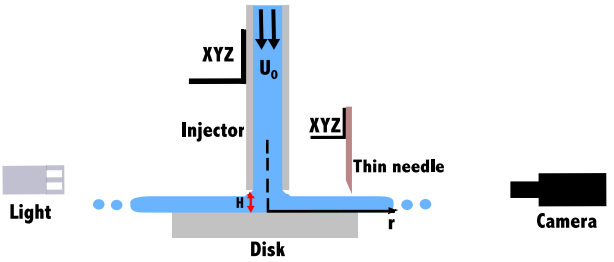

Figure 2.3: Experimental setup for film thickness measurement: A thin needle set downstream the jet impact (1 mm before the plexiglass disk border) was used to measure the thickness of the liquid film. Its displacement was tuned by a precision three axis displacement tool. A high-speed camera Y4, for which the optic axis was set perpendicularly to the thin needle axis and facing a light source, was used to control the measurement process.

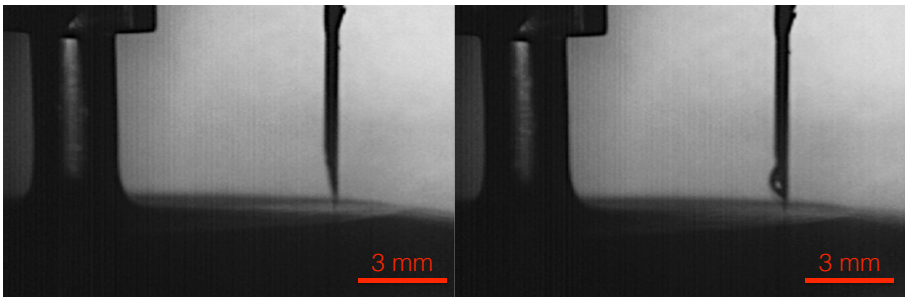

Figure 2.4: Illustration of the film thickness measurement process based on a thin needle displacement in the case of a plexiglass disk. The needle was set downstream the jet impact (1 mm before the disk edge). On the right, the needle touched the liquid surface and a small droplet appeared rapidly. The *Re* and *We* were respectively 10 640 and 529.

2.2 Turbulent Savart sheet

2.2.1 Evolution of the water bell

As expected, the jet impact on the non-textured disk center resulted in a thin liquid film that flowed radially, exceeded the disk border and lead to a curved and self-suspended Savart sheet (or bell at low flow rate). In this section, one firstly focus on the evolution of the curved shape of the Savart sheet and, then, on its radial expansion.

The Savart sheet was filmed from a side view to investigate the evolution of its conical aperture as a function of Q. The Figure 2.5 presents the evolution of the angle ϕ, which represents the opening angle of the curved sheet relative to the perpendicular plan to the disk border, as a function of Q. The acquired images from a side view of the nozzle are embedded in the Figure 2.5 in order to provide a better comprehension of the sheet evolution. No variability is observed when measuring ϕ. For low Q values, the sheet is subject to the gravity ($Fr < 1$) and is getting curved closer to the jet axis (a ϕ value of 54°). The obtained shape is a closed / semi-opened water bell as it is illustrated on the first image (on the left) in Figure 2.5. Upon an increase of Q, the water bell progressively opens and the gravity effect is neglected compared to inertia ($Fr > 1$). It presents a slightly curved shape highlighted by a ϕ value inferior to 90° for high Q values. Hence, one cannot reach a horizontal ejection of the sheet with a flat impactor as observed in the literature [46]. Some alternatives were found to force the sheet to exit the impact surface with a horizontal ejection angle such as the case of a thin copper coaxial cylinder embedded at the disk edge [9].

Also, it is crucial to indicate that the ejection angle is sensitive to $X = \frac{D}{d}$ in addition to Q [46] i.e. for $X >> 1$, the closed bell is less pronounced. In the following, the Savart sheet is filmed from a top view in order to characterize its radial expansion.

At the disk edge, the liquid film was ejected with an angle ϕ and constituted a Savart sheet of radius R. The sheet rim was delimited by nodes where the liquid was concentrated. These nodes were the emission point of droplets (Figure 2.6) as observed in the literature [8]. As the jet flow is turbulent at the impact (characterized by high Re numbers inside the injector) the Savart sheet and its rim were turbulent by construction. The impact wave

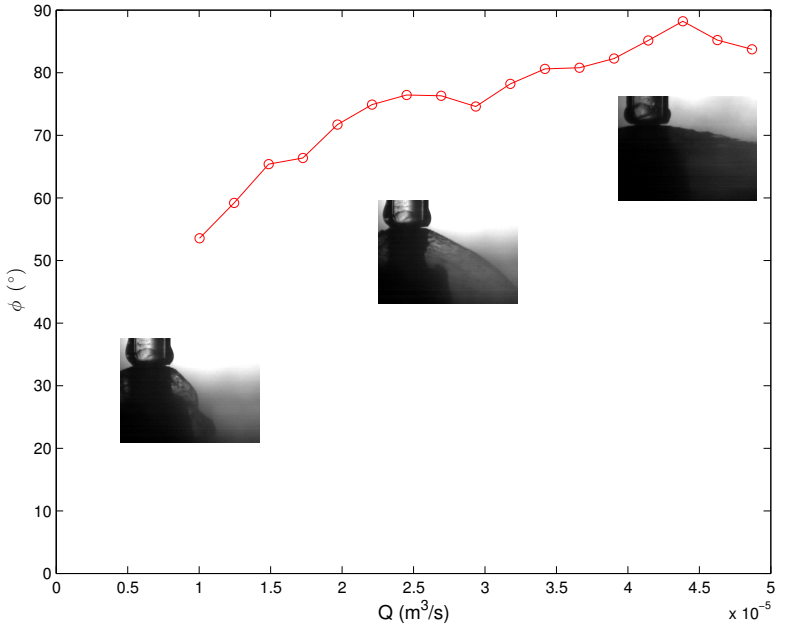

Figure 2.5: Case of the veroblue disk ($X = 2$): Evolution of the angle ϕ, representing the opening angle of the curved Savart sheet relative to the perpendicular plan to the disk border, as a function of Q. The images acquired in a side view of the nozzle reflect the evolution of the sheet from a curved bell to a conical sheet.

disturbances emanating from the turbulent impact may be observed on the sheet surface. As a result, the local disturbances in the film triggered downstream the disk border the formation of random holes at a distance R' (from the jet axis) in the liquid sheet. These holes amplify and lead to the disintegration of the liquid sheet into droplets. Studies on the turbulent regime are relatively scarce. However, these holes were observed within the turbulent splash plate atomization [51].

The Figure 2.7 shows the evolution of the radii R and R' of the Savart sheet as a function of Q. These radii values were computed from 100 images separated by 0.5 ms. This fairly short timescale was chosen in order to better tracking of the evolution of sheet holes. All the radii were measured within the same angular coordinates in the lab reference. Error bars indicate the standard deviation calculated using 100 measurement repetitions of R and R' based on 100 images for the same Q. The two curves have similar trends and they can be divided in two parts. The first part is characterized by an abrupt slope for

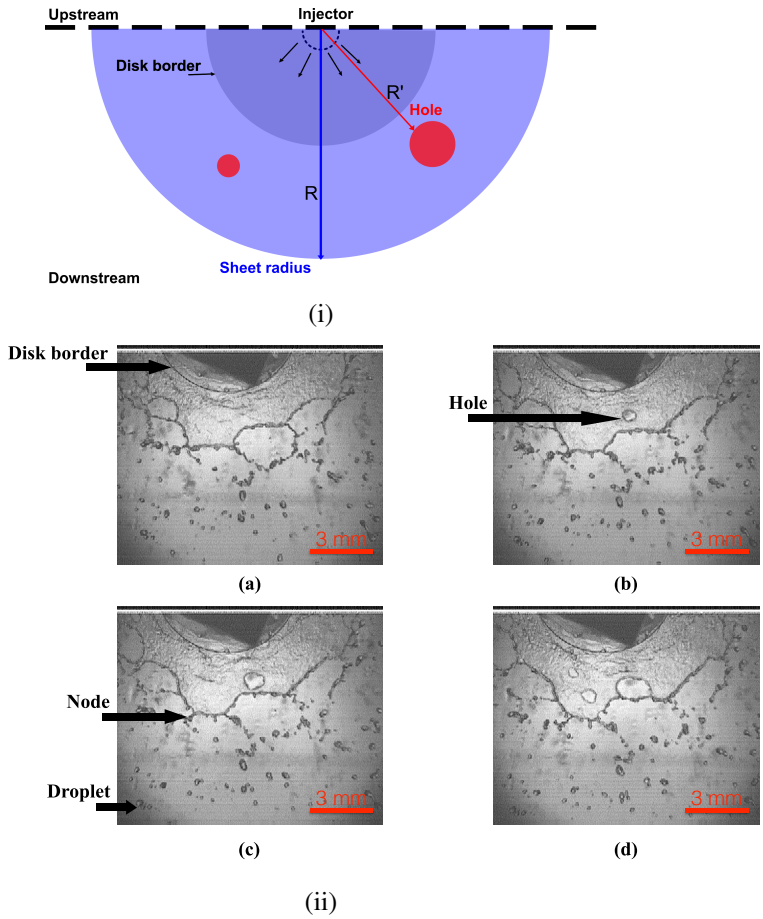

Figure 2.6: Top view of the evolution of the Savart liquid sheet within a turbulent flow. (i) a sketch presenting the radial sheet expansion and the appearance of holes downstream the disk border. (ii) The four successive images (a, b, c and d) were timely separated by 0.5 ms. The holes appear and then split the sheet into random ligaments leading to droplet formation in the case of a veroblue disk (X = 2). The jet was characterized by U_0 = 4.22 m.s^{-1}, Re = 12 414 and We = 719.

$Q < 2.5\ \ 10^{-5}$ m^3.s^{-1} where the second part of the curve is characterized by an almost constant radial radius.

For the sheet expansion, its radius R increases almost linearly with the increase Q despite the appearance of the holes in the sheet for $Q < 2.5\ 10^{-5}$ m^3.s^{-1}. Then, for high Q values, the sheet presents R values around 40 - 50 mm corroborated by high lengths of error bars. On the other hand, the holes appear downstream the disk border and they never exceed the sheet rim i.e. $R' \leq R$ even in ascending part of the curve. For a wide range of

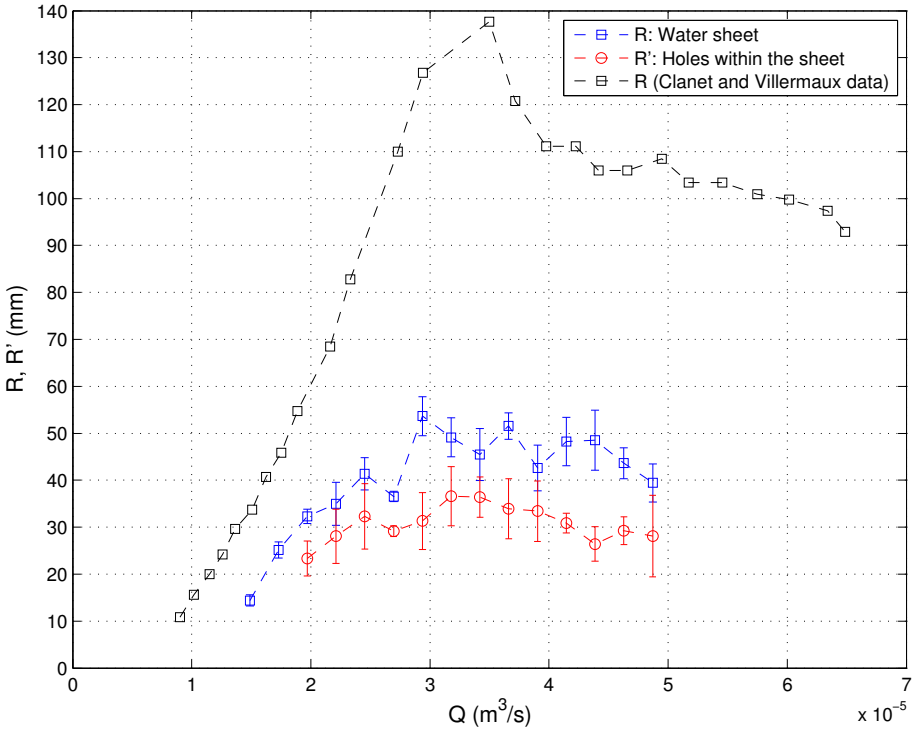

Figure 2.7: Evolution of the radii R and R' of the Savart sheet as a function of Q within a turbulent flow regime. The case of the veroblue disk ($X = 2$) is studied. Experimental measurements of Clanet and Villermaux [9] of the radius R within a laminar flow regime are added. Their D and d were respectively 10.8 mm and 2.7 mm corresponding to a $X = 4$.

Q ($> 2.5\ 10^{-5}$ m^3.s^{-1}), R' is almost constant (around 30 mm). Hence, it presents at this stage a new constraint, in addition to the sheet expansion R, at the location of structures within the sheet (Chapter 4).

Moreover, one added experimental measurements of Clanet and Villermaux [9] of the sheet radius R in the Figure 2.7. Their D and d were respectively 10.8 mm and 2.7 mm ($X = 4$) and their Q values corresponded to our Q ranges. Despite these similar conditions, they generated a laminar Savart sheet thanks to their injector exit that permits to a generate a laminar flow even at high Q. Unfortunately, they did not detail their injector exit [9]. By comparing the two curves of R in both regimes, they present similar trends and the turbulent regime presents smaller R values due to holes for the same Q ranges.

No benchmarks in terms of the radial sheet expansion R were found due to a lack of data within the turbulent regime and the evolution trend of the non dimensional critical diameter $\frac{2R}{d}$ addressed in the Chapter 1 is no longer valid.

2.2.2 Downstream film velocity

The Figure 2.8 presents the film mean velocity U, measured downstream the jet impact and 1 mm before the disk edge, as a function of $Re = f(Q)$ for three disk diameters. The experimental velocities were measured based on the flow rate Q and the local measured thickness h of the liquid film. Error bars show the error on the speed U due to the incertitude on h. The standard deviations of h was established using three independent measurements for the same Reynolds numbers Re. The mean velocity U increases when the Re is increased for each disk diameter. For the same Re, the flow is slown down when the disk diameter is increased. This can be explained by the increase of friction forces on the disk surface for a given Re that promotes the growth of the boundary layer on the impactor.

During the measurement process of h, at high Re, the liquid surface position was estimated despite the presence of the disturbance waves. Therefore, the thickness h may have been overestimated since the droplet appears on the needle for the maximum height and not the mean value. This overestimation leads to an underestimation of U. In the case of the disk diameter of 40 mm, the flow slowed down and disturbances waves were attenuated compared to the jet impact. The flow surface was more stable and the measurement process of h was easier to establish.

To sum up, the shape of the Savart sheet is sensitive on the flow rate Q. The sheet exhibits a curved bell, at low Q, that is subjected to the gravity. Upon an increase of Q, the inertia dominates and the sheet looks as a cone. The sheet is characterized by a maximal radial expansion R. Some holes, randomly appear in the sheet at a distance R' from the center and triggered its disintegration at this location $R' \leq R$. Therefore, the distance R' is a constraint within the case of the tap water sheet that is more strict than R, for the location of textures in the sheet. Furthermore, the mean velocity U decreases by increasing the radial distance

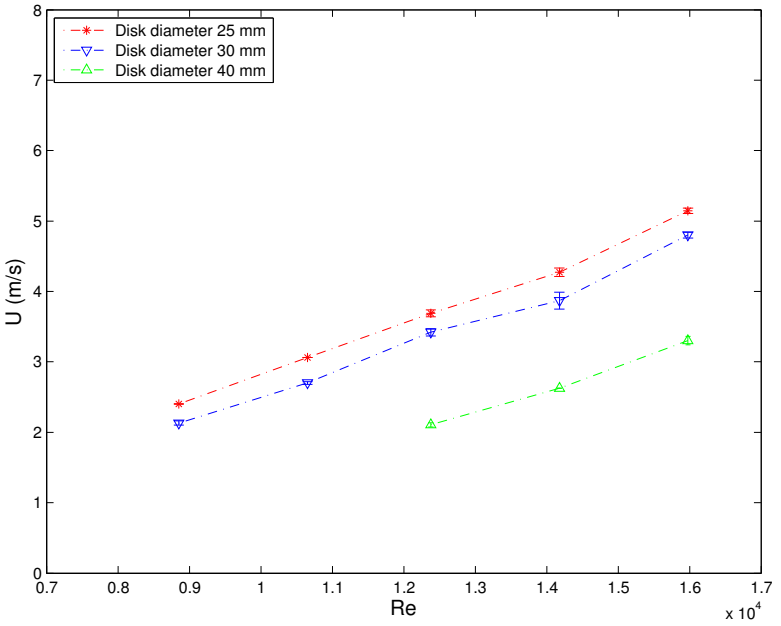

Figure 2.8: Mean velocity U of the liquid flow measured downstream the jet impact (1 mm before the disk border) as a function of Re (Re depends only on the injected Q) in the case of the plexiglass disk.

on the disk surface. Hence, one encountered two constraints on the disk surface that are the film deceleration and the hydraulic jump.

The liquid sheet randomly disintegrates and results into droplets. In the following, the generated droplets are characterized in terms of diameters.

2.3 Atomization of the turbulent Savart sheet

The emitted droplets from the Savart sheet have to be characterized in terms of their diameters. In the following, the droplets are firstly presented in terms of their numbers and then, presented in terms of their volumes.

To study the droplets characteristics in terms of their numbers, one needs to define relevant tools as the mean droplet diameter $D_m = \frac{1}{\mathrm{N_d}} \sum_{\mathrm{i=1}}^{\mathrm{N_d}} \mathrm{D_{d,i}}$ (N_d : the droplet number, D_d

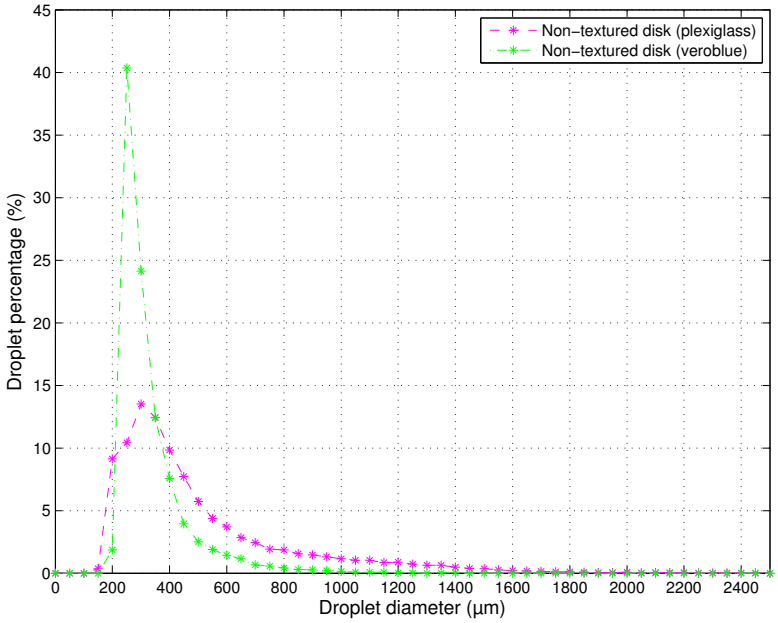

Figure 2.9: Representation of droplet percentages as a function of their diameters. The cases of the plexiglass (X = 10) and the veroblue (X = 2) non-textured disks are studied. The measurements were performed at a Q = 2.8 10^{-5} $m^3.s^{-1}$

: the droplet diameter), the Standard deviation $STD = \sqrt{\frac{\sum_{i=1}^{N_d}(D_{d,i}-D_m)^2}{N_d}}$ and the coefficient of variation $CV = \frac{STD}{D_m}$.

The Figure 2.9 presents the probability density function (PDF) of droplets where droplets percentages are plotted as a function of their diameters. The two reference measurements correspond to Savart sheets emanating from the plexiglass and the veroblue non-textured disks whose diameters are respectively 30 mm and 6 mm. The measurements of the droplets diameters are performed at the same Q = 2.8 10^{-5} $m^3.s^{-1}$. The characteristics of droplets are presented in Table 2.1.

In the case of the plexiglass disk, the droplet size distribution has a probability peak corresponding to droplet diameters of 300 μm and the mean droplet diameter D_m is 502 μm. As expected, the droplet distribution is wide and droplet diameters range between 100 μm and 2500 μm. This result is consistent with the measurements of Clanet and Villermaux [9]. The extent of the distribution is corroborated by high STD and CV values that are respectively 318.21 μm and 63 %. Droplets with diameters between 750 μm

Table 2.1: Characteristics of droplets emanating from the disintegration of the Savart sheet in the the cases of the plexiglass and the veroblue non-textured disks.

	Q (10^{-5} m^3.s^{-1})	D_m (μm)	STD (μm)	CV (%)
Non-textured disk: Plexiglass (X = 10)	2.8	502.88	318.21	63
Non-textured disk: Veroblue (X = 2)	2.8	331.24	123.50	37

and 2500 μm have low percentages of probabilities (inferior to 2 %). On the other hand, in the case of the veroblue disk, the droplet size distribution presents a probability peak corresponding to droplets diameters of 250 μm and their percentage is 40 %. Compared to the plexiglass disk, one generates smaller droplets and the D_m is decreased to 331 μm. The droplet size distribution is also tightened and it is highlighted by reduced STD and CV values that are respectively 123.50 μm and 37 %. The production of smaller droplets may be linked to the reduced D that minimizes the friction on the disk surface and hence generating a thin film. However, in this case, it is difficult to justify the difference between the two droplet size distributions since different parameters such as D and the wetting conditions are involved.

Droplets are then characterized in terms of their volumes. In the agricultural spray application field, the droplet size distribution are generally presented by the mean of the cumulative volumes of droplets. Therefore, to facilitate the transition from the presentation of the droplet size distribution in terms of numbers to cumulative volumes, one introduces the Figure 2.10 that presents the relative volume of droplets as a function of their diameters. In the case of the plexiglass disk, the droplet size distribution is wide and droplets range between 100 μm and 2500 μm. The curve has a peak corresponding to droplets whose diameters are 1200 μm with 9% of volume percentages. However, in the case of the veroblue disk, the distribution is less extended and droplet diameters are between 100 μm and 1400 μm. The curve presents a peak corresponding to droplet diameters of 300 μm with 26% of volume percentages.

The Figure 2.11 presents the cumulative relative volumes of droplets as a function of their diameters. The obtained spays are extremely coarse (XC). All configurations are

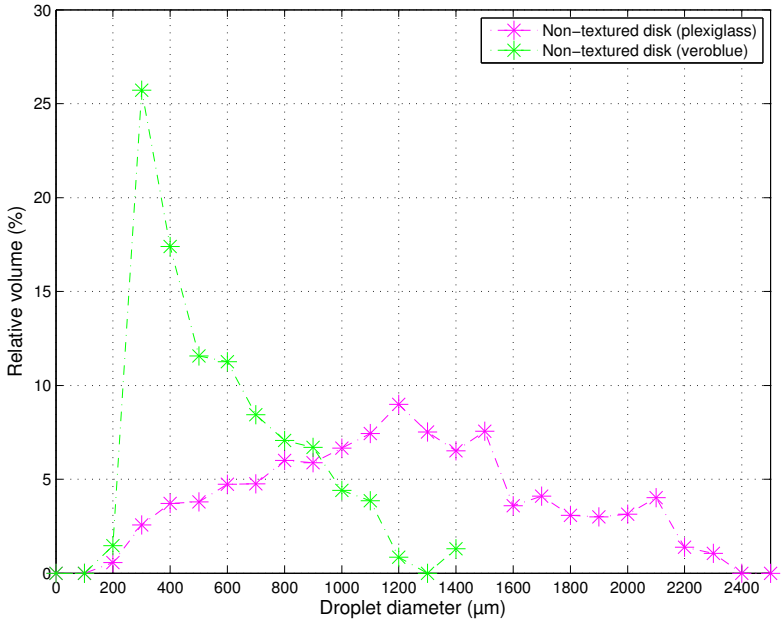

Figure 2.10: Representation of relative volumes of droplets as a function of their diameters. The cases of the plexiglass ($X = 10$) and the veroblue ($X = 2$) non-textured disks are studied

thus compared to a standard agricultural flat fan nozzle that is *Tee jet TP* 65 15 with the same spray class (XC) tested at $Q = 6.9\ 10^{-5}$ m^3.s^{-1}.

For a better readability of curves in Figure 2.11, V_{10}, V_{50}, V_{90}, which indicate respectively that 10 %, 50 % and 90 % of the spray volume is composed of droplets whose diameters are smaller than this value, and the relative span factor *RSF* are presented in Table 2.2.

Table 2.2: Spray characteristics in terms of volumes. All configurations are compared to a reference standard agricultural flat fan nozzle *Tee jet TP* 65 15 within the same spray class (extremely coarse (XC).

	Q (10^{-5} m^3.s^{-1})	V_{10} (μm)	V_{50} (μm)	V_{90} (μm)	*RSF*
Non-textured disk: Plexiglass	2.8	541.82	1205	1921	1.14
Non-textured disk: Veroblue	2.8	269.38	498.29	959.14	1.38
Tee jet TP 65 15	6.9	225	540	928	1.30

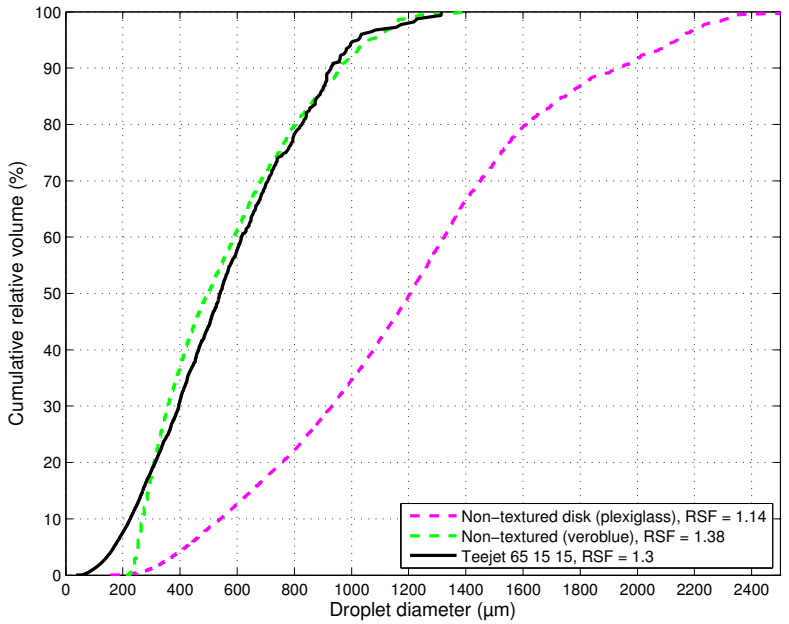

Figure 2.11: Representation of cumulative relative volumes of droplets as a function of their diameters. The cases of the plexiglass ($X = 10$) and the veroblue ($X = 2$) non-textured disks are studied

As expected, the droplet size distributions corresponding to the case of the non-textured disks are wide and the quality of the spray is extremely coarse (XC). The extent of the distribution is corroborated by a high RSF value that is close to that of common hydraulic nozzles (≈ 1). The flat fan nozzle $Tee\,jet\ TP$ 65 15 and the the non-textured disks have the same sheet break up mode and the same spray class (XC). In the case of the plexiglass disk, the V_{50} is 1205 μm and the extent of the distribution is corroborated by a high RSF value of 1.14. However, in the case of the veroblue disk, one generates smaller droplets ($V_{10} = 269\ \mu$m) and the V_{50} is 498 μm. The difference in V_{50} is linked to wetting conditions and disk diameters as explained above. The V_{50} and the RSF in the case of the veroblue disk is similar to those of $Tee\,jet\ TP$ 65 15 despite the difference of flow conditions.

At this stage, no solid comparisons can be established between the tow designs because of the difference in the flow conditions, the wetting properties and disk diameters.

2.4 Conclusion

In this chapter, we introduced the experimental setup based on the impact of a round turbulent jet on a non-textured disk that will be used in the following chapters. Two disk characteristics were used as follows:
- A plexiglass disk with a D = 30 mm and a X = 10 (see also Chapter 3).
- A veroblue disk with a D = 6 mm and a X = 2 (see also Chapter 4).

At the edge of the veroblue disk, the liquid film was ejected with an angle ϕ and formed a Savart sheet of a radius R. The resulted Savart sheet adopts a conical aperture that depends on Q. For low Q values, the sheet is subject to gravity and it adopts a closed / semi-opened bell. As Q increases, the water bell is progressively opened since the inertia dominates. Furthermore, the sheet exhibits random holes that appeared downstream the disk edge. They amplify and lead to the disintegration of the sheet into droplets. On the other hand, one measured the mean velocity U of the flow 1 mm before the plexiglass disk edge through an experimental measurement of the flow thickness h. The mean velocity U rises linearly with the Re for different disk diameters. The flow is slown down when the disk diameter is increased due to the increase of solid friction for a given Re. We have also characterized the droplet size distribution in terms of diameters for the emitted droplets. In both disk configurations the droplet size distribution is clearly wide (Span values are superior to 1).

As a conclusion, the turbulent sheet is interesting with respect to the agronomic application because of the simplicity and the robustness of the disk configuration and the high flow rate ranges that are closed to those applied in the field. The resulted droplets presents a wide size distribution that do not correspond to the target of the precision agriculture. Consequently, the challenge is to find the right alternatives to tame the turbulent regime and hence, fragment the sheet into individual jets.

To meet the agronomic objectives in terms jet numbers and droplet velocities, some crucial points must be taken in consideration in relation to the different textures used to control and to fragment the turbulent sheet into individual jets. At the disk surface, one encounters a semi-free film that is subjected to its velocity deceleration and the formation

of the hydraulic jump. Outside the disk surface, the film is free and is delimited by two factors that are the random holes and its maximum radial expansion that both induce its disintegration into ligaments and droplets of various sizes.

In the following, one uses specific structures in order to taylor the turbulent regime as follows:
- the rectangular grooves in the Chapter 3.
- the triangular textures in the Chapter 4.

3

Perturbation of the semi-free film using grooves

Chapter 3

Perturbation of the semi-free film using grooves

Much efforts were devoted to perturb the dynamics of the liquid film using textured disks. For instance, Taylor investigated the effect of knife cuts grooves that were engraved radially and regularly on the disk surface [11] (Figure 3.1a). The used groove geometry was not able to destabilize the liquid sheet since only cardioids were formed downstream at the liquid sheet surface as drawn in the Figure 3.1b.

In this chapter, we propose to study the impact of deep radial grooves with controlled rectangular shapes. We show that, under given flow conditions, the sheet destabilizes into individual jets. The geometrical parameters of the disk will be tuned as its diameter, the size of grooves (depth, length, width) and their numbers. To obtain enough jets in respect to the agronomic requirement one needs an impact disk of intermediary size (typically $X \sim 10$): large enough to engraved a lot of grooves but small enough to avoid the hydraulic jump.

The present chapter is structured as follows: In the first part, the disk engraved along its circumference by radial grooves in order to induce the split of the film into multiples jets is addressed. Several jet regimes are described through experimental phase diagrams. Then, in the second part, the generated droplets are characterized in terms of diameters and velocities.

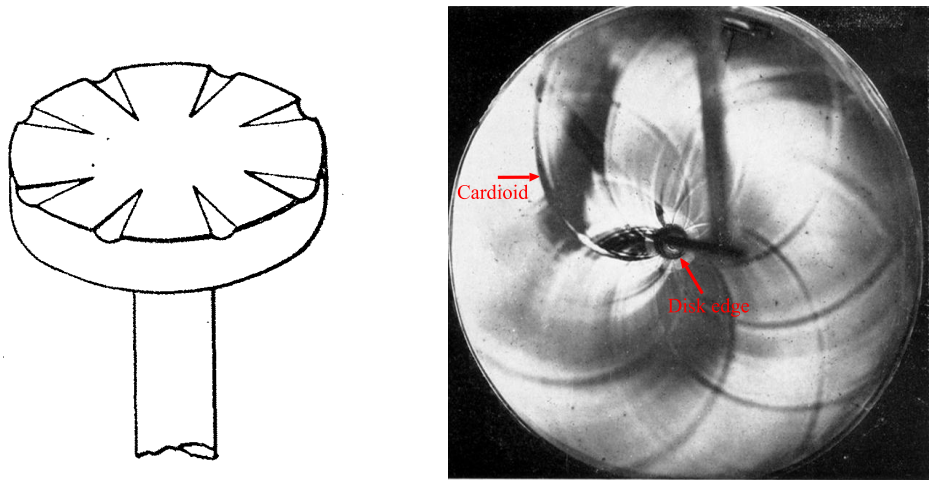

(a) (b)

Figure 3.1: Illustration of the cardioids at the surface of a free Savart liquid sheet within a laminar flow [11]. (a) A disk engraved radially by eight knife cuts grooves. (b) A top view of a Savart sheet resulting from the impact of a round jet on the engraved disk. The sheet exhibits eight cardioids and the used grooves failed to split it into individual jets.

3.1 Material and Method

We used the same experimental setup presented in the Chapter 2 (Figure 2.2). The disk was a plexiglas cylinder cut with a numerically controlled CNC machine. The disk diameter D was fixed to 30 mm that represents a compromise permitting to engrave enough textures and to keep an acceptable flow friction level on the surface (a larger disk would increase the solid friction and would result in a hydraulic jump). The rectangular grooves were regularly engraved downstream at the edge of the top disk surface using the CNC machine (Figure 3.2a). They had a square section of 1 mm side and a length L that was fixed to 5 mm or 2.5 mm (Figure 3.2b). The grooves are considered as open channel and are not completely filled by the liquid because the thickness of the liquid film h is much less than 1 mm. Since the grooves were regularly spaced all over the disk perimeter, the disk geometry can be summarized by the number of grooves N and the length of the groove L. These parameters allow us to define the gap between two successive grooves as the inside circular arc between two successive grooves $d1$ (m): $d1 = [(\frac{D}{2} - L)\frac{2\pi}{N}] - 10^{-3}$ (Figure 3.3).

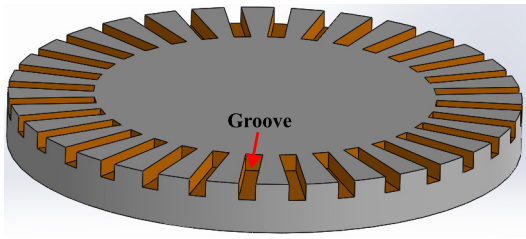

(a)

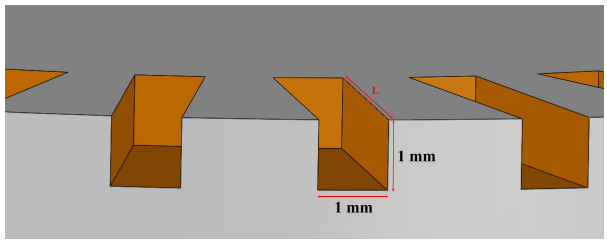

(b)

Figure 3.2: Example of a disk engraved along its circumference by a number N of radial rectangular grooves. (a) Sketch of a disk engraved by $N = 32$ grooves. (b) Zoomed view of the rectangular groove that had a square section of 1 mm side and a length L that was fixed to 5 mm or 2.5 mm.

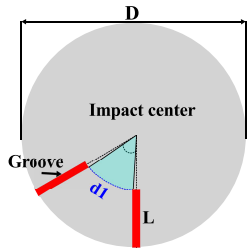

(a)

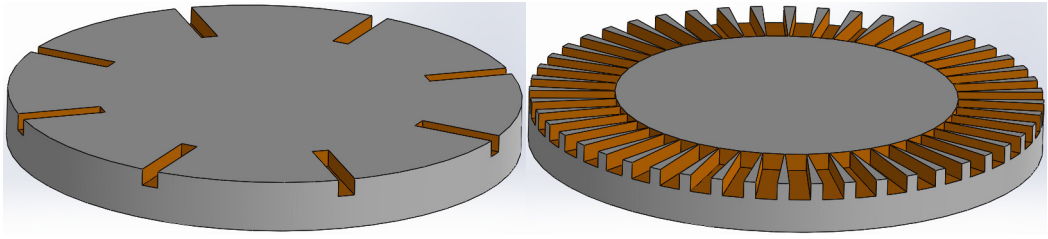

(b) (c)

Figure 3.3: Illustration of the inside circular arc $d1$ (distance) between two successive grooves. (a) This length is given by $d1 = [(\frac{D}{2} - L)\frac{2\pi}{N}] - 10^{-3}$ where D, L and N represent respectively the disk diameter (m), the groove length (m) and the groove number. The experimental sketches (b) and (c) represent engraved disks with radial grooves with $L = 5$ mm where $d1$ values are respectively 6.9 mm ($N = 8$) and 0 mm ($N = 58$).

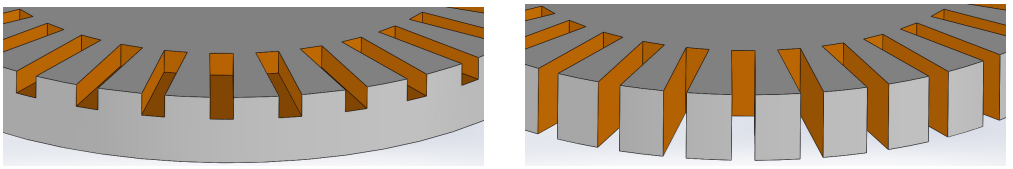

(a) (b)

Figure 3.4: A sketch showing a benchmark between (a) the groove with a square section of 1 mm and (b) the grooves with empty contents (teeth).

One also used other plexiglass disks with the same D = 30 mm and engraved with grooves having empty contents as drawn in the Figure 3.4. In this case, the engraved disks were a plexiglass cylinder cut with a laser cutter (Trotec Speedy 100 TM).

The used liquid was tap water at 20 °C (surface tension $\sigma = 73.5 \pm 0.3$ mN.m^{-1}, density ρ = 1000 kg.m^{-3} and kinematic viscosity $\nu = 10^{-6}$ m^2.s^{-1}). The measured contact angle was 74° (static wetting).

The droplet measurements vary as a function of the disk geometry. In the case of the ungraved plexiglass disk, droplets were measured as soon as they were detached from the sheet (60 mm from the disk edge) in order to avoid merged droplets. In the case of the engraved disk, droplets were measured as soon as they were detached from the jet (6 mm from the disk edge).

3.2 Impact on a structured disk

3.2.1 From a Savart sheet to liquid jets

In the case of a non-textured disk, the jet impact on the disk center resulted as expected in a liquid film that flowed radially, exceeded the disk border and lead to a savart sheet depending on Q. As the jet flow is turbulent at the impact, disturbances were occured in the film and resulted in random holes that appeared downstream the disk border. These holes were amplified and lead to the disintegration of the liquid sheet.

By engraving the grooves on the top disk, one manages to break up the liquid film before it reached the disk edge. Therefore, the radial film dynamics were modified and several

liquid jets at the disk border were observed. Varying $d1$ and Q, four regimes of jet are observed and they are classified by the number of emitted jets n as shown in the Figure 3.5. The number of jets n is either stable or fluctuating.

In the case of a stable n, two regimes are obtained. The first regime represents the case where all the liquid is entrapped in the grooves leading to a one jet per groove. Therefore, the number of jets n is equal to N. The second regime is characterized by the presence of secondary jets emitted between two successive grooves in addition to the emission of main jets from grooves. The two jet types are not emitted in the same plane and the jet number n is equal to $2N$. In the case of the number of jets n fluctuates, two regimes are also observed. The first regime represents the case where the secondary jets may locally merge with the main jets and leading to a mixed zone ($n = N_1^*$). The number of jets n is between N and $2N$. Finally, even main jets may coalesce and an other mixed zone is formed ($n = N_2^*$). The number of jets n is lower than N and greater or equal to $\frac{N}{2}$. The jet coalescence is elastic in both cases what explains the fluctuation of the number of jets n [52].

A specific symbol for each regime is defined in the Figure 3.5 and these symbols are used to describe the following phase diagrams.

3.2.2 Phase diagrams

In order to understand the transition between the observed regimes, we have established phase diagrams by varying Q, L and $d1$. The first tested configuration is based on grooves with L = 5 mm (Figure 3.6). The different regimes are plotted as a function of $d1$ and Q. Each $d1$ corresponds to an engraved disk. Below a critical value $d1$ (= 0.12 mm), jets are only emitted from the grooves ($n = N$). The gap between two successive grooves is so small that the liquid is forced to pass through the grooves. When Q exceeds 3.6 10^{-5} $m^3.s^{-1}$, main jets may merge elastically and n fluctuates between $\frac{N}{2}$ and N ($n = N_2^*$ regime). In the case of high $Q >> 4.1\ 10^{-5}$ $m^3.s^{-1}$ and remaining below the threshold value in $d1$, the coalescence between jets increases and the liquid film is no longer broken up on the disk into jets. As a result, a Savart sheet is formed and it adopts cardioids structures at its surface and therefore the regime of Taylor is found [11]. For

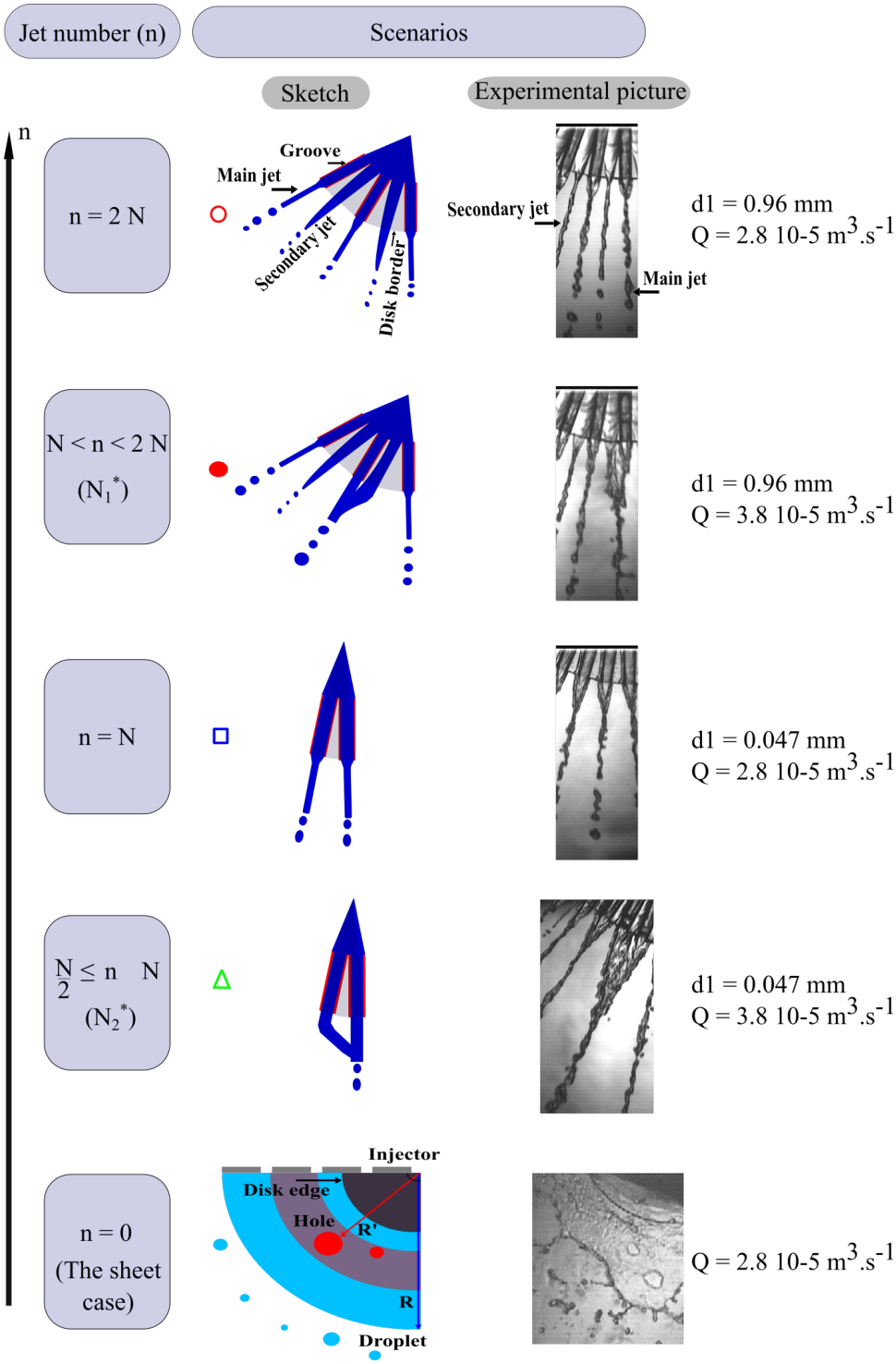

Figure 3.5: Different regimes of the liquid behavior on the disk depending on $d1$ and Q. These regimes are classified as a function of the emitted jet number n. A specific symbol is given for each regime.

medium $d1$ values (0.12 mm $< d1 <$ 0.42 mm), main and secondary jets interact together leading to elastic coalesce ($n = N_1^*$ regime). This behavior is observable for all Q ranges in this regime. For high $d1$ values ($>$ 0.42 mm), main and secondary jets do not interact together and the jet number n is stable et is equal to $2N$. The secondary jets and main jets may merge with the increase of Q leading to $n = N_1^*$ regime (mixed zone).

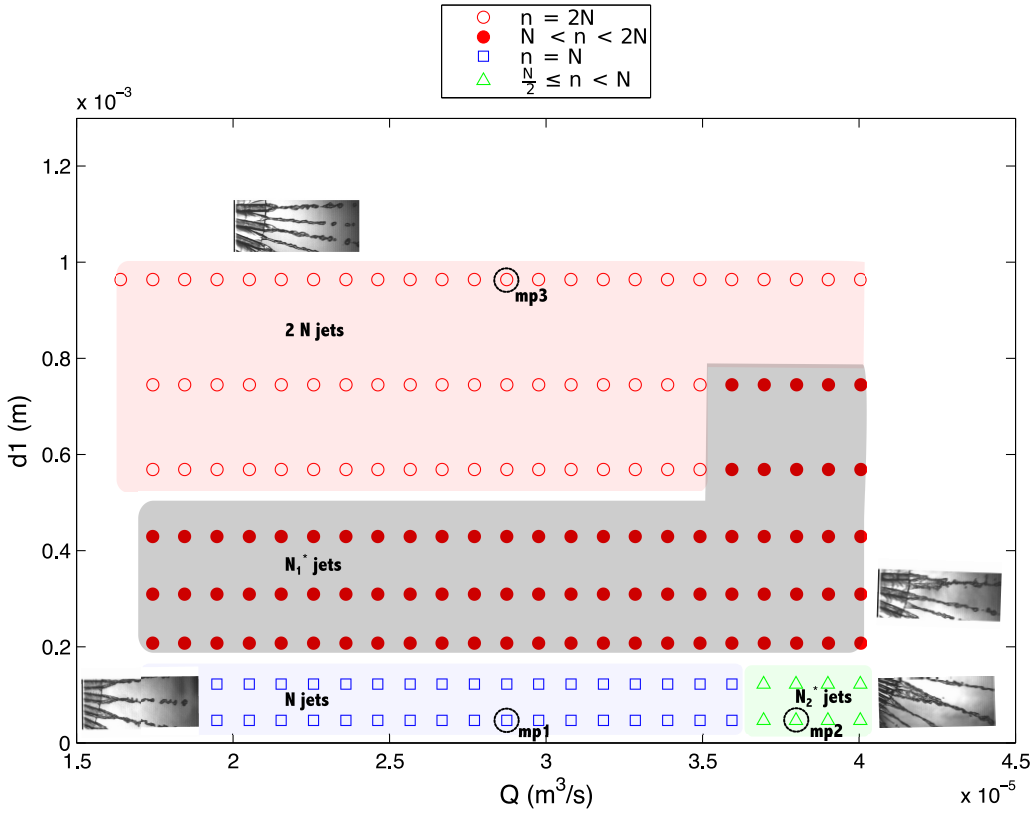

Figure 3.6: Representation of different regimes as a function of $d1$ (m) and Q (m^3.s^{-1}). The groove length was 5 mm and the disk diameter D was 30 mm. Three measurement point of the droplets properties (see paragraph 5) were performed and were designed as $mp1$, $mp2$ and $mp3$.

The origin of secondary jets comes from the destabilization of the liquid film by the grooves on the disk. Indeed, in the case of $n = 2N$ ($d1 >$ 0.12 mm) and for medium Q values, the groove destabilizes the radial turbulent flow that becomes tangential next to the groove edge and hence one triggers its break up before reaching the disk border. The destabilization conducts to the de-wetting of the disk. In the Figures 3.7a and 3.7c, a close-up of the disk shows that the secondary jet is surrounded by dry regions along the grooves

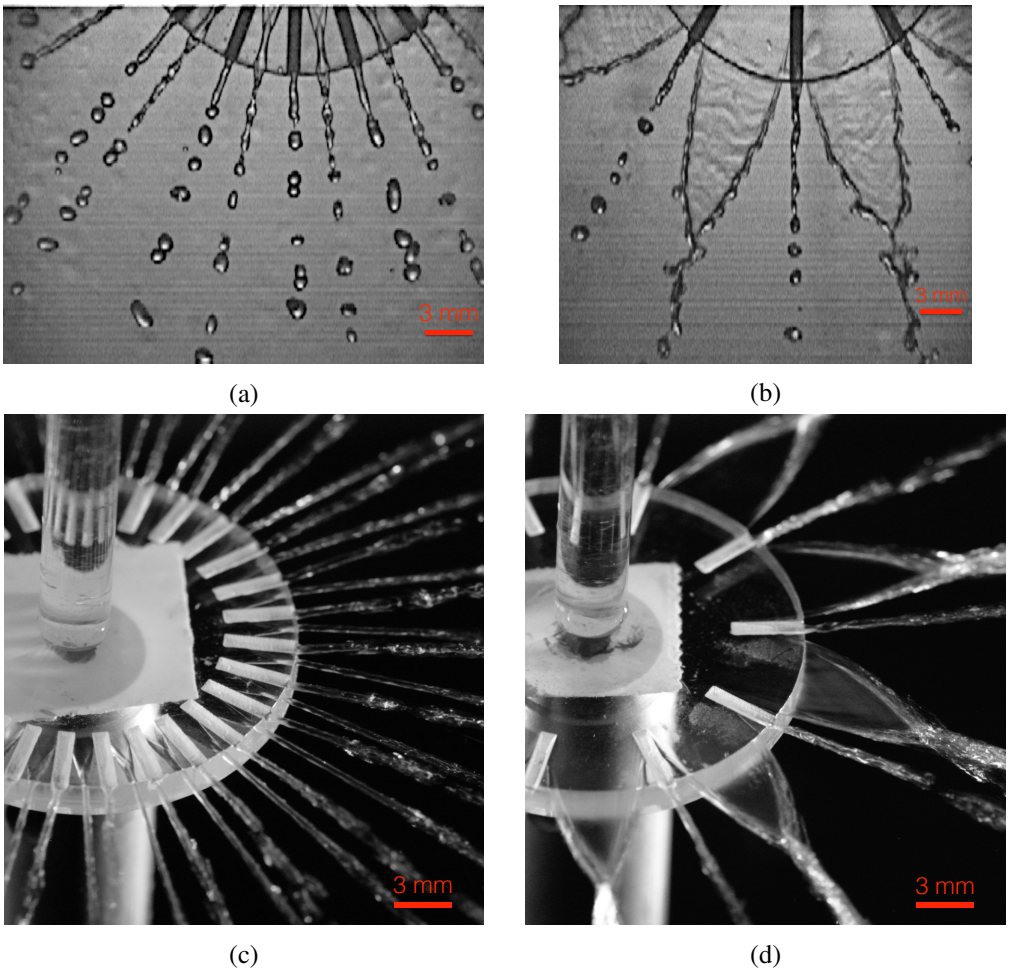

Figure 3.7: Snapshots of the $n = 2N$ regime: (a) and (c) The parameters are $d1$ = 1.3 mm and Q = 1.8 10^{-5} $m^3.s^{-1}$. The secondary jets are clearly seen between two successive grooves. The de-wetting zone is well pronounced. (b) and (d) The parameters are $d1$ = 2.5 mm and Q = 2.8 10^{-5} $m^3.s^{-1}$. Between two successive grooves, the sheet can be found and it collapses into droplets

before being ejected out of the disk. The destabilization of the sheet prior its ejection out of the disk can be also visualized when $d1$ is large. In the Figures 3.7b and 3.7d, between two successive grooves, a secondary jet is observed. The secondary jets are first liquid sheets as large as the distance between two successive grooves. The turbulent film do not trigger perforations in the formed sheet. The flow inside this sheet is no longer radial as before the interaction with the grooves but also tangential. These tangential contributions lead to the convergence of the sheet into a jet.

The second configuration is based on a groove length reduced by a factor one half from the previous configuration, i.e. L = 2.5 mm. It allows to increase the number of engraved grooves for a disk of the same diameter. The different regimes are also plotted as a function of $d1$ and Q in the Figure 3.8. The transition between the $n = N$ regime and the merged zone $n = N_1^*$ occurs for the same $d1$ threshold value as seen in the configuration 1. This fact confirms that main jets are only obtained when the grooves upstream corners are close enough. Then, the transition to $n = N_2^*$ zone is observed for a Q value lower than the one observed in the configuration 1. Moreover, the reduction of the groove length conducts to an expansion of the mixed zone $n = N_1^*$ as it occurs for $d1$ values from 0.2 mm to 0.8 mm. Hence, one states that the transition between the $n = N_1^*$ and the $n = 2N$ regimes is mainly fixed by the groove length L since the vertical transition happens almost for the same Q but with a factor 2 in $d1$ for the horizontal transition. This factor 2 corresponds to the inverse variation in L between the two tested configurations. Furthermore, the $n = 2N$ zone is reduced and is observed for $d1$ values superior to 0.8 mm. For high Q, main and secondary jets are destabilized and some of them interact together leading to elastic coalescences.

To conclude, one can evidence general behaviors and trends. According to the presented results, the generation of individual jets guided by grooves is linked to the groove geometry as well as the gap $d1$ between them. Below a threshold in $d1$, one can observe that the incident radial flow is forced to follow the grooves and therefore be guided through these grooves regardless their length L. An other important result is that the reduction of the groove length allows to increase the number of emitted jets. However, this length reduction conducts to a lower main jet stability and leads to elastic coalescence phenomena between main and secondary jets. On the other hand, in the confluence region (elastic merging), the resulting jet is excited at a scale defined by the sizes of the incident jets what may increase the noise generated by surface roughness manifested by corrugations. These corrugations constitute the elastic connections areas between two very close jets and hence it affects the number of jets [53].

The resulted jets (case of the engraved disks) or sheets (case of the ungraved disk) disintegrate then into droplets. The droplet characteristics in terms of diameters and velocities are addressed in the following section.

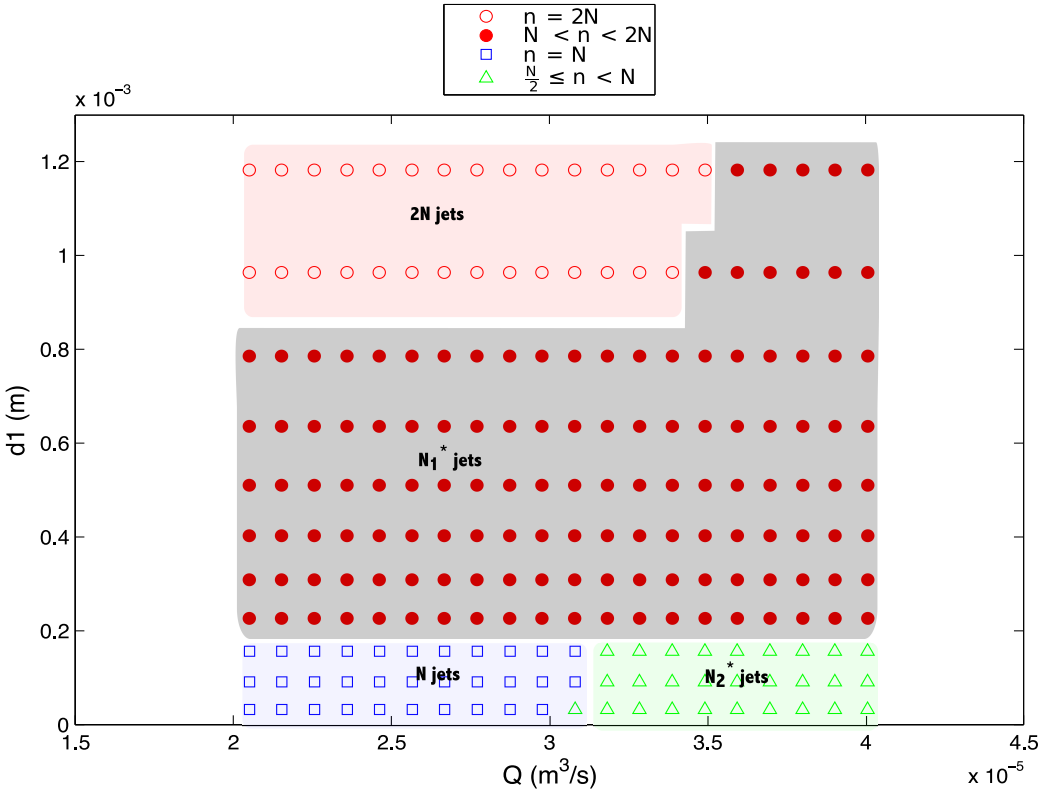

Figure 3.8: Representation of different regimes as a function of $d1$ (m) and Q ($m^3.s^{-1}$). The groove length was 2.5 mm and the disk diameter D was 30 mm.

3.2.3 Droplets

3.2.3.1 Droplets diameters

Droplets emitted from the sheet (case of the ungraved disk) and jet breakups were investigated in terms of diameters. The configuration of the engraved disk with $L = 5$ mm is only addressed. The jet regime affects the spray characteristics. Thus, three measurement points on the phase diagram $mp1$, $mp2$ and $mp3$ that correspond respectively to $n = N$ jet zone, $n = N_2^*$ jet zone and $n = 2N$ jet zone are performed. For a better understanding of the impact of the groove geometry on spray characteristics, one adds a design similar to that tested in $mp3$ but with empty grooves (Figure 3.4). Characteristics of measurement points are shown in Table 3.1.

Table 3.1: Characteristics of measurement points of different regimes.

	$d1$ (mm)	Q (10^{-5} m^3.s^{-1})	Jet regime
Ungraved disk	-	2.8	sheet
$mp1$	0.047	2.8	$n = N$
$mp2$	0.047	3.8	$n = N_2^*$
$mp3$	0.963	2.8	$n = 2N$

The Figure 3.9 presents the probability density function (PDF) of droplets where droplets percentages are plotted as a function of their diameters for three measurement points $mp1$, $mp2$ and $mp3$. The reference measurement corresponds to droplets emitted from the liquid sheet in the case of the ungraved disk (D= 30 mm). Characteristics of droplets corresponding to different measurement points are shown in Table 4.5.

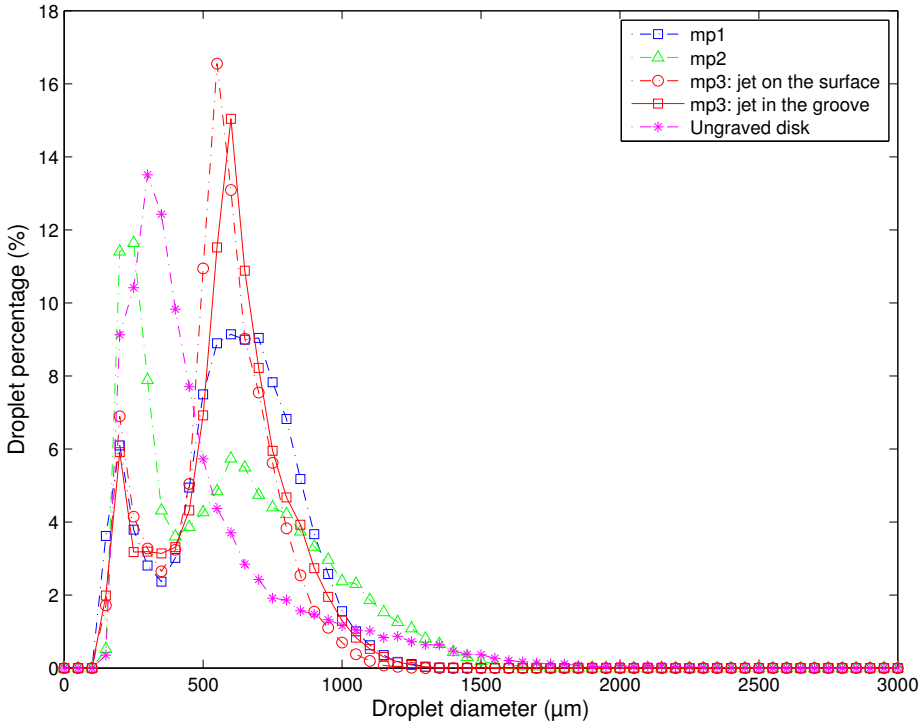

Figure 3.9: Representation of droplet percentages as a function of their diameters for three measurement points $mp1$, $mp2$ and $mp3$. The curve *ungraved disk* corresponds to droplets emitted from the liquid sheet (disk without grooves).

In the case of the *ungraved disk*, the droplet size distribution has a probability peak

corresponding to droplet diameters of 300 μm and D_m = 502 μm. As expected, the droplet distribution is wide and droplet diameters range between 100 μm and 2500 μm. This result is consistent with the measurements by Clanet and Villermaux [9]. The extent of the distribution is corroborated by high STD and CV values that are respectively 318.21 μm and 63 %. Droplets with diameters between 750 μm and 2500 μm have low percentages of probabilities that are inferior to 2 %. Once the disk is engraved radially with grooves, the sheet break up regime is no longer valid and the jet break up regime occurs. For all measurements involving an engraved disk, i.e. $mp1$, $mp2$ and $mp3$, the droplet size distribution is narrower than that of the *ungraved disk*. In these regimes, the droplet size distribution adopts a bimodal shape characterized by two probability peaks. The first peak which is the highest corresponds to main droplets of the spray and the lowest probability peak corresponds to the population of secondary droplets. For all measurement points ($mp1$, $mp2$ and $mp3$), the peak of secondary droplets is close to the main peak of the droplet population emitted in the case of the *ungraved disk* but it is less pronounced than the *ungraved disk* case. Droplet diameters exceeding 1100 μm have very low percentages and correspond almost to merged droplets which is not always the case for the case of the *ungraved disk*; these big droplets correspond to non-spherical ligaments or beads.

Table 3.2: Characteristics of droplets corresponding to different measurement points.

	D_m (μm)	STD (μm)	CV (%)
Ungraved disk	502.88	318.21	63
$mp1$	596.28	228.35	38
$mp2$	582.54	319.28	55
$mp3$: jet on the surface	549.22	190.37	35
$mp3$: jet in the groove	584.82	209.09	36
$mp3$ (empty groove): jet on the surface	550.49	188.83	34
$mp3$ (empty groove): jet in the groove	640.66	227.02	35

For the measurement point $mp1$ (corresponding to $n = N$ jet regime), the main droplet population is centered on a droplet diameter value of 600 μm and the secondary droplet population is characterized by smaller droplets with diameters close to 200 μm. The reduced droplet size distribution is highlighted by low STD and CV values which are respectively 228.35 μm and 38 %.

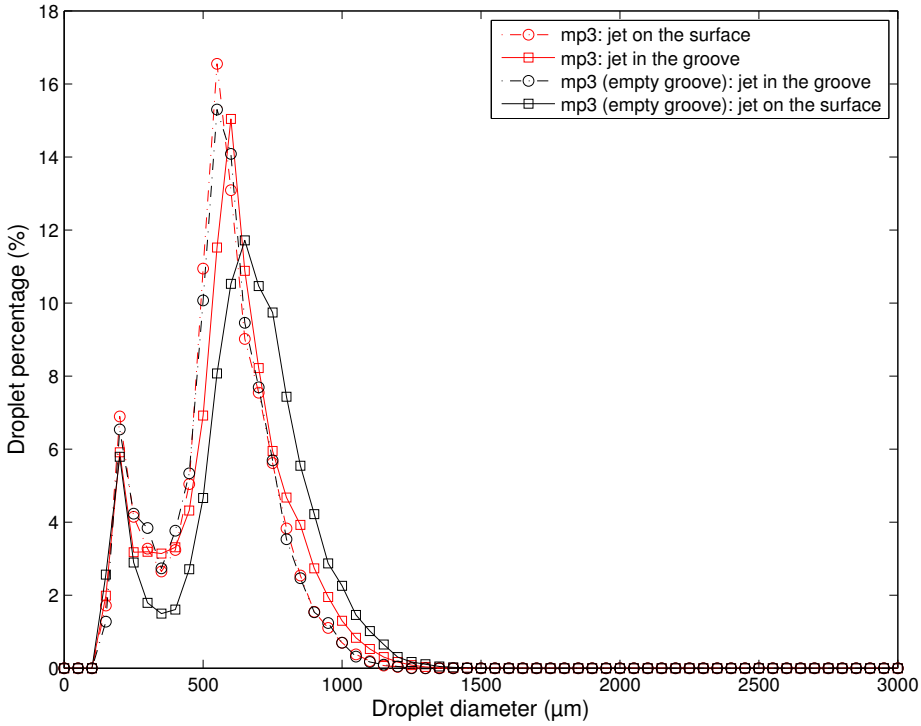

Figure 3.10: Representation of droplet percentages as a function of their diameters for the case $mp3$. We investigate two disk designs with different geometrical shapes: a disk with grooves having a square section of 1 mm side and a disk with empty grooves.

Moreover, for the case $mp2$ which corresponds to an increase of Q and a transition to $n = N_2^*$ jet regime characterized by inelastic coalescences, the PDF curve keeps the same shape as in $mp1$ with two distinct droplet populations. In contrast with $mp1$, one observes an increase of the probability peak of secondary droplets to 11.5 % while the probability peak of main droplets decreases to 5.7 %. As a result, the mean droplet diameter D_m is reduced to 582 μm. The increase of the amount of small droplets is due to droplets obtained from inelastic collisions between neighboring jets which conduct to more small droplets created by other phenomenon than the Plateau-Rayleigh destabilization. This droplet size distribution is highlighted by high STD and CV values that are respectively 319.28 μm and 55 %. The decrease of D_m with the increase of Q corresponds to that of Clanet and Villermaux [9].

For the measurement point $mp3$ (corresponding to $n = 2N$ jet regime), one investigates separately droplets resulting from the breakup of both jets: jets emanating from the groove

and jets emanating from the gap between two neighboring grooves. In the first case where jets are ejected from grooves (that is similar to the case of $mp1$), as expected, the PDF curve has a similar trend as that obtained in $mp1$. However, the obtained droplet size distribution is slightly tightened as that in $mp1$ and it shows low STD and CV values that are respectively 209.09 μm and 36 %. In the second case where jets are directly ejected from the disk surface, the pdf is similar to the previous case with the jet in the groove ($mp3$). One notices a slight decrease of D_m to 549 μm and also a slight narrowing of the droplet size distribution that conduct to low STD and CV values which are respectively 190.37 μm and 35 %. The main probability peak is the highest and it reaches a maximum of 16.7 %. This difference in D_m value is linked to the shape of the emitted jet that is influenced by the change of boundary conditions on the disk surface i.e. the jet emitted between the grooves is only influenced by same boundary conditions (characterized by the friction and the wetting property) while the jet which passes through the groove is subjected to a brutal change of boundary conditions since the jet leaves the surface and fall down into the groove. As a result, this change has an effect on the velocity of the flow that is discussed below. For a better understanding of the influence of boundary conditions of the flow in the groove, we investigate the design $mp3$ with empty grooves as explained above. One notices a slight increase of both D_m and STD value to respectively 640 μm and 227.02 μm (Figure 3.10).

Following the Plateau-Rayleigh instability, one can expect that the D_m is close to 1.89 mm for droplets emitted from a jet issued from a 1 mm side square section groove. The discrepancy between this expected D_m and the measured ones can be explained by the fact that the grooves are not totally filled by the liquid and thus the liquid ejected from the grooves converges in jets smaller than the output grooves sections.

In the following, droplets are characterized in terms of their volumes. The Figure 3.11 presents cumulative relative volumes of droplets as a function of their diameters. Obtained spays are extremely coarse (XC). All configurations are thus compared to a standard agricultural flat fan nozzle that is *Teejet TP* 65 15 with the same spray class (XC) tested at Q = 6.9 10^{-5} $m^3.s^{-1}$. For a better readability of curves in Figure 3.11, V_{10}, V_{50}, V_{90}, which indicate respectively that 10 %, 50 % and 90 % of the spray volume is composed of droplets whose diameters are smaller than this value, and the relative span factor RSF are presented in Table 3.3.

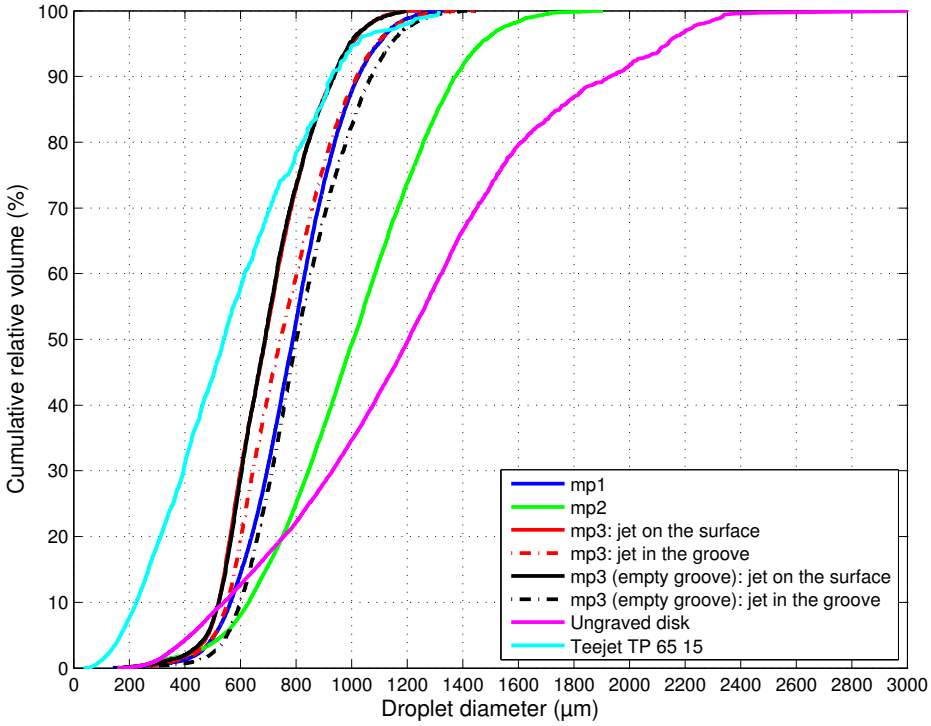

Figure 3.11: Representation of cumulative relative volumes of droplets as a function of their diameters. Measurements correspond to droplets emitted by the sheet in the case of the ungraved disk and by jets emanating from different scenarios of the liquid sheet on the engraved disk. The measurements points mp1, mp2 and mp3 correspond respectively to n = N, n = N*1 and n = 2 N regimes. These cases are compared to a reference standard flat fan nozzle Teejet TP 65 15 within the same spray class (XC).

As expected, the droplet size distribution corresponding to the case of the *ungraved disk* is wide and the quality of the spray is extremely coarse (XC) where the V_{50} is 1205 μm. The extent of the distribution is corroborated by a high *RSF* value of 1.14 that is close to that of common hydraulic nozzles ($\approx$ 1). The flat fan nozzle *Teejet TP* 65 15 and the *ungraved disk* have the same sheet break up mode and the same spray class. However, the flat fan nozzle generates finer droplets that is due to the difference of flow conditions where the V_{50} is 540 μm. The droplet size distribution is also wide and it is highlighted by a *RSF* of 1.30.

As indicated above, engraved grooves induce a change in the liquid breakup regime from a sheet break up regime to a jet break up regime. For all configurations involving an engraved disk, i.e. $mp1$, $mp2$ and $mp3$, droplet size distributions become narrower than the

Table 3.3: Spray characteristics in terms of volumes corresponding to different measurement points. All configurations are compared to a reference standard agricultural flat fan nozzle *Tee jet TP* 65 15 within the same spray class (extremely coarse (XC).

	Q (10^{-5} m^3.s^{-1})	V_{10} (μm)	V_{50} (μm)	V_{90} (μm)	*RSF*
Ungraved disk	2.8	541.82	1205	1921	1.14
*mp*1	2.8	564.6	789.2	1025.7	0.58
*mp*2	3.8	629.88	1007.7	1375	0.74
*mp*3: jet on the surface	2.8	521.66	690.09	934.24	0.6
*mp*3: jet in the groove	2.8	553.93	745.23	1021	0.63
*mp*3 (empty groove): jet on the surface	2.8	522.33	688.8	935.82	0.6
*mp*3 (empty groove): jet in the groove	2.8	601.64	802.64	1071.9	0.59
Tee jet TP 65 15	6.9	225	540	928	1.30

case of the *ungraved disk* and the *Tee jet TP* 65 15. As a result, *RSF* values are reduced to 0.5 - 0.7 that are similar to those of sprays emitted by Controlled application applicators. Droplet size distributions are shifted towards smaller droplets due to the different break up regimes. Hence, the V_{50} is reduced compared to that of the *ungraveddisk* but it is larger than the V_{50} of the nozzle reference due to the difference of flow conditions and the groove geometry. It is noticed that the percentage by volume of small droplets is underestimated because of the intrinsic computation of the cumulative volume of droplets compared to the droplets percentage by numbers.

For the *mp*1, the droplet size distribution is centered on a V_{50} of 789 μm and it presents a *RSF* value around 0.58. Besides, for the *mp*2 which corresponds to an increase of Q and a transition to $n = N_2^*$ jet zone, the curve keeps the same shape as in *mp*1 and the V_{50} increases to 1007 μm. However, in contrast with *mp*1, the V_{10} increases from 564 μm to 629 μm due to inelastic coalescence. Therefore, the droplet size distribution is slightly extended and it is highlighted by *RSF* value around 0.74. For the *mp*3 where jets are ejected from grooves (that is similar to the case of *mp*1), the CDF curve keeps also the same shape as in *mp*1 and the droplet size distribution is centered on a V_{50} of 745 μm. The distribution is more tightened and it has a *RSF* value of 0.55. When jets are ejected from the disk surface, the obtained V_{50} is reduced to 690 μm. This result may be explained by the fact that the secondary jet emitted between the groove gap is less noisy than the liquid

guided by the groove. Compared to the case $mp3$ where the jets are ejected from empty grooves, the V_{50} is increased to 802 μm due to the friction in the groove geometry that result in more big droplets (Most of the explanation comes from the analysis of the speed).

3.2.3.2 Droplet velocities

Droplet velocities are computed for all configurations involving an engraved disk, i.e. $mp1$, $mp2$ and $mp3$. The Figure 3.12 presents average droplet velocities as a function of their diameters. Each velocity per diameter class corresponds to the average velocity of at least 15 droplets. For all configurations, the velocity curve is divided in two parts: One observes an abrupt slope of the curve for droplet diameters inferior to 400 μm. Then, droplets have almost constant velocities. The first increasing part can be understood as the diminution of the air friction contribution to the drop motion when the droplet diameter increases.

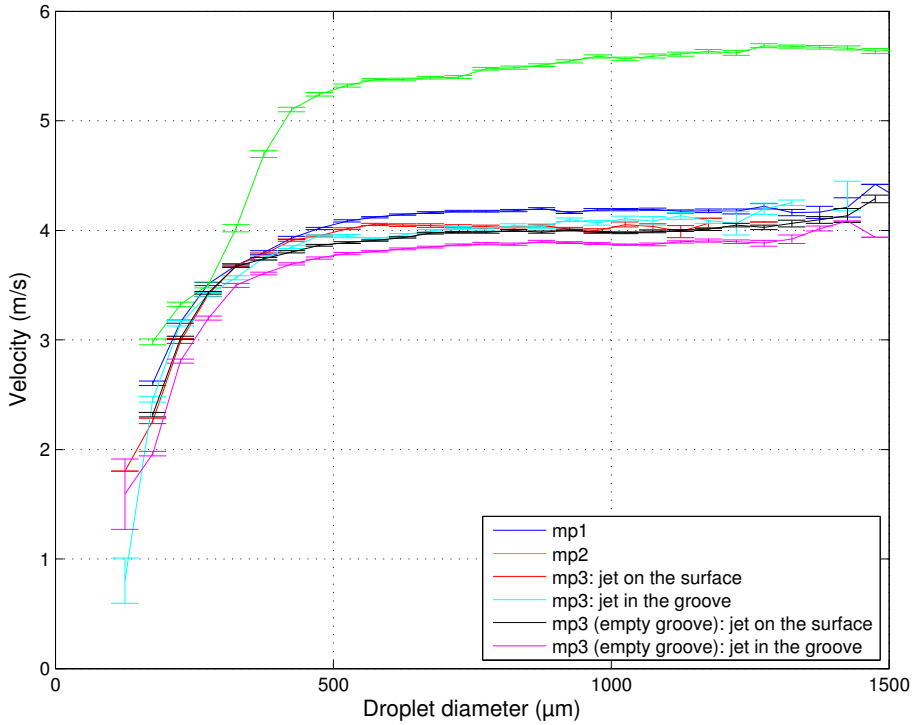

Figure 3.12: Representation of droplets velocities as a function of their diameters.

For $mp1$, jets are only generated from grooves and droplet velocities are around 4.2 m.s^{-1} that are the highest observed speed among the studied cases. Compared to the case $mp3$ where jets are generated from the disk surface, droplet velocities are slightly smaller. This difference is probably due to that the jet emitted between the groove gap is only influenced by initial boundary conditions of the disk surface that are the friction and the wetting property. Hence, the jet is always a semi-free film that is subject to a permanent friction on the surface what explains its deceleration. However, the jet which passes through the groove geometry is subjected to a brutal change of boundary conditions; the jet pass from a semi-free film (at the groove entry) to a free film by leaving the groove thanks to inertia and finally, it finishes by falling down on the basis of the semi-open groove to become again a semi-free film. This quick change in the boundary conditions may be the origin of the slight difference in terms of velocities between the two previous configurations. Besides, in the case of jets emitted from grooves ($mp3$), droplet velocities are slightly decreased compared to velocities in $mp1$. This result is probably linked to wetting properties of the surface basis of the semi-open groove that are affected by the cut process. In a purpose of a better understanding of the groove effect on the velocity, the groove was fully empty (open groove). As a result, droplet velocities are decreased compared to $mp1$ and $mp3$: *jet in the groove*. One finds a small liquid sheet evolving in the air but it is subjected to the effect of two parallel surface of the groove that increase the friction.

For $mp2$ which corresponds to an increase of Q, droplets velocities increase and reach 5.5 m.s^{-1}.

To conclude, by inserting grooves on the disk circumference, the sheet break up regime is no longer valid and the jet break up is established. Droplet size distributions present a bimodal aspect reflecting two droplet populations. This bimodal aspect is probably linked to the jet behavior i.e. the obtained droplet sizes ($\approx$ 600 - 800 μm) and velocities ($\approx$ 4 m.s^{-1}) correspond to jet fragmentations in the Plateau-Rayleigh regime (see Figure 1.5). However, these jets are subjected to external perturbations that are due to the change of the flow expansion from radial to tangential and to the capture of the flow in a specific geometry (groove or gap). Hence, jets are not circular (like capillary jets) and look like small triangular liquid sheets that decompose into liquid beads. As a consequence, secondary droplets are emitted in addition to main droplets from both jets emanating either from the gap or from the groove.

3.3 Conclusion

This study investigates a turbulent round water jet impacting a motionless disk engraved along its circumference by a number N of radial grooves. In the case of an ungraved disk, a semi-free thin film flows radially on the surface, leaves the disk edge thanks to its inertia and leads to a free Savart liquid sheet characterized by holes (due to the turbulent regime). By the insertion of grooves, one tames the turbulent flow and the film splits into several smaller liquid jets before reaching the disk edge. Phase diagrams presented as a function of the distance $d1$ between two grooves and the flow rate Q highlight the transition between jet regimes ($n = 2N$, $n = N_1^*$, $n = N$ and $n = N_2^*$). The $n = N$ jet regime is directly linked to the disk geometry and particularly to the space between grooves. In the case of $n = 2N$, jets are emitted in two different planes that is a favorable parameter to avoid jet coalescences. The reduction of the groove length generates a large number of jets. However, elastic coalescences between main and secondary jets are favoured. Furthermore, droplets are characterized in terms of their diameters and velocities. The quality of obtained sprays are extremely coarse and they are compared to the standard flat fan nozzle *Tee jet TP* 65 15 with the same spray class. For all configurations including an engraved disk, the obtained droplet size distribution is narrower compared to the ungraved disk and to the standard flat fan nozzle. The V_{50} is reduced towards smaller droplets (from 1200 μm in the case of the ungraved disk to 700 - 800 μm in the case of the engraved disk configurations) but it is still coarse compared to that of the *Tee jet* nozzle. With the current designs (L = 5 mm), one generates 72 jets over 360° that are too few compared to agricultural recommendations in terms of jet numbers ($\approx$ 111 jets corresponding to a Q = 1.66 10^{-5} $m^3.s^{-1}$). One can increase the jet number by reducing the width of the groove or increasing the distance from the inlet. However, in the latter case, one is facing to the quick flow deceleration induced by the surface friction.

To sum up, by introducing the grooves, one can taylor the turbulent liquid film by splitting it into individual jets (under specific conditions of Q, L and $d1$) and removing the holes downstream. However, the difficulty level is extremely high to meet the desired jet numbers and velocities since we are limited by the size of the groove and the quick deceleration of the film on the surface. Consequently, reducing the disk diameter as much

as possible while ensuring the formation of the Savart sheet and splitting it using specific structures will be the right alternative to reach our objectives.

4

Perturbation of the free Savart sheet using triangular prisms

Chapter 4

Perturbation of the free Savart sheet using triangular prisms

In this chapter the Savart sheet is fragmented into jets by creating local disturbances out of the disk circumference. This way of doing is totally original. We propose to investigate the influence of triangular textures put in the free turbulent Savart sheet downstream the disk border. We will show that, under given flow conditions and geometrical parameters of theses textures, the sheet split into individual jets. The geometrical parameters of the disk configuration will be tuned as the disk diameter, the size of triangular textures and their numbers. To obtain enough jets, one needs a disk diameter of small size (typically $X = 2$): small enough to reduce as much as possible the surface friction but large enough to allow the formation of the Savart sheet.

The chapter is structured as follows: In the first part, the case of triangular textures used to split the turbulent sheet into jets. One introduces a geometrical model that explains the generation of individual jets through theses structures. In the second part, the emitted droplets are characterized in terms of diameters and velocities.

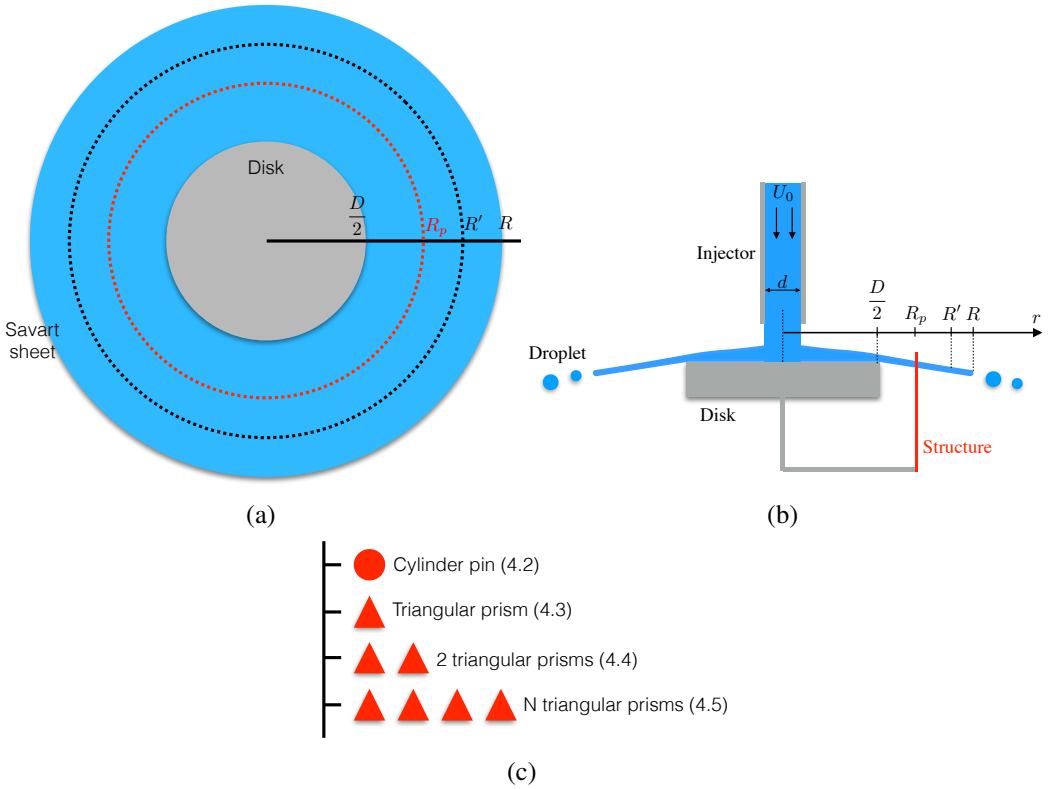

Figure 4.1: (a) Top view and (b) side view of the turbulent Savart sheet evolving in the air perturbed by specific structures. (c) Cross section of the used structure to tame the turbulent sheet. One firstly tested a simple circular pin, a triangular structure and an assembly of triangular structures.

4.1 Material and Method

We used the experimental setup presented in the Chapter 2 (Figure 2.2). The disk was made with a veroblue print polymer using a 3D printer (Objet30 Prime TM). The disk diameter D was fixed to 6 mm and $X = 2$. The value of D was a compromise with regards to the flow velocity and the development of the Savart sheet i.e. the disk diameter must be small enough to minimize the radial flow deceleration due to the increase of friction effects close to the surface but large enough to ensure the formation of the Savart sheet. The measured contact angle was 25° (static wetting).

As a reminder, one aims to break up the sheet into jets using specific structures placed downstream the disk border (Figures 4.1a and 4.1b). In order to meet this objective, one

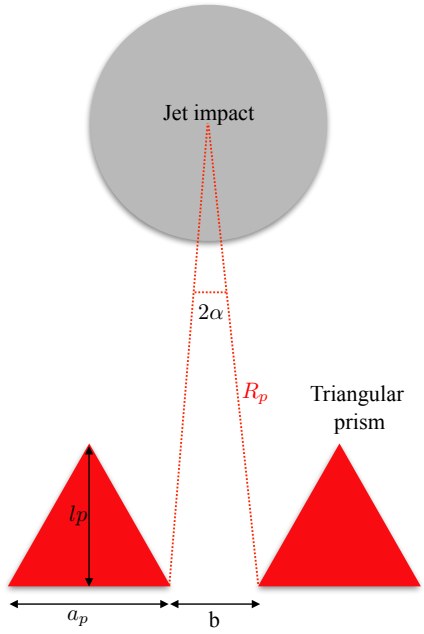

Figure 4.2: A number N of triangular prisms were placed in the sheet at a radial distance r from the jet axis. The prism is characterized by a base a and a perpendicular bisector l to the base. One defined the angle 2α and the distance b between two successive prisms.

established the following strategy. From a single basic case, one increased the complexity. One tested the effect of a simple circular pin, a triangular prism structure and an assembly of triangular prism structures on the sheet behavior (Figure 4.1c).

All the tested structures were made of 3D veroblue print polymer. They were set directly in the sheet and perpendicular to the disk surface plan at a radial distance from the injector axis. This radial distance is strictly greater than $\frac{D}{2}$ and less than or equal to R' (for which the holes appear in the sheet) or to R since one finds in some cases $R' = R$ (See Figure 2.7 in Chapter 2) .i.e the holes disintegrate the entire sheet. The first tested structure was a pin cylinder with a diameter of 300 μm. The second structure was a triangular prism with a top surface having the shape of an isosceles triangle. Its base a_p is variable while l_p, the perpendicular bisector to the base, is fixed to 2.5 mm (Figure 4.2). Then, N triangular prisms were placed radially in the sheet. One defined the angle 2α and the distance b between two successive prisms (Figure 4.2).

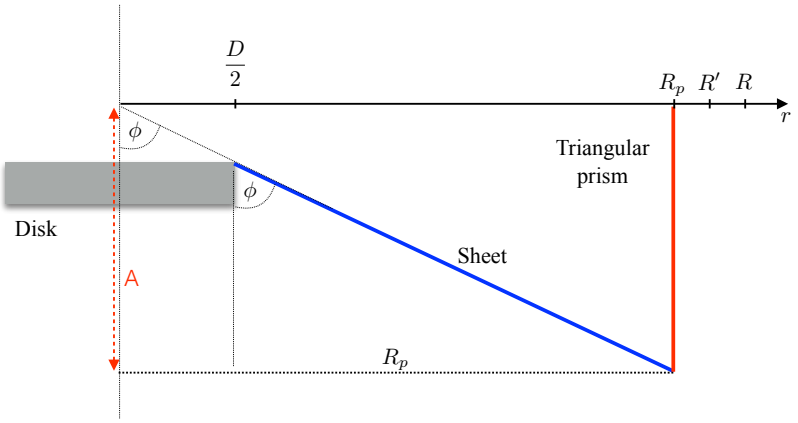

Figure 4.3: A sketch of the Savart sheet emitted with a ϕ angle and impacted the triangular prism structure. The length of the triangular A depends on ϕ and on the distance R_p of the prism in the sheet from the jet impact.

The length of the triangular prism A is influenced by the behavior of the conical shape of the Savart sheet that depends on Q (See Chapter 2). The length A must be large enough for the sheet to impact the textures. The minimum value of A is equal to $\frac{R_p}{\tan\phi}$ where: ϕ is the ejection angle of the sheet that depends on Q and R_p presents the distance of the prism in the sheet from the jet impact (Figure 4.3). The distance R_p is defined as: $\frac{D}{2} < R_p < R' \leq R$. Based on the Figure 2.7 in the Chapter 2, one estimates that R = 50 mm corresponding to Q values between 2.5 10^{-5} $m^3.s^{-1}$ and 4.5 10^{-5} $m^3.s^{-1}$. The ϕ value is estimated to be 80° for the same Q ranges. Therefore, the minimum value of A is equal to 8.8 mm for which the sheet will impact the bottom extremity of the triangular prism. For a security reason, the value of A was fixed to 20 mm and the prism was mounted from the disk surface downward as one can never obtain an horizontal sheet.

The droplet measurements vary as a function of the disk type. In the case of the non-textured disk, droplets were measured as soon as they were detached from the sheet (60 mm from the disk edge) in order to avoid merged droplets. In the case of the textured disks, droplets were measured as soon as they were detached from the jet.

One investigated different configurations of structures in order to control the turbulent Savart sheet. In the following, all structures are placed radially in the Savart sheet at R_p = 15 mm from the jet impact.

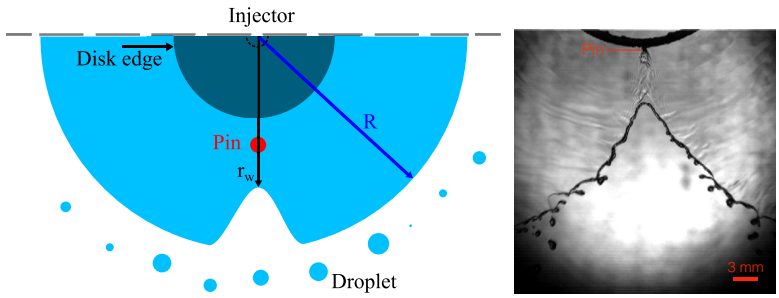

Figure 4.4: Perturbation of the Savart sheet using a cylinder pin: (a) The sketch illustrates the observed wake downstream the pin. (b) An image of the wake at $Q = 2.5\ 10^{-5}\ \mathrm{m}^3.\mathrm{s}^{-1}$.

4.2 Case of a cylinder pin

One created a local perturbation in the free Savart sheet using a cylinder pin with a diameter of 300 μm that is close to the sheet thickness (Figure 4.4). This obstacle was able to alter the sheet dynamics. The sheet is pierced downstream the pin and the sheet exhibited a V shaped wake. This observation is similar to that obtained in the case of polygonal sheets generated with textured disks ([4, 5]). The Figure 4.5 represents the evolution of the distance r_w for which the wake is observed as a function of the flow rate Q. The radius r_w distance was computed using 50 images separated by 0.5 ms in order to better tracking of the wake evolution. Error bars indicate the standard deviation calculated based on 50 measurement repetitions of r_w for the same Q. The curve trend is similar to that of the sheet radius and it can be divided in two parts. In the first part, the curve is characterized by an abrupt slope for low Q ($< 2\ 10^{-5}\ \mathrm{m}^3.\mathrm{s}^{-1}$). The r_w is almost stable for the same Q and it never reaches the sheet radius. When Q increases, the curve is characterized by an almost constant r_w values around 25 - 30 mm corroborated by high lengths of error bars. The high variability may be explained by the appearance of the holes (due to the turbulent sheet) downstream the pin and hence they affect the r_w measurement (Figure 4.6). For high Q, the wake may merge with the sheet rim and it never exceeds the sheet radius i.e. $r_w \leq R$.

An assembly of these cylinder pins lead to the modification of the standard Savart sheet as its rim adopted polygonal shapes. The vertices of these polygons constitute the emission

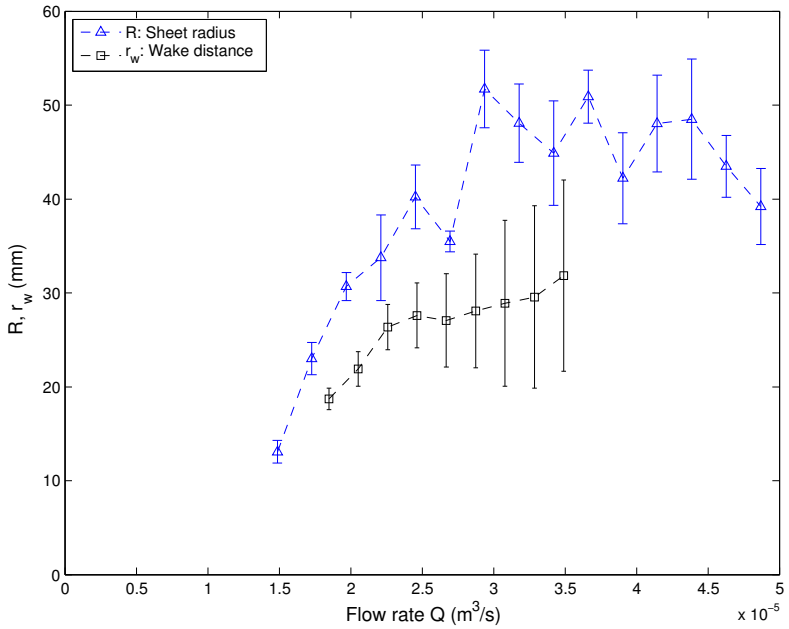

Figure 4.5: Evolution of the distance r_w of the wake observed downstream the cylinder pin as a function of the flow rate Q. The distances r_w and R are computed from the jet axis.

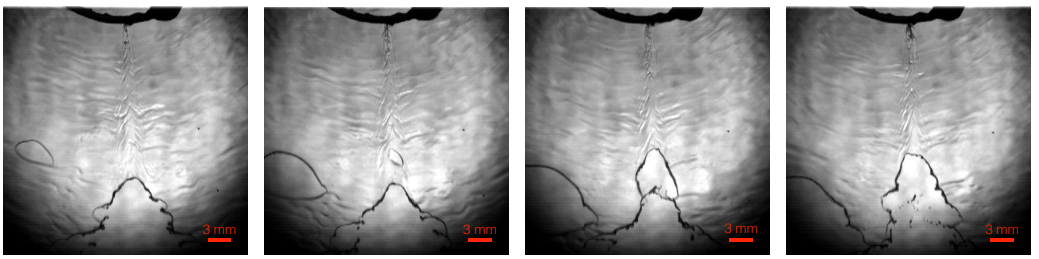

(a) (b) (c) (d)

Figure 4.6: Evolution of the wake downstream the pin for a $Q = 4.5\ 10^{-5}$ m^3.s^{-1}. The images (a), (b), (c) and were timely separated by 0.5 ms. The holes due to the turbulent flow increase the variability of the distance wake r_w.

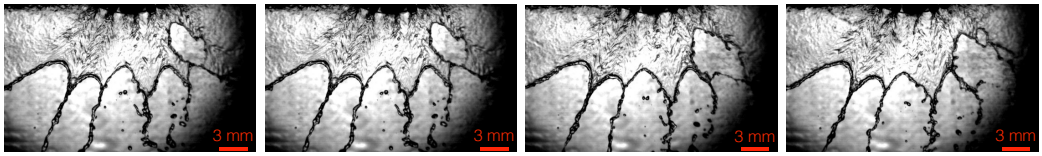

(a) (b) (c) (d)

Figure 4.7: An assembly of cylinder pins placed in the sheet influence the sheet dynamics as its rim exhibits a polygonal turbulent vertices. These vertices are the emission points of individual jets. However, the holes break up the sheet and destroy the initial organization of the obtained jets. The images (a), (b), (c) and were timely separated by 0.5 ms for $Q = 3.1\ 10^{-5}$ m^3.s^{-1}.

source of jets (Figure 4.7). However, the architecture of these polygons is unstable as additional perturbations presented by holes break up randomly the sheet. Compared to the studies of Dressaire ([4, 5]), their polygons are stable because of the laminar flow and the absence of holes in the sheet.

To sum up, the Savart sheet is perturbed using a cylinder pin and resulted in a wake that is unstable for high Q due to the holes. An assembly of these pins lead to control the sheet and the formation of individual jets. However, the jets are rapidly lost downstream the pins due to the random break up of the sheet caused by the holes. Therefore, one must use the right structure that avoid the wake downstream. In addition, it must be placed in the sheet at a radial distance inferior to R'. In the following, we will use a triangular prism to break up the sheet.

4.3 Case of a triangular prism

A triangular prism structure characterized by a_p = 1 mm and l_p = 2.5 mm was placed directly in the Savart sheet at R_p = 15 mm from the jet axis. Consequently, the triangular prism breaks up the sheet as a stable decrease in the radial sheet was observed. However, the sheet aperture adopts the triangle shape and no wake was observed downstream the prism (the space is empty of liquid) (Figure 4.8). At the aperture point of the sheet (that corresponds to a radial distance r = 12.5 mm where the sheet hits the prism), the flow is no longer radial and two tangential components of velocities are created on both sides of the prism. Also, the liquid is subjected to friction forces close to prism surface. The sheet

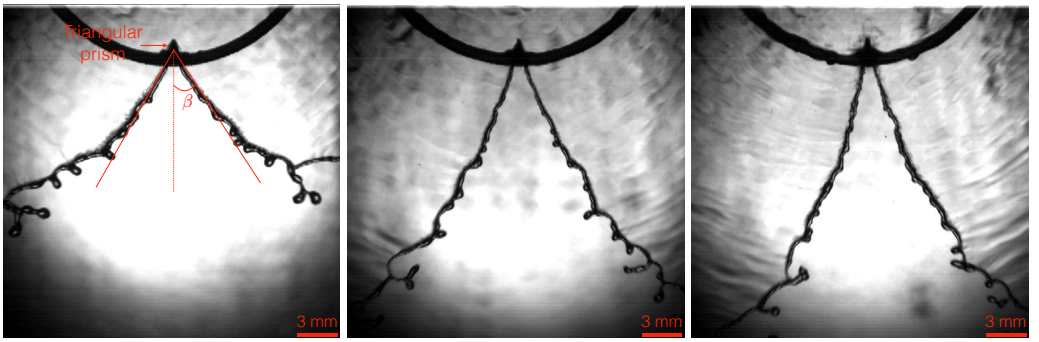

(a) (b) (c)

Figure 4.8: Perturbation of a Savart sheet using a triangular prism structure characterized by a = 1 mm and l = 2.5 mm and placed directly in the sheet at 15 mm from the jet axis: The sheet is perturbed and no wake was observed downstream the prism structure. The images (a), (b) and (c) correspond to the perturbation at different flow rates Q that are respectively 2 10^{-5} $m^3.s^{-1}$, 3.7 10^{-5} $m^3.s^{-1}$ and 4.8 10^{-5} $m^3.s^{-1}$

aperture is characterized by an angle β (Figure 4.8a). The Figure 4.9 presents the evolution of β as a function of Q. The value of β was computed based on one image for a given flow rate Q since the aperture shape was stable. At low Q, β presents high values. The sheet portion close to the prism structure is rapidly getting curved as the surface tension tends to reduce its volume (Figure 4.8a). By increasing Q, β is reduced and the sheet is more developed and getting much closer to the prism because of the inertia (Figure 4.8b).

When two successive triangular prisms (a = 1 mm) spaced by a gap b were radially inserted in the Savart sheet at 15 mm from the jet axis, one perturbed locally twice the sheet. As a result, two neighboring apertures are created, interact with each other and lead to the formation of a sheet portion. This latter is entrapped in the gap b and it evolves downstream the two neighboring prisms (Figure 4.10). For low b values, one generates a liquid bead (similar to a capillary jet) that disintegrates into droplets under the action of surface tension. The Figure 4.10a illustrates the generation of a jet through a gap b = 250 μm. It is clear that the liquid sheet entrapped in the small gap is highly subjected to the frictions induced by the surface of the prisms. Hence, the capillary forces dominate the inertia and generates a small liquid jet (bead). As b increases, the trapped liquid is less subjected to surface frictions and it generates a developed sheet thanks to the inertia. This sheet between two prisms looks like a V shape tongue. The V shaped sheet and its maximum expansion are designed respectively by *vss* and C (Figure 4.10b). Then, the *vss* results

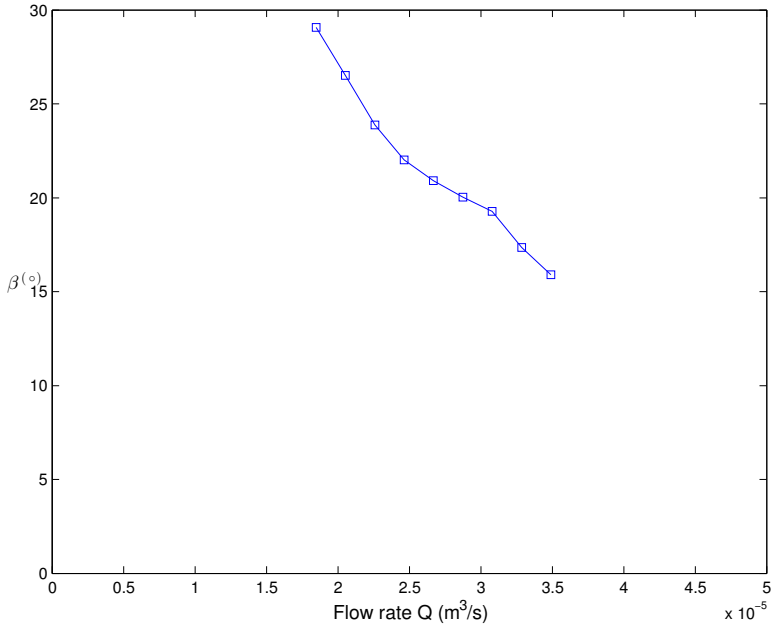

Figure 4.9: Evolution of the sheet aperture β as a function of the flow rate Q.

in a ligament bead characterized by a breakup length L_b and it ends into droplets (Figure 4.10b). The total breakup length is equal to the sum of C and L_b. For high b values, the trapped liquid pass easily through the gap, and hence leading to a well developed sheet dominated by inertia while the V shape is less pronounced and its rim is subjected to the surface tension (Figure 4.10c).

In the following, the formation of the sheet between two successive prisms will be explained using a geometrical model. Also, the focus will be on the transition between the *vss* and the jet ligament by investigating the intrinsic distances C and L_b.

One developed a geometrical model that allows to explain the formation of the *vss* through the gap between two successive triangular prisms. The model aims to establish the interactions between C that is intrinsic parameter to the *vss* and the geometrical parameters of the triangular prisms as presented in the Figure 4.11. Based on a trigonometric development, C is defined as follows:

$$C = R_p(\sin\alpha\tan(\frac{\pi}{2} - \beta + \alpha) - (1 - \cos\alpha)) \tag{4.1}$$

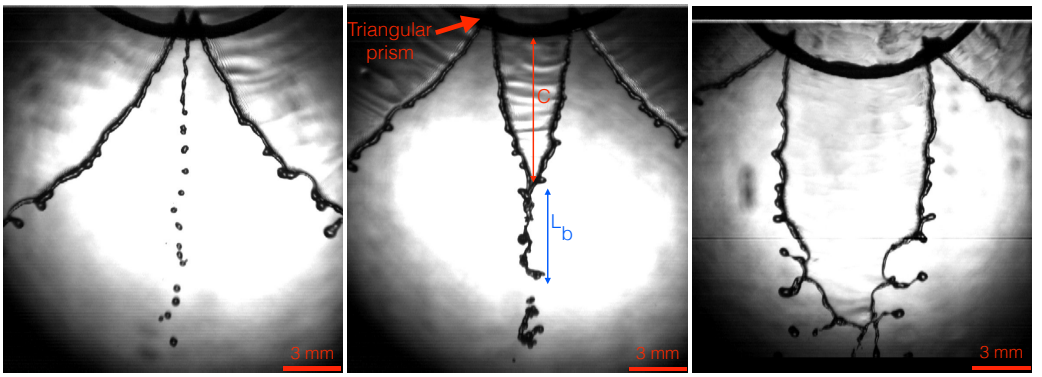

(a) (b) (c)

Figure 4.10: Perturbation of a Savart sheet by two successive triangular prisms spaced by a gap b: (a) For b = 250 μm, a jet is directly generated through the gap. (b) For b = 4.18 mm, a *vss* is generated from the gap and its radial expansion is designed by C. The sheet converges under the surface tension to form a jet ligament with a distance L_b that disintegrates into droplets. (c) For b = 7.32 mm, the obtained sheet is well developed and the V shape is less pronounced. Its rim breaks up into droplets. The trials are performed at the same $Q = 2.93\ 10^{-5}$ m^3.s^{-1}.

with: R_p correspond to the radial emplacement of the triangular prisms from the jet impact, α is the angle half between two successive prisms and β is the ejection angle of the *vss* formed close to one prism side.

The limits of the model are depending on the angle α and β:
- When α tends to zero, the C value is zero. It reflects either the case of the free sheet (without perturbations) or the sheet hits the textures because $b = 0$.
- When $\alpha << \beta$, the model results in a defined C value.
- When $\alpha \geq \beta$, C tends towards infinity but one is limited by the expansion sheet R. Hence, C tends towards R.

Moreover, the model overestimates the C since the *vss* is curved (under the effect of surface tension) just getting far away from the lateral sides of the prisms (the value of β is quickly modified). Also, the model is semi-empirical since the experimental measurements of β (that depends on Q) were used to compute C.

The Figure 4.12 presents the evolution of C as a function of Q for different gaps b. The continuous and dotted lines represent respectively the experimental and the semi-empirical

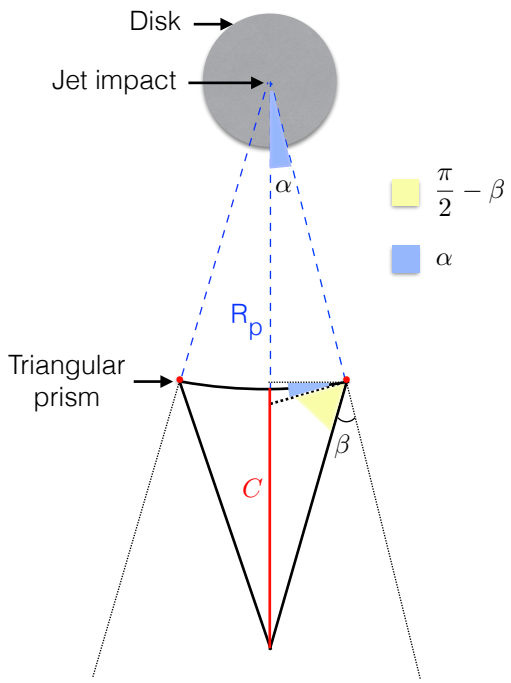

Figure 4.11: A sketch of the geometrical parameters defined in the case of two successive triangular prisms placed at a radial distance R_p from the jet impact. The triangular prism are considered as points in order to facilitate the calculation of C.

measurements (model) of C. For a given Q, each experimental measurement of C was performed based on Matlab analysis of 50 images acquired at 2000 Hz. For small b values corresponding to small α values ($\leq$ 2.08 mm), as expected, the sheet expansion C tends to zero. The variability of C is small even for high Q value and empirical measurements and the semi-empirical model are in a good fit. In the case of $b \leq 4.17$ mm, the sheet expansion slightly increases with the increase of Q where the semi-empirical model and experimental measurements are still in a good fit. By increasing b, the sheet is well developed downstream the neighboring structures. The latter fit is no longer valid since the semi-empirical model overestimates the values of C that tend to infinity in this case. For this reason, the curve corresponding to the case where $b = 14.65$ is not plotted. Also, for high Q, the holes appear near the sheet rim and disintegrate it what may reduce C. It is to note that the expansion C increases as b increases for a given Q.

To understand the transition between the *vss* and the jet that emerges from this latter and also the competition between the inertia and the capillary forces in this region, one

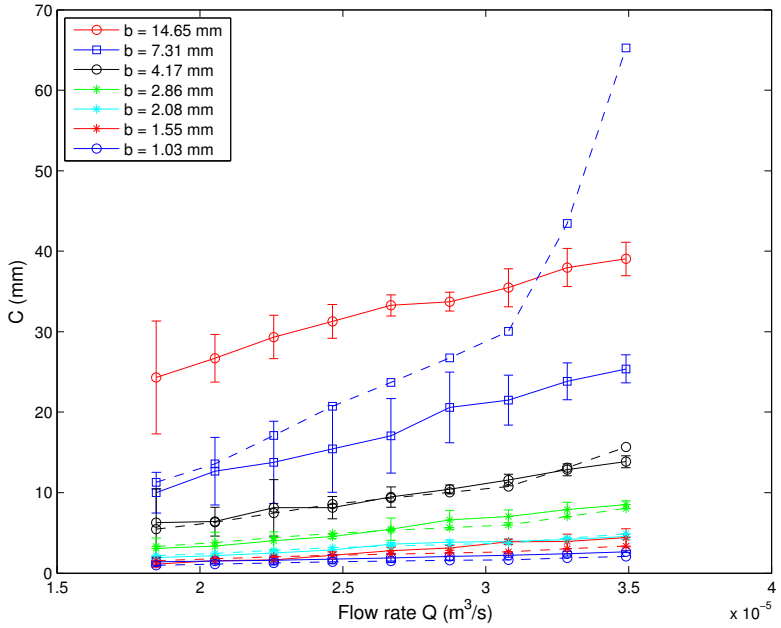

Figure 4.12: Evolution of the maximum sheet expansion C as a function of the flow rate Q for different gap b values between two successive triangular prisms. The continuous and dotted lines correspond respectively to the experimental and semi-empirical measurement of C.

compared in the following the distances C and L_b. The Figure 4.13 presents the evolution of C and L_b as a function of the geometrical angle 2α between two successive grooves for different flow rates Q. The distance L_b is also measured based on Matlab analysis of 50 images acquired at 2000 Hz for a given Q. The parameters C and L_b present two opposite trends with the increase of the angle 2α leading to establish three main parts. The first part corresponds to small 2α values; C is inferior to L_b. When 2α tends to zero, one rapidly promotes the generation of a jet ligament through the gap. Also, by increasing Q for these small angles, the L_b increases. Then, when 2α increases, the C increases linearly (i.e. the *vss* appears). Afterwards, the two curves C and L_b intersect and one defines the second zone that corresponds to 2α values between 11° and 16°. These angle values correspond respectively to distance gaps b around 2,87 mm and 4.18 mm that are close to the capillary length (3 mm for the tap water). Finally, the C values exceeds those of the L_b i.e. one promotes the generation of the *vss* that emits a small jet ligament. Here, the C increases with the increase of Q and no trend is found for the L_b in this region. From these observations, it is clear that the competition between the inertia and capillary forces plays

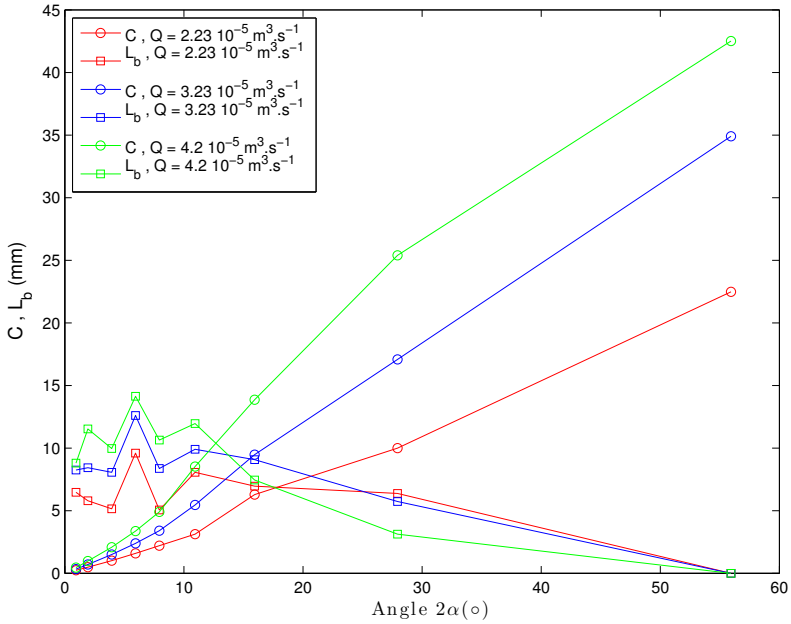

Figure 4.13: Evolution of C and L_b measured experimentally as a function of the angle 2α between two successive grooves. The continuous lines are used for a better readability of curves.

a crucial role in the transition between these zones. When b is inferior to the capillary length (first zone), the capillarity dominates the flow as a jet ligament is generated through the gap. When b is superior to the capillary length (third zone), the inertia exceeds the capillary forces and a well developed *vss* is created.

4.4 Case of N triangular prisms

One used N triangular prisms characterized by a_p = 1 mm and l_p = 2.5 mm to perturb the free Savart sheet. They were placed at 15 mm from the jet impact. As a result, the N triangular prisms interact together, modify locally the radial sheet dynamics and lead to several liquid jets downstream. Varying b and Q, two regimes of jets are observed and they are classified by the number of emitted jets n as shown in the Figure 4.14. The number of jets n is either stable or fluctuating.

In the case of a stable n, the sheet volume is equally divided by the N prisms. The volume portions entrapped in the gaps lead to a one jet per gap. Therefore, the number of jets n is equal to N. For a given flow rate Q, one generates a small jet column for small values of b. When b increases, a *vss* is ejected through gaps. By increasing the flow rate Q, the regime $n = N$ is no longer valid and one founds the case of a fluctuating n. The *vss* are always emitted through the gaps but some neighboring *vss* may locally interact and merge constituting a local mixed zone. The number of jets n is fluctuating since the jet coalescence were elastic. Therefore, the jet number n is lower than N and greater or equal to $\frac{N}{2}$. At this given Q, one also finds elastic merging of jets when b decreases. At high flow rates, the merging between jets is no longer elastic. It becomes inelastic what leads to the creation of a Savart sheet downstream the prisms. This latter contains cardioids on its surface that are similar to that of Taylor.

In order to understand the transition between the observed regimes, we have established phase diagrams by varying Q, b and a_p. The Figure 4.15 presents the different jet regimes that are plotted as a function of b and Q. Each b corresponds to a disk configuration where a_p is fixed to 1 mm for all the tested designs. The smallest gap b that can be printed is 0.25 mm leading to 72 prisms. Below a critical value b (= 0.5 mm), the entrapped liquid between the gaps is no longer radial and become tangential to the prism sides. These tangential contributions lead to a jet ligament and the jet number n is equal to N. By increasing Q, the neighboring jet ligaments may merge elastically what may affect their stabilities. The jet number n is mainly lower than N and greater or equal to $\frac{N}{2}$. When b increases, the tangential contributions lead to the convergence of the entrapped sheet into a *vss* that lead to a liquid bead disintegrating into droplets. The jet number n is stable and it is equal to N. By increasing Q, the elastic coalescence between successive *vss* and hence the jet number n is mainly lower than N and greater or equal to $\frac{N}{2}$.

The zone of $n = N$ where a jet ligament jet is generated through the gap, the *vss* still exist but its C value is too small compared to the L_b. The transition between the two kinds of jets is linked to the capillary length that defines the competition between the inertia and the capillarity as shown in the Figure 4.13. Therefore, below the capillary length (b = 3 mm), the capillary forces dominates the inertia while the two kinds of jets still coexist (a small *vss* converging to a jet ligament). When b is too small ($\leq$ 0.5 mm), the C value is neglected compared to L_b and only the jet ligament is indicated. When b exceeds the capillary length,

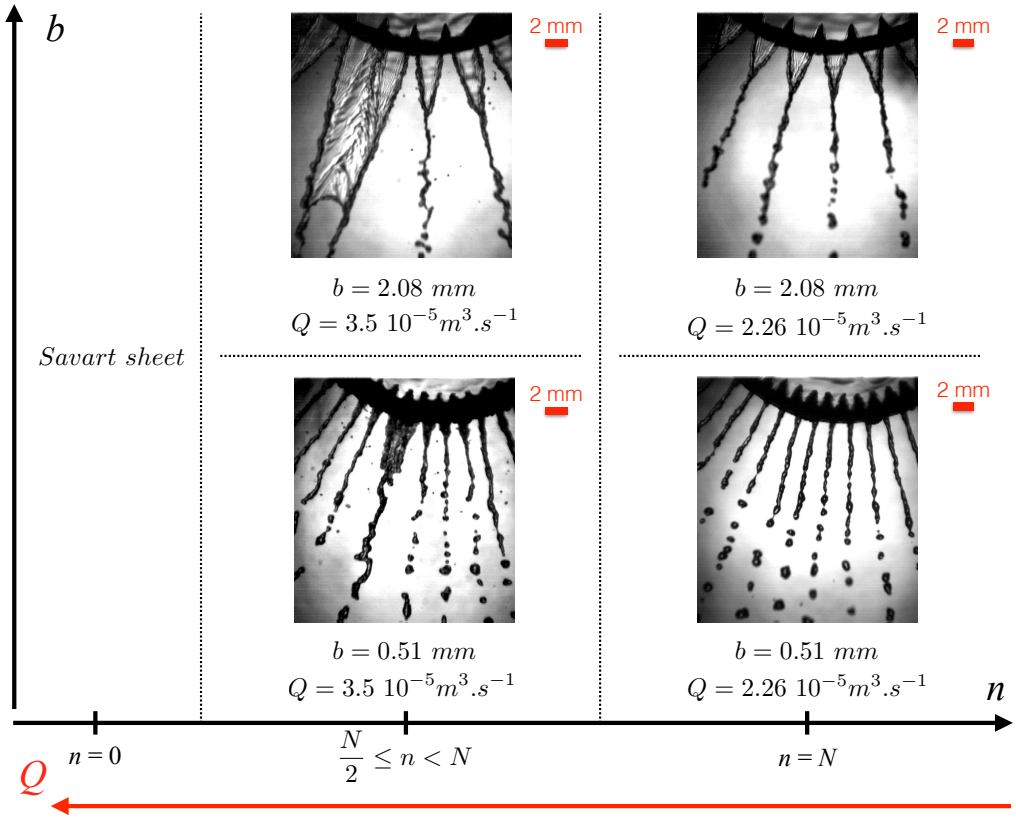

Figure 4.14: Number of jets n generated through the gaps between prisms depending on b and Q. The number of jet n can be either stable and it is equal to N or unstable and $n \leq N$.

the two kinds of jets coexist (a developed *vss* converging to a small jet ligament) where the inertia dominates the capillary forces. By increasing b, the *vss* is still developing by increasing its C while the L_b is reduced as shown in the Figure 4.13.

The second configuration corresponds to triangular prisms for which we varied a_p values for a fixed b equal to 0.25 mm. The prism numbers corresponding to a_p values are presented in the Table 4.1. The Figure 4.16 presents the jet regimes plotted as a function of a_p and Q. For small a_p values, the generated jets are getting closer and exhibit an elastic coalescence for the tested Q ranges. Hence, the jet number n is unstable and it is lower than N and greater or equal to $\frac{N}{2}$. By increasing a_p, the regime $n = N$ is found but the coalescence appears rapidly by increasing Q. As a_p increases, the jet regime $n = N$ expands and the merging zone occurs at Q ranges close of those obtained in the first configuration.

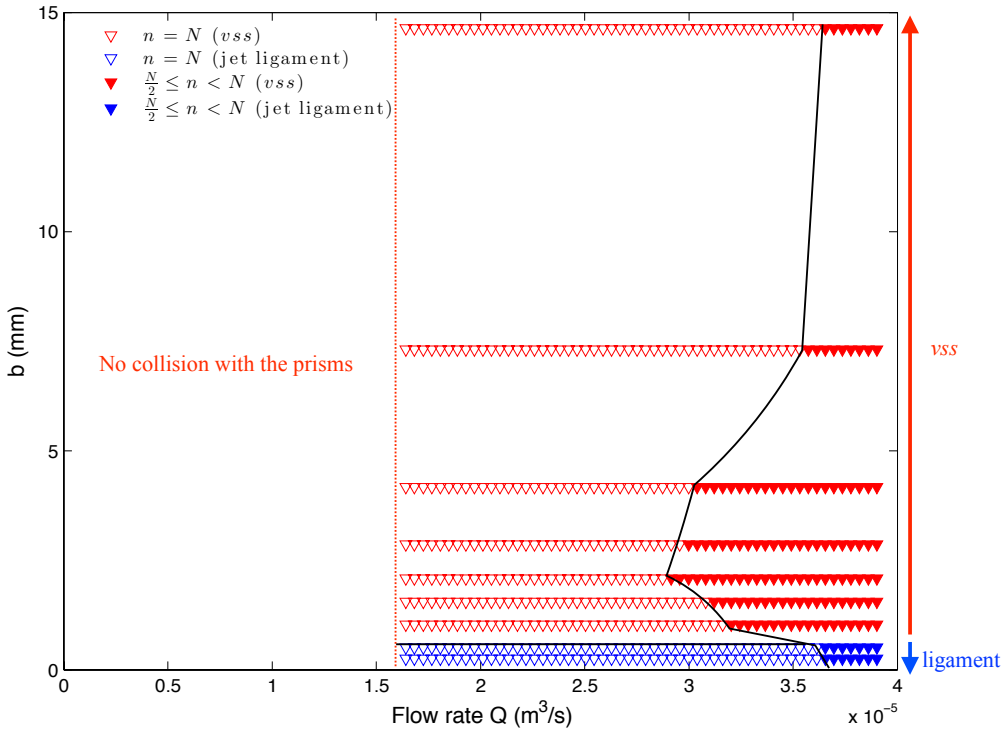

Figure 4.15: Representation of different regimes as a function of b (mm) and Q (m^3.s^{-1}). The base a_p is fixed to 1 mm.

The origin of the elastic coalescence comes from the corrugations presented at the surface of the generated jets in particular at high Q. These corrugations constitute the elastic connections areas between two very close jets and hence it reduces the number of jets n. Also, when the entrapped liquid is subjected to deceleration in the gap, the sides of the triangular prism are quickly wet and hence they constitute a connection source with the neighboring jet [53].

To sum up, the entrapped sheet volume portion in the gap changes its radial expansion and adopts a tangential behavior that converges to a jet. This latter can be a *vss* or a ligament jet and the transition between the two kinds of jets is directly linked to the competition between inertia and capillarity. According to the first configuration (a_p = 1 mm and variable b values), the jet number can either stable ($n = N$) or unstable ($\frac{N}{2} \leq n < N$). The reduce of a_p allows to increase the jet numbers n but it lead to an expansion of the merged zones. For the agronomic application, the value of the gap b between successive

prisms should be inferior to the capillary length l_c (3 mm in the case of water) in order to ensure the formation of jets where the capillarity dominates. Also, the base a_p should be large as much as possible to resist to the flow impact and to avoid the merging of jets. However, a_p should be small enough to ensure the formation of a maximum number of jets. According to the phase diagram, a_p = 1 mm and b = 0.25 mm are the best compromise to generate liquid jets. The jet number n will depend on the distance R_p of prisms from the jet impact.

Table 4.1: Characteristics of prism designs based a variable a_p. The b is fixed to 1 mm and the prisms are placed at 15 mm from the jet impact

a_p (mm)	Prism numbers N
0.28	180
0.34	160
0.75	94
0.85	86
0.99	76
1.06	72

The generated jets (case of the textutred disks) or sheets (case of the non-textured disk) breakup then into droplets. The droplet characteristics in terms of diameters and velocities are addressed in the following section.

4.5 Droplet diameters

The resulted distribution size of droplets emitted from two and N triangular prisms are characterized by their numbers and volumes in this section.

4.5.1 Case of two successive triangular prisms

The jets emanating from the perturbation of the sheet by two successive triangular prisms (a_p = 1.06 mm) spaced by a gap b produce droplets. The droplet diameters are firstly investigated in terms of numbers. The Figure 4.17 presents the probability density function

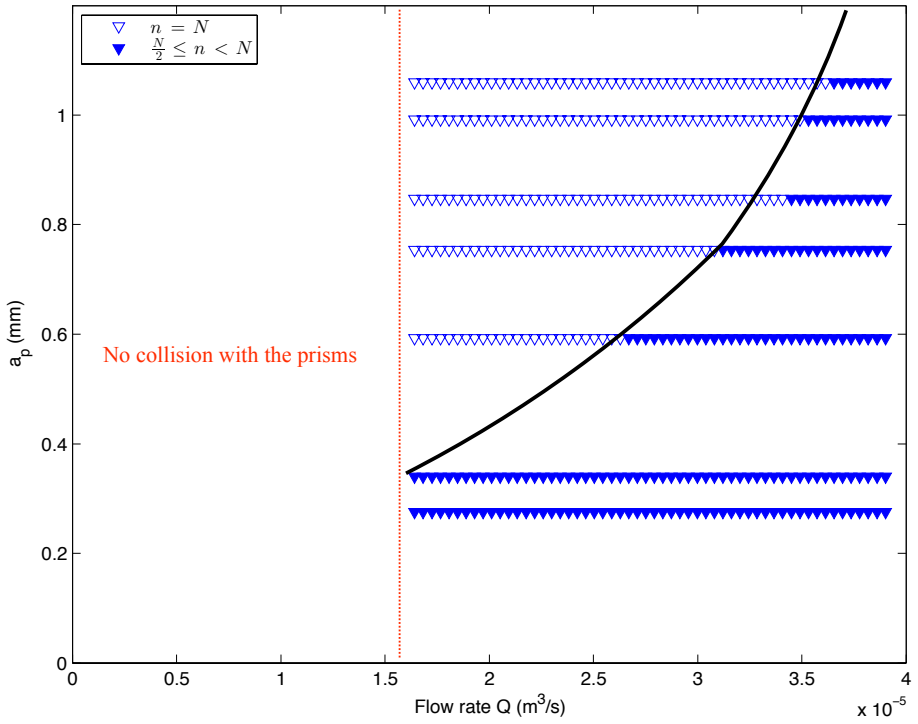

Figure 4.16: Representation of different regimes as a function of a_p (mm) and Q ($m^3.s^{-1}$). The base b is fixed to 0.25 mm.

(PDF) of droplets where the percentage of droplets are plotted as a function of their diameters. All the configurations are compared to the reference measurement where droplets are ejected from the Savart sheet in the case of a non-textured disk. Characteristics of droplets corresponding to different measurement points are shown in Table 4.2.

In the case of the non-textured disk, the droplet size distribution has a probability peak corresponding to droplet diameters of 250 μm and and their percentage is 40 %. The D_m is 331 μm. The droplet size distribution seems to be tightened and it is highlighted by reduced STD and CV values that are respectively 123 μm and 37 %. Droplets with diameters exceeding 700 μm have low percentages of probabilities that are inferior to 3 %. This result is contradiction with the measurements by Clanet and Villermaux [9]. The production of small droplets may be linked to the reduced disk diameter D = 6 mm that permits to minimize the surface friction on the disk and hence generating a thin film. Once the two successive triangular prisms are inserted in the sheet, the sheet break up

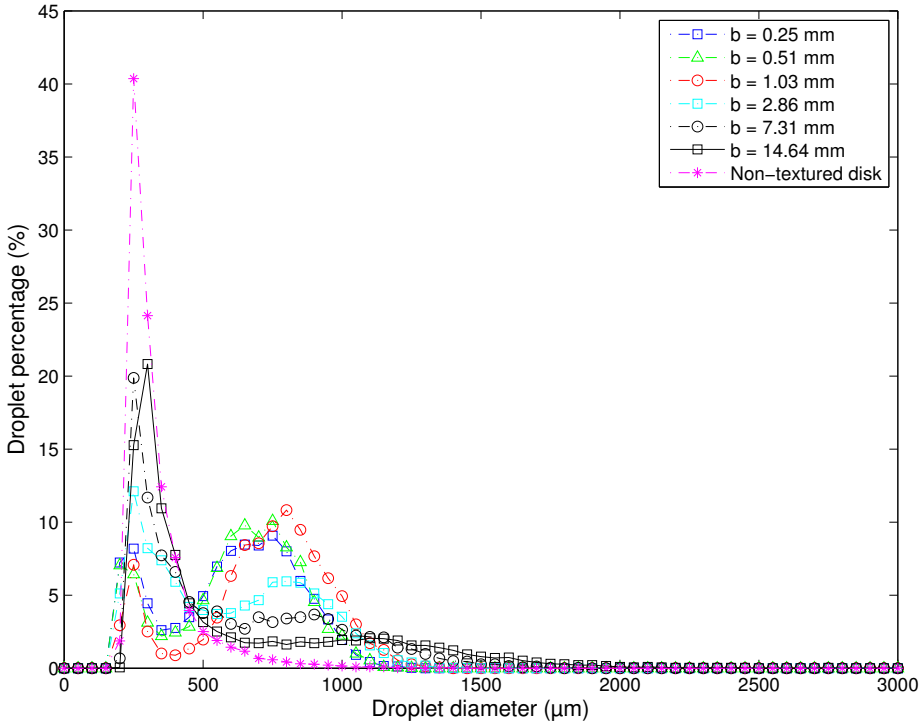

Figure 4.17: Representation of droplet percentages as a function of their diameters in the case of two neighboring triangular prisms spaced by a gap b. The base of the prism a_p is 1.06 mm. The prisms are placed at R_p = 15 mm from the jet impact. The curve *non − textured disk* corresponds to droplets emitted from the Savart sheet. All the measurements were performed at a $Q = 2.8\ 10^{-5}\ \mathrm{m^3.s^{-1}}$)

regime is no longer valid and the jet break up regime occurs. The droplet size distribution seems to be extended compared to that of the non-textured disk as it adopts a bimodal shape characterized by two probability peaks. The first peak which is the largest corresponds to main droplets and the lowest probability peak corresponds to the secondary droplets. The bimodal aspect is linked to the jet breakup behavior that is influenced by the capture of the radial flow in the prism and the change of the flow expansion from radial to tangential. A liquid bead is formed (instead of a capillary jet) and disintegrates in the Plateau-Rayleigh regime (see Figure 1.5) but secondary droplets are generated in addition to main droplets (similar to the case of grooves). For all measurements involving the two neighboring prisms, the D_m increase and the peak of secondary droplets is close to the main peak of the droplet population generated by the free Savart sheet but with smaller percentages. Droplet diameters exceeding 1600 μm have very low percentages.

For the configurations including b values inferior or equal to 1.03 mm, the D_m is increased as b increases and the main and secondary droplets have almost close percentages. By increasing b, the *vss* is well developed and the D_m is mainly decreased and it still superior to that of the case of the free Savart sheet. The droplet size distribution is extended compared to the previous case of b and it is highlighted by high STD and CV values. Also, the main droplets are less produced what necessarily increase the percentage peak of secondary droplets.

Table 4.2: Characteristics of droplets corresponding to two neighboring triangular prisms spaced by a gap b. The prisms are placed at R_p = 15 mm from the jet impact. The curve $non-textured\ disk$ corresponds to droplets emitted from the Savart sheet. All the measurements were performed at a $Q = 2.8\ 10^{-5}\ m^3.s^{-1}$.

	D_m (μm)	STD (μm)	CV (%)
$Non-textured\ disk$	331.24	123	37
b = 0.25 mm	602.4	233.41	38
b = 0.51 mm	621.46	225.2	36
b = 1.03 mm	717.83	238.68	33
b = 2.86 mm	588.27	280.24	47
b = 7.31 mm	582.89	331.26	56
b = 14.64 mm	600.52	412.95	68

In the following text, the produced droplets are characterized in terms of their volumes. The Figure 4.18 presents cumulative relative volumes of droplets as a function of their diameters. In order to ensure a better readability of curves in Figure 3.11, the spray intrinsic parameters V_{10}, V_{50}, V_{90} and the relative span factor RSF are presented in Table 4.3.

The spray produced in case of the non-textured disk is extremely coarse (XC) where the V_{50} is 498 μm. The droplet size distribution is wide and is highlighted by a high RSF (= 1.38). The spray is also characterized by 10% of its volume by droplet diameters inferior to 269 μm. By introducing the two neighboring prisms, the droplet size distribution is shifted towards big droplets as the V_{50} increases with the increase of b. The produced sprays are characterized by V_{10} that exceeds 590 μm. This is directly linked to the change in the breakup regime from the sheet to the jet breakup. The droplet size distribution are tightened and they are corroborated by reduced RSF values.

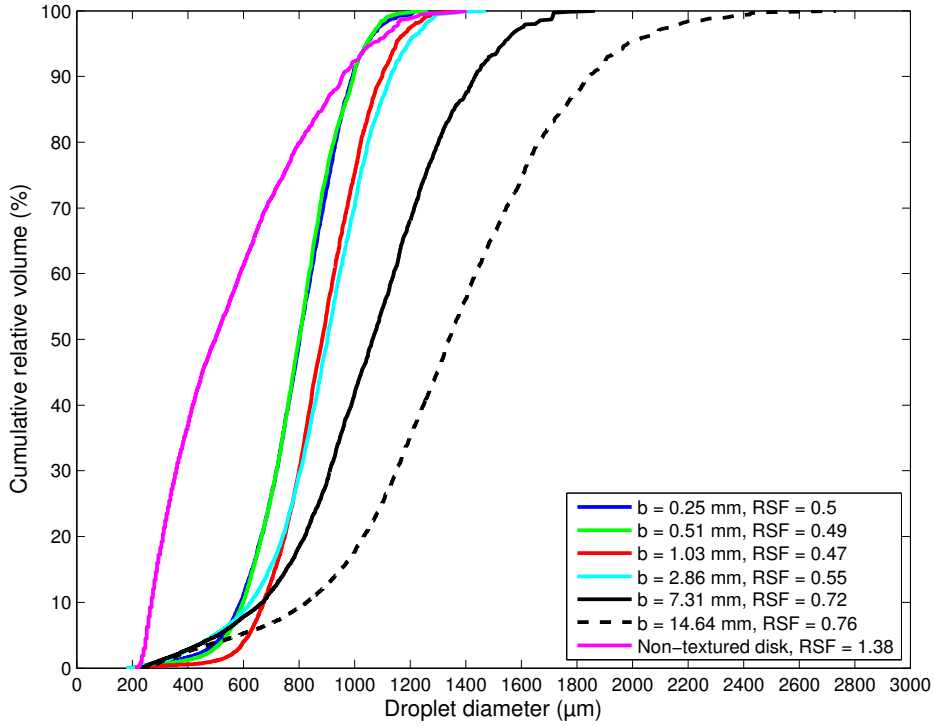

Figure 4.18: Representation of cumulative relative volumes of droplets as a function of their diameters. Measurements correspond to droplets emitted by the Savart sheet in the case of the non-textured disk and by different types of jets in the case of different configurations of the two neighboring triangular prisms spaced by a gap b. The measurements were performed for a $Q = 2.8\ 10^{-5}\ \mathrm{m^3.s^{-1}}$).

In the case where the gaps b are too small (0.25 mm and 0.51 mm), the sprays present similar characteristics in terms of V_{50} and RSF (around 0.5). For b values between 1.03 mm and 2.86 mm, the *vss* is developed (that means that more liquid volume is passing through the gap) and the V_{50} increases. The droplet size distributions are tightened and are illustrated by reduced RSF values (0.48 μm - 0.55 μm). By increasing values of b, the *vss* grows more and gets closer to the sheet shape. As a result, the droplet size distribution is extended and presents slightly high RSF values. Also, the V_{50} increases and reaches 1340 μm in the case of b = 14.64 mm. However, compared to the Savart sheet, the difference in terms of V_{50} is big and it is probably linked to the repartition of the sheet volume in the case of the two prisms.

To sum up, it is too difficult to establish a benchmark in terms of volume between the two

configurations (textured disk with two successive prisms) and non-textured disk. Indeed, one founds the sheet and jet breakup regimes that affects the droplet diameter. Even, the *vss* is developed through the gap, it ends by splitting into to a small/big jet ligament that disintegrates into droplets. In addition, the sheet volume is not equally divided between the gap and the rest of the free sheet.

Table 4.3: Spray characteristics in terms of volumes corresponding to the non-textured disk and the case of two neighboring triangular prisms spaced by a gap b. The base a_p of the prism is 1.06 mm. The measurements were performed for a $Q = 2.8\ 10^{-5}\ m^3.s^{-1}$.

	Q (10^{-5} $m^3.s^{-1}$)	V_{10} (μm)	V_{50} (μm)	V_{90} (μm)	*RSF*
Ungraved disk	2.8	269.38	498.29	959.14	1.38
$b = 0.25$ mm	2.8	590.70	801.81	992.80	0.5
$b = 0.51$ mm	2.8	599.34	801.08	996.29	0.49
$b = 1.03$ mm	2.8	673.72	884.46	1097.5	0.48
$b = 2.86$ mm	2.8	626.23	903.14	1130.8	0.55
$b = 7.31$ mm	2.8	667.77	1065.9	1435.4	0.72
$b = 14.64$ mm	2.8	827.97	1340.1	1847.8	0.76

In the following, the droplets produced by the jets obtained in the case of N triangular prisms are characterized.

4.5.2 Case of N triangular prisms (R_p = 15 mm)

One investigates the effect of N triangular prisms placed at R_p = 15 mm in the Savart sheet on the droplet diameters. As the agronomic application requires a large number of jets n, three designs presented in the Table 4.4 permit to generate both a maximum and a stable n ($n = N$).

One firstly investigates droplet diameters in terms of numbers. The Figure 4.19 presents the PDF of droplets where the droplet percentages are plotted as a function of their diameters. The three tested designs TD_1, TD_2 and TD_3 are compared to the case of a non-textured disk. The droplet measurements were performed at $Q = 2.8\ 10^{-5}\ m^3.s^{-1}$). Characteristics of droplets corresponding to different measurements are shown in Table 4.2.

As explained before, the case of the non-textured disk presents a probability peak corresponding to droplet diameters of 250 μm with 40% and the D_m is 331 μm. By the introduction of N triangular prisms, one creates a second droplet population that is probably due to the difference of the breakup regime of the liquid. In the case of TD_1, the two droplet diameter populations have the same percentages (7%) and the peak of secondary droplets corresponds to the same droplet diameters as in the case of the non-textured disk. The D_m is increased and the droplet size distribution is extended. By increasing the jet number n (reducing a_p), the pdf is shifted towards smaller droplets and the D_m is reduced.

Table 4.4: Characteristics of the tested textured disks (including N prisms).

Textured disk	b (mm)	a (mm)	number of prisms N
TD_1	0.25	1.06	72
TD_2	0.25	0.85	86
TD_3	0.25	0.75	94

Table 4.5: Characteristics of droplets corresponding to three tested designs TD_1, TD_2 and TD_3. The prisms are placed at R_p = 15 mm from the jet impact. The $non-textured\ disk$ corresponds to the reference case. All the measurements were performed at a $Q = 2.8\ 10^{-5}$ m^3.s^{-1}.

	D_m (μm)	STD (μm)	CV (%)
$Non-textured\ disk$	331.24	123	37
TD_1	602.31	233.41	38
TD_2	460.52	210.16	45
TD_3	423.86	186.46	44

Then, one investigates the droplet diameters in terms of their volumes. The Figure 4.20 presents cumulative relative volumes of the produced droplets as a function of their diameters. The obtained spays are extremely coarse (XC). All configurations are thus compared to a standard agricultural flat fan nozzle that is $Teejet\ TP$ 65 15 with the same spray class (XC) tested at $Q = 6.9\ 10^{-5}$ m^3.s^{-1}. The intrinsic parameters of sprays that are V_{10}, V_{50}, V_{90} and the relative span factor RSF are presented in Table 4.6.

In the case of the non-textured disk, the V_{50} is centered around 498 μm and the droplet size distribution is large. It is corroborated by a high RSF value (= 1.38) that is close to that of common hydraulic nozzles ($\approx$ 1) and in particular to that of the $Teejet\ TP$6515.

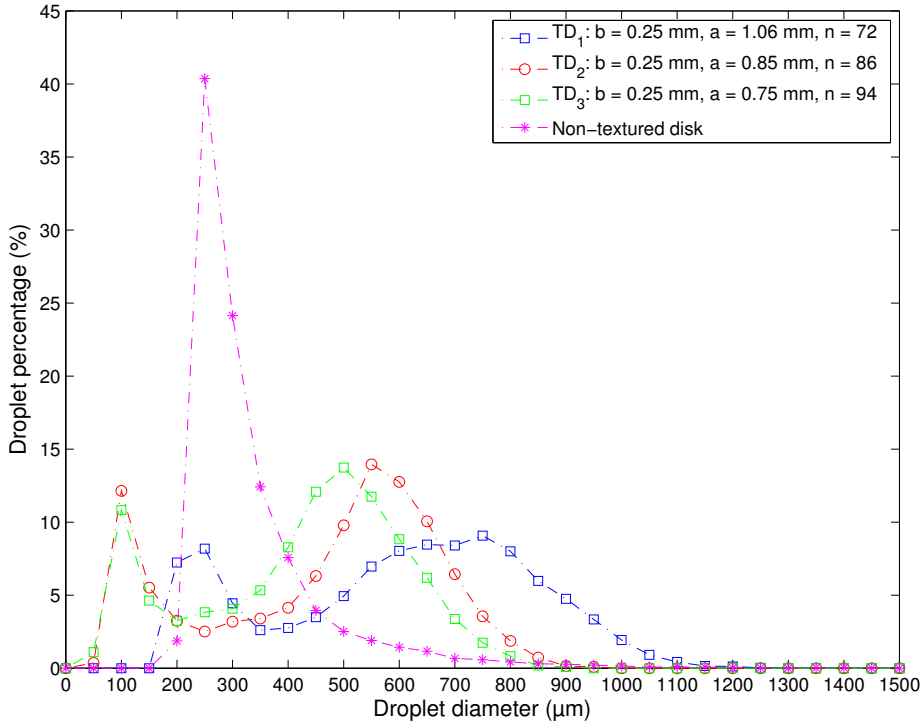

Figure 4.19: Representation of droplet percentages as a function of their diameters in the case of three designs TD_1, TD_2 and TD_3. The prisms are placed at R_p = 15 mm from the jet impact. The curve *non − textured disk* corresponds to droplets emitted from the Savart sheet. All the measurements were performed at a $Q = 2.8\ 10^{-5}$ m^3.s^{-1}.

By the insertion of 72 triangular prisms in the case of TD_1, the V_{50} is increased to 801 μm and the droplet size distribution becomes reduced where the RSF is equal to 0.5 that is similar to that of the CDA technology. By increasing the n (for the same R_p) to 86 and 94 jets, the sheet volume is equally divided in more smaller volumes in the gaps. As a result, the droplet size distribution is shifted towards small droplets and the V_{50} is reduced as n increase. The droplet size distribution is kept tightened corroborated by low RSF (around 0.5). The smallest V_{50} that can be reached is 577 μm in the case of the TD_3. If one increases more the n, one expects to reduce more the V_{50}. However, based on the phase diagram (Figure 4.1), the jet regime $n = N$ is no longer valid and the jet coalescence dominates and n becomes unstable what may increase the droplet diameters.

The Figure 4.21 highlights the trend of the V_{50} as a function of the base a_p of the prism. The values of V_{50} are extracted from the Table 4.6. The distance R_p of the prism from

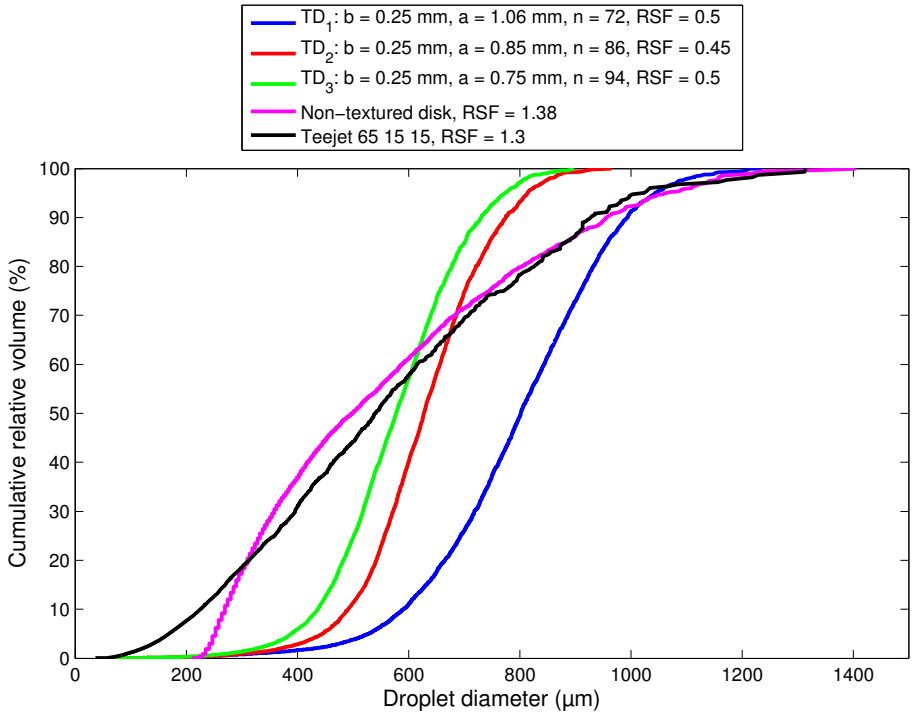

Figure 4.20: Representation of cumulative relative volumes of droplets as a function of their diameters. Droplet measurements correspond to the non-textured disk and to textured designs TD_1, TD_2 and TD_3. The prisms are placed at $R_p = 15mm$. The measurements were performed at a $Q = 2.8\ 10^{-5}$ m^3.s^{-1}. All configurations are compared to a reference standard agricultural flat fan nozzle *Tee jet TP* 65 15 within the same spray class (extremely coarse (XC))

the jet impact is 15 mm and the gap b is 0.25 mm. As the distance a_p increases, the V_{50} decreases and the number of jets n also decreases.

One can increase the number of jets n by inserting the prisms further down in the sheet as long as being careful to the holes. In the following, the effect of the distance R_p of prisms on the droplet size distribution is addressed.

4.5.3 Case of N triangular prisms (R_p = variable)

By taking into account to the limitation of the radial distance R' (for which the holes appear in the sheet), the N triangular prisms are inserted as far as possible downstream in the sheet. The different distances R_p are 15 mm, 22 mm and 28 mm. At 28 mm, the prisms

Table 4.6: Spray characteristics in terms of volumes corresponding to the non-textured disk and to textured designs TD_1, TD_2 and TD_3. The prisms are placed at $R_p = 15mm$. The measurements were performed at a Q = 2.8 10^{-5} $m^3.s^{-1}$. All configurations are compared to a reference standard agricultural flat fan nozzle *Tee jet TP* 65 15 within the same spray class (extremely coarse (XC)).

	Q (10^{-5} $m^3.s^{-1}$)	V_{10} (μm)	V_{50} (μm)	V_{90} (μm)	*RSF*
$Non-textured\ disk$	2.8	269.38	498.29	959.14	1.38
TD_1	2.8	590.7	801.12	992.80	0.5
TD_2	2.8	491.6	627.67	776.03	0.45
TD_3	2.8	436.91	577.89	730.87	0.5
Tee jet TP 65 15	6.9	225	540	928	1.30

are too close to the hole zone. The three design characteristics are presented in the Table 4.7. These designs allow to generate a stable configuration of jets that is $n = N$.

Table 4.7: Characteristics of the tested textured disks for different distances R_p.

Textured disk	R_p (mm)	b (mm)	a (mm)	Prism number N
TD_1	15	0.25	1.06	72
TD_4	22	0.25	1.06	120
TD_5	28	0.25	1.06	140

The Figure 4.22 shows the PDF of droplets where the droplet percentages are presented as a function of their diameters. The three tested designs TD_1, TD_4 and TD_5 are compared to the case of a non-textured disk. The droplet measurements were always performed at Q = 2.8 10^{-5} $m^3.s^{-1}$. Characteristics of droplets corresponding to different measurements are shown in the Table 4.8.

As one used the same Q in the previous section, one remains the same description to the transition from the case of the non-textured to the TD_1. At R_p = 15 mm, the D_m is 602 μm and n is 72 jets. By increasing the R_p to 22 mm, the n increases to 120 jets. As a result, the droplet size distribution is shifted towards small droplets and the D_m is reduced. The two droplet population have the same percentages (9%). By introducing the TD_5, the n reaches 140 jets and the D_m is decreased to 337 μm that is close to that of the reference case. The percentage of the secondary droplets exceeds those of the main droplets and reaches 15%.

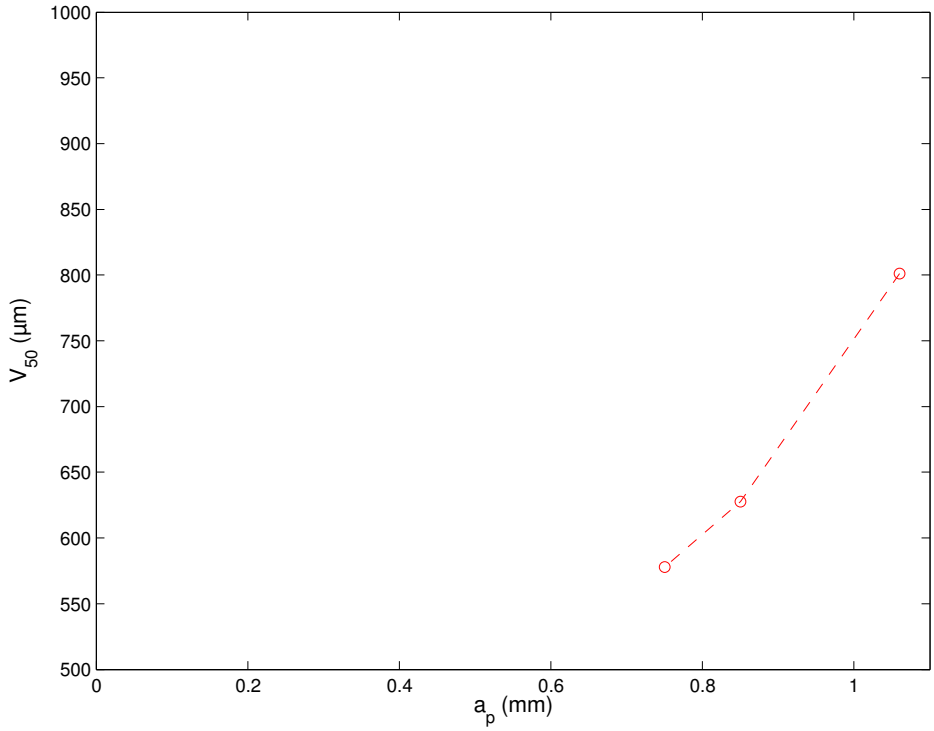

Figure 4.21: Evolution of the V_{50} as a function of the base a_p of the prism. The gap b is fixed to 0.25 mm and the distance R_p = 15 mm.

Table 4.8: Characteristics of droplets corresponding to three tested designs TD_1, TD_4 and TD_5 corresponding to three R_p values that are respectively 15 mm, 22 mm and 28 mm. The $non-textured\ disk$ corresponds to the reference case. All the measurements were performed at a $Q = 2.8\ 10^{-5}$ m^3.s^{-1}.

	D_m (μm)	STD (μm)	CV (%)
$Non-textured\ disk$	331.24	123	37
TD_1	602.31	233.41	38
TD_4	447.59	187.42	41
TD_5	337.53	183.44	54

.

Finally, the Figure 4.23 presents the cumulative relative volumes of the droplets as a function of their diameters. The tested configurations produce XC sprays and they are compared to the flat fan nozzle $Teejet\ TP$ 65 15 with the same spray class tested at $Q = 6.9\ 10^{-5}$ m^3.s^{-1}. The intrinsic volumetric parameters of the produced sprays are presented in the Table 4.9.

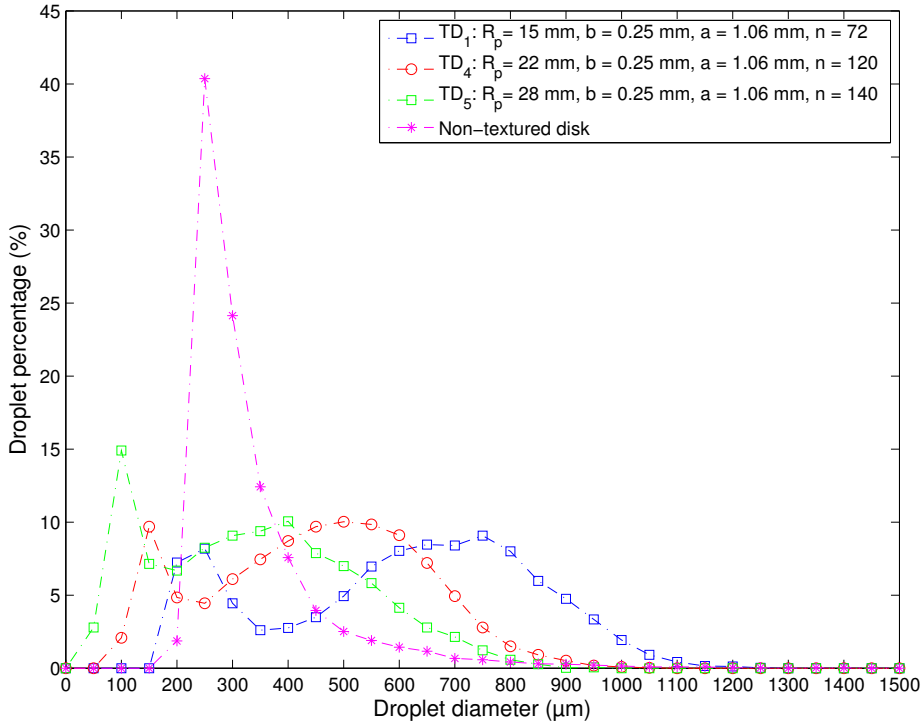

Figure 4.22: Representation of droplet percentages as a function of their diameters in the case of three designs TD_1, TD_4 and TD_5. The prisms are placed at different R_p that are 15 mm, 22 mm and 22 mm. The reference case corresponds to the $non-textured\ disk$. All the measurements were performed at a $Q = 2.8\ 10^{-5}$ m^3.s^{-1}.

As a reminder, the non-textured disk is characterized by an extended droplet size distribution ($RSF > 1$) and a V_{50} around 498 μm. These volumetric parameters are similar to those of the Standard Teejet. The insertion of the prisms lead to reduce the width of the droplet size distribution. When the TD_1 is used at R_p = 15 mm (n = 72 jets), the V_{50} is increased to 801 μm and the RSF is reduced to 0.5 (compared to the Savart sheet). By increasing the R_p to 22 mm, the n is increased to 120 jets. The V_{50} is reduced to 622 μm. This can be explained by the fact that the sheet becomes thinner at 22 mm and this latter is equally divided through 120 gaps what may reduce the spray volume per gap compared to the sheet volume at 15 mm. For the case TD_5, the n is increased to 140 as the R_p is increased to 28 mm. As expected, the V_{50} is reduced and reached 558 μm. The droplet size distribution is kept reduced and the RSF is around 0.5.

The Figure 4.24 highlights the evolution of the V_{50} as a function of the distance R_p. The

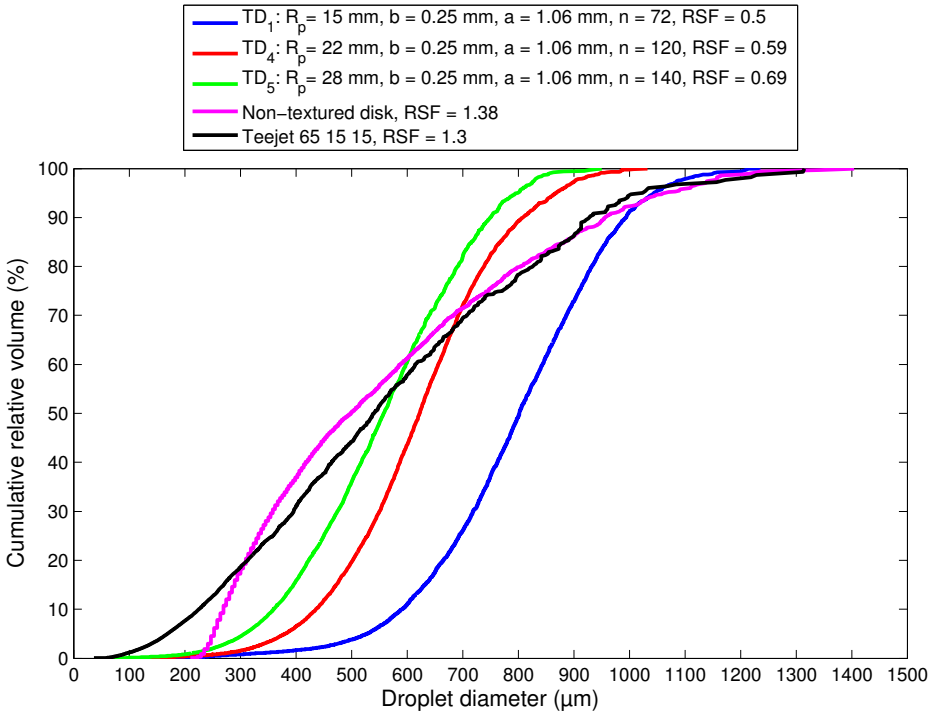

Figure 4.23: Representation of cumulative relative volumes of droplets as a function of their diameters. Droplet measurements correspond to the non-textured disk and to textured designs TD_1, TD_4 and TD_5. The prisms are placed at three R_p that are respectively 15 mm, 22 mm and 28 mm. The droplet measurements were performed at a Q = 2.8 10^{-5} $m^3.s^{-1}$. All configurations are compared to a reference standard agricultural flat fan nozzle *Teejet TP* 65 15 within the same spray class (extremely coarse (XC)).

values of V_{50} are extracted from the Table 4.9. The base of the prism a_p and the gap b are respectively 1.06 mm and 0.25 mm. As the distance R_p increases, the V_{50} decreases and the number of jets n increases.

To sum up, one investigates the influence of three parameters that are the base of the prism a_p, the gap b between prisms and the distance R_p of prisms from the jet impact on the number of jets n. The number of jets n is defined as $\frac{2\pi R_p}{a+b}$. The Figure 4.25 presents an overview of tested designs that correspond to combinations between these parameters. When the distances a_p and the R_p are constants, the investigation of the gap b is quite interesting to understand the sheet transition from a jet ligament to a *vss*. However, the jet ligament is more interesting than the sheet for the agronomic application. Hence, the value of the gap b should be inferior to the capillary length. Also, as a large number of jets

Table 4.9: Spray characteristics in terms of volumes corresponding to the non-textured disk and to textured designs TD_1, TD_4 and TD_5. The prisms are placed at three R_p that are respectively 15 mm, 22 mm and 28 mm. The measurements were performed at a Q = 2.8 10^{-5} $m^3.s^{-1}$. All configurations are compared to a reference standard agricultural flat fan nozzle *Teejet TP* 65 15 within the same spray class (extremely coarse (XC))

	Q (10^{-5} $m^3.s^{-1}$)	V_{10} (μm)	V_{50} (μm)	V_{90} (μm)	*RSF*
$Non-textured\ disk$	2.8	269.38	498.29	959.14	1.38
TD_1	2.8	590.7	801.12	992.80	0.5
TD_4	2.8	436.45	622.6	808.7	0.59
TD_5	2.8	360.18	558.12	749.5	0.5
Teejet TP 65 15	6.9	225	540	928	1.30

n is also desired, the gap b should be small as much as possible and it is fixed to 0.25 mm. Then, at this value of the gap b, by varying the base a_p of the prism, one established the limits for which jets may merge elastically and investigated the robustness of prisms with the decrease of a_p. One finds that a prism with a_p = 1.06 mm is the ideal configuration that resist to the flow impact and ensure a high number of jets n. Finally, by fixing the a_p and b at these values, one investigates the distance R_p of prisms where its limit was defined by the distance R' (for which holes appear). As a rule of thumb, one can increase the jet number n either by reducing the triangular prism size (a+b) or increasing the R_p. These parameters affect the sheet volume that influences the droplet size. In the Figure 4.26, the obtained V_{50} in the case of all configurations are plotted as a function of their number of jets n. The curve presents two parts. A first part corresponds to the of the V_{50} as the number of jet n increases. Then, one finds a stagnation part in which the V_{50} is almost constant with the increase of the jet number.

4.6 Droplet velocities

The droplet velocities are computed for the configurations involving two successive triangular prisms spaced by a gap b. The Figure 4.27 presents average droplet velocities as a function of their diameters. Each velocity per diameter class corresponds to the average velocity of at least 15 droplets. For all b configurations, the velocity curve is divided in

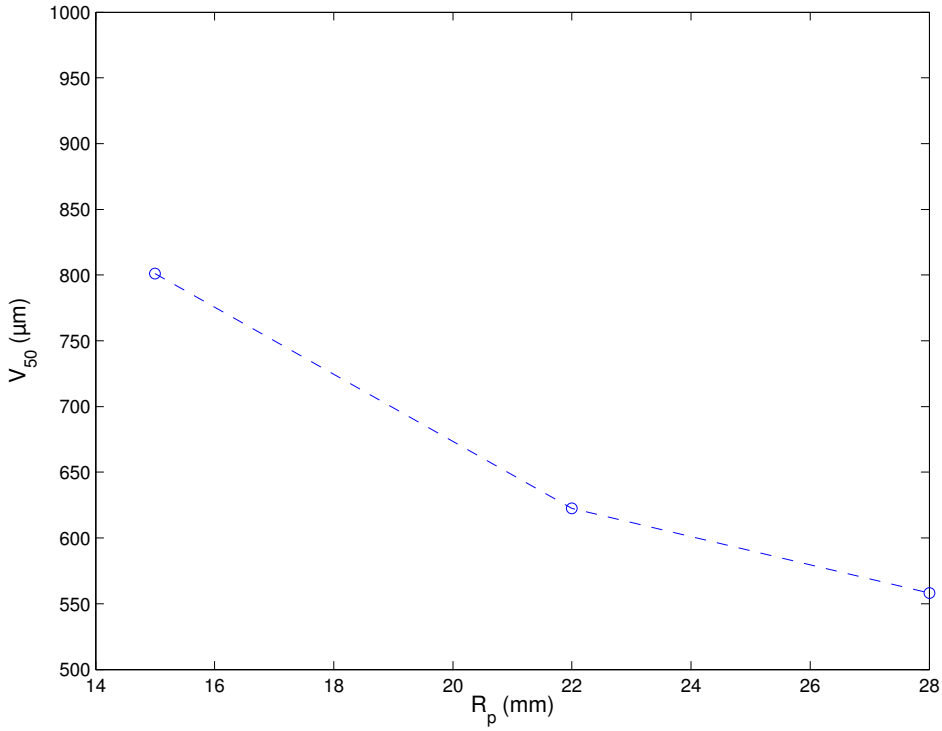

Figure 4.24: Evolution of the V_{50} as a function of the distance R_p of the prism from the jet impact. The gap b is fixed to 0.25 mm and the base of the prism a_p is fixed to 1.06 mm.

two parts. The first part is almost characterized by an abrupt slope of the curve for droplet diameters inferior to 400 μm. Then, droplets have almost constant velocities.

In the case $b = 0.25$ mm, droplet velocities are around 4.2 m.s^{-1}. The case $b = 0.51$ mm presents droplet velocities similar to the previous case. By the increase of b, the droplet velocities are increased and can reach 6.2 m.s^{-1} when $b = 7.31$ mm. As the b increases, the sheet portion entrapped in the gap is less decelerated. No comparison with the velocity of the free sheet is possible since the measurement were not performed at the same distance.

4.7 Conclusion

This study aims to control the turbulent Savart sheet by creating a local perturbation downstream the disk border. By taking into account to the limitation imposed by the holes

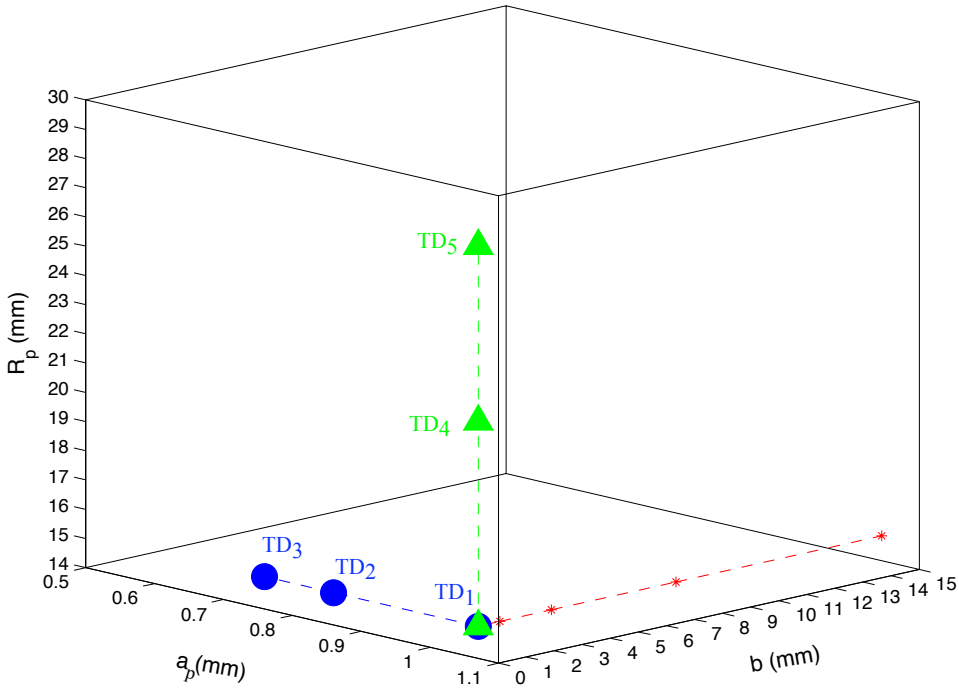

Figure 4.25: 3D representation of the parameters a_p, b and R_p corresponding to different disk configurations.

at R', the triangular prism has proved to be an efficient tool to break up the sheet. As a result, the sheet behavior is locally modified as the radial expansion is changed to be tangential close to both sides of the prism. An assembly of two successive prisms spaced b a gap b lead to the generation of a *vss* under the the effect of these tangential contributions. This *vss* converges to a jet ligament that disintegrates into droplets. A semi-empirical model was developed and it permitted to explain the formation of the *vss* through the gap. The transition between the *vss* and the jet ligament is directly linked to the competition between the inertia and the capillarity. When the gap b is inferior to the capillary length (= 3 mm in the case of the tap water), the capillarity dominates and the jet ligament is promoted in particular in case of small gaps. When the gap b between two prisms exceeds the capillary length, the inertia dominates and the the jet types coexist. Furthermore, when N triangular prisms are inserted radially in the sheet, the local perturbations interact together and lead to the generation of jets. Varying the the geometrical parameters of the prisms that are the prism base a_p and the gap b in addition to the flow rate Q, different

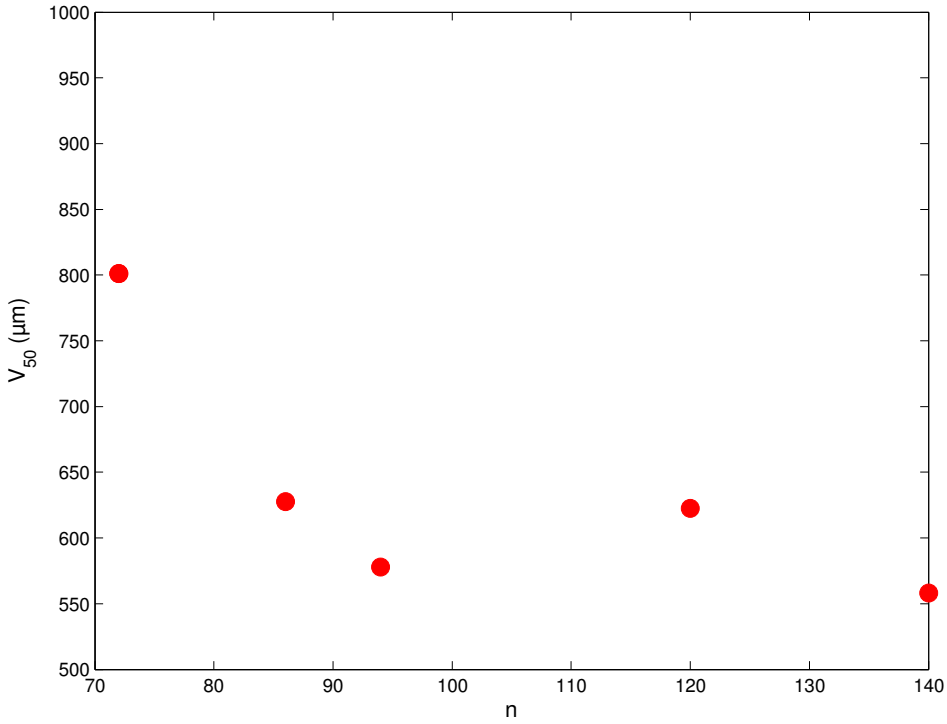

Figure 4.26: Evolution of the V_{50} as a function of the number of jets n. The number of jets n is equal to the number of prisms N since the jets are stable.

jet regimes are obtained and are presented in diagram phases. The jet number n can be stable where a jet per gap is generated ($n = N$) or unstable where elastic coalescences of neighboring jets may occur ($\frac{N}{2} \leq n < N$). The reduction of the a_p leads to the expansion the merged zone of jets.

The size of the generated droplets depends on the sheet volume that is entrapped in the gap. The V_{50} of the droplet size distribution can be reduced by increasing the jet number by reducing the a_p of the prism at the same radial distance R_p. Also, it can be reduced by increasing the R_p since the free sheet thickness decreases radially. Droplet velocities increase as the gap b increases.

To conclude, using N triangular prisms, one controlled the turbulent Savart sheet despite its complexity and one generates a stable number of jets n over an important flow rate ranges. This finding constitutes an advanced step compared to the results of Dressaire that tamed a laminar sheet and an innovation in the field of spray atomization. The present

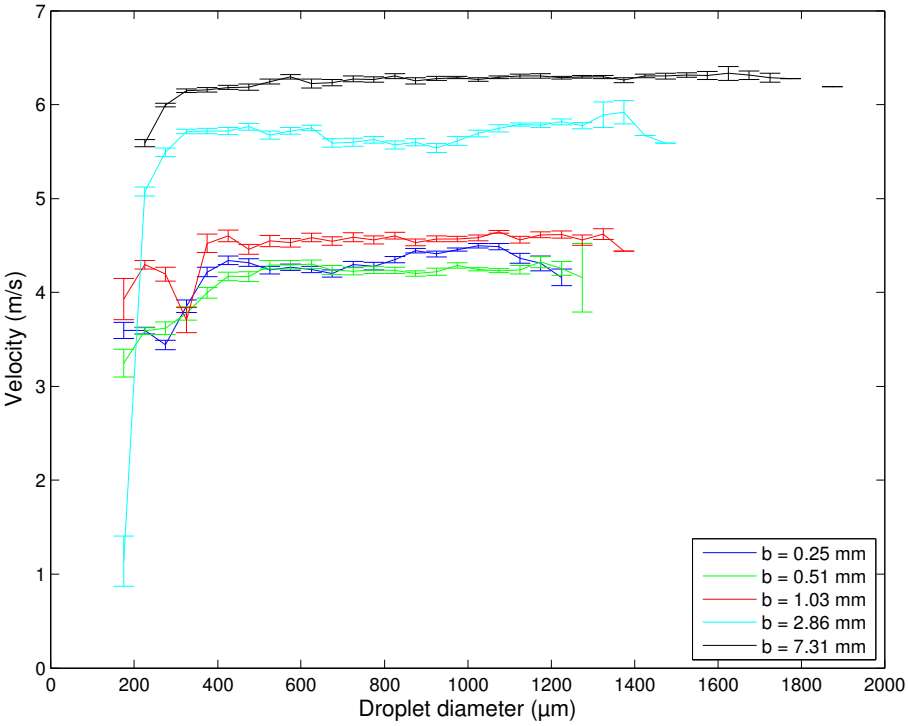

Figure 4.27: Representation of droplets velocities as a function of their diameters. The R_p is 15 mm. The measurements were performed at a $Q = 2.8\ 10^{-5}\ m^3.s^{-1}$.

configuration presents much flexibility on its geometrical parameters that are the size of the prism structure and its R_p permitting to increase the number of jets n and to reduce the V_{50}. In the present study, we reach 140 jets over 360° and a V_{50} around 558 μm. This spray characteristics are getting closer to that used in the agricultural field.

5

Discussion

Chapter 5

Discussion

Perturbation of the free Savart sheet using triangular prisms In the crop protection field, the Plant Protection Product (PPP) application may be performed at either low or high flow rates Q. For field treatments, a typical applied Q is around 1.6 10^{-5} $m^3.s^{-1}$ (= 1 $l.min^{-1}$) that is to be distributed among given number of jets n that depends on the geometry of the nozzle. The jets generate droplets which size and speed must be optimized for a maximum treatment efficiency in term of retention and drift. Results of numerical simulations showed that droplet diameters of 225 μm may offer high control of deposition by combining a low drift potential and moderate kinetic energy at the top of the canopy [18]. Droplets are ejected generally at 10 $m.s^{-1}$ using hydraulic nozzles. Therefore, the required jet number n is 111 jets for a Q = 1.6 10^{-5} $m^3.s^{-1}$. One also notes that agricultural nozzles present a spray angle opening between 80° and 140° and even 360° as for instance the Micromax 3s (case of the Controlled Droplet Application (CDA)). The required number of jets is generated from this spray angle opening.

The configuration of Savart namely a round jet impacting vertically a non-textured disk meets the requirements of agricultural nozzles and in particular the high flow rate ranges. The jet impact is turbulent by nature ($Re > 2000$) what may create local disturbances that are propagated downstream in the flow. Additional perturbations may arise from the setting of the gap H between the nozzle tip and the disk surface. In our case, when the gap H is smaller than 550 μm, the film thickness is no longer homogenous close to the

injector exit what drastically affects its radial expansion. A more sophisticated system could determine the H_{min} that can be reached.

Within this configuration (non-textured disk), the value of the ratio $X = \frac{D}{d}$ (D is the disk diameter and d is the jet diameter) affect the film velocity on the disk. The larger distance on the disk, the greater deceleration of the film until obtaining the hydraulic jump. Wetting properties of surfaces affect also the flow velocity. Hence, $X \sim 1$ is the best candidate to reduce not too much the film velocity and to develop a Savart sheet with the maximum expansion R. Then, the sheet thickness evolves in the air as $\frac{a}{2r}$ (a is the jet radius and r is the radial distance). This sheet is turbulent and contains holes that appears downstream (due to the turbulence) at a radial distance R' where $R' \leq R$. The holes are growing until they break up the sheet into ligaments and then into droplets. Free sheets obtained within the Savart configuration are similar to those produced by flat fan nozzles. The perforations are also observed (depending the properties of the spray mixture) in the case of hydraulic nozzles [54]. However, the sheet in the latter case is not decelerated since it directly evolves in the air. Moreover, the ratio X influences the droplet diameters. For a given flow rate Q, the larger X, the greater V_{50} (V_{50} increases from 498 μm to 1205 μm corresponding respectively to an increase of X from 2 to 10). This can be explained by the fact that configurations with small X values result in thinner film thickness and hence smaller droplet sizes. In general, the V_{50} depends on the film thickness h and on the flow rate Q. Also, the h may be decrease by acting on H since numerical simulations has shown that decreasing H may result in a reduced h what may reduce the droplet size [43]. The obtained velocities are 3 m.s^{-1} and 4 m.s^{-1} corresponding respectively to X values that are 10 and 2. The spray quality is extremely coarse and the droplet size distribution is wide. It is highlighted by a high RSF around 1 that is similar to that of hydraulic nozzles. This basic configuration of Savart is not quite interesting for the PPP application since it does not bring improvements in term of droplet sizes, speeds and trajectories.

(a) (b)

Figure 5.1: Illustration of the formation of jets at the disk border of two CDA atomizes: (a) Case of the Micromax 120 (Micron) (b) Case of the Girojet (Tenoma)

In the present study, the used liquid is tap water characterized by a high surface tension (73.5 ± 0.3 mN.m^{-1}). By changing the physicochemical properties of the liquid, the behavior of the Savart sheet obviously changes. The additives added to the spray mixture in the PPP field act mostly on its surface tension and on its viscosity (Newtonian and non-Newtonian liquids). For instance, the widely anti-drift adjuvants that are used as an alternative strategy to mitigate the spray drift are classified into two categories: polymers of high molecular weight and dilute oil-in-water emulsions (its use is more recent) [55]. Polymers such as the guar gum increase the viscosity what enhances the stability of the sheet. Similar sheets obtained by the impact of a droplet on a disk and based on a mixture of water and polymer lead to long ligaments arising from the sheet rim. These ligaments are destabilized into large droplets [56, 57]. In the case of dilute oil-in-water emulsions, the surface tension is decreased. However, non-wettable particles, such as oil droplets, are found to puncture the liquid film leading to additional perforations. These additional perforations are located closer to the nozzle where the sheet is thicker. As a consequence, the droplet size increases [54, 57]. On the other hand, the use of a surfactant as for instance the Break Thru S240 (Evonik Industries AG, Essen, Germany) [16] reduces the surface tension what may delay the appearance of holes. The surfactant increases also the elastic viscosity. In the case of the flat fan nozzle, it results in the stabilization of the sheet rim what may shift the break-up of the sheets to larger flow rates Q [58]. It will probably induce the same effect as in the case of flat fan nozzle.

The first strategy to tame the turbulent sheet is to split it into individual jets using a disk engraved along its circumference by a number N of radial grooves (Chapter 3). One acts acts on the semi-free film on the disk. To obtain enough jets in respect to the agronomic requirement one needs an impact disk of intermediary size ($X = 10$): large enough to engraved a lot of grooves but small enough to avoid the hydraulic jump. For the current groove geometry (1mm of width and 5 mm of length), one can generate maximum 72 jets over 360 ° (at a radial distance 15 mm from the jet impact) where $n = N$ or $n = 2N$ (see Figure 3.6 in Chapter 3). The number of jets n in both cases is stable over a wide flow rate Q ranges. The regime $n = 2N$ presents two jets located in different planes what may avoid jet coalescences. Jets break up in a transitional regime between the Rayleigh-Plateau regime and the first wind. By decreasing the groove width to 750 μm or 500 μm instead of 1 mm, the two latest regimes are no longer valid and elastic jet coalescences

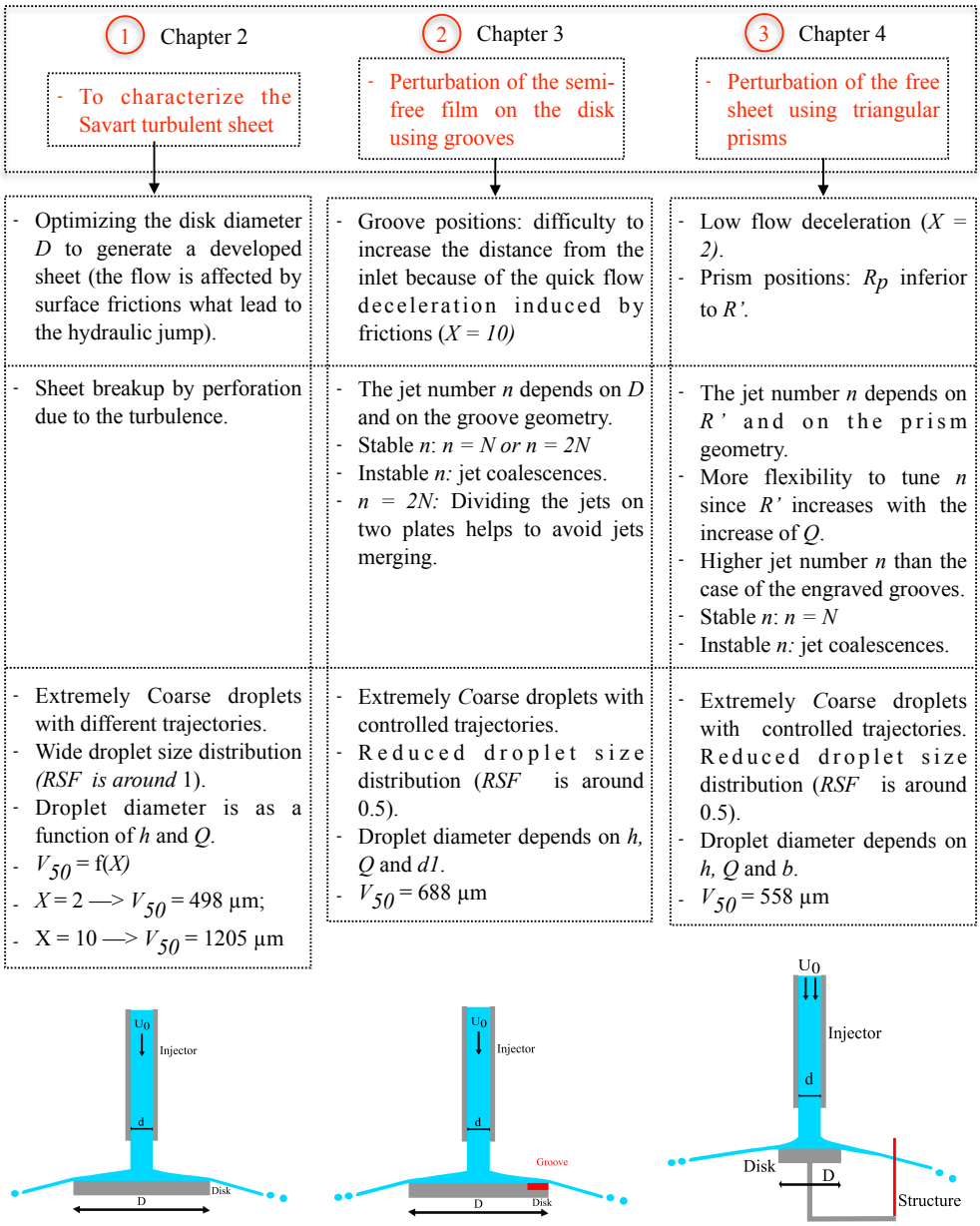

Figure 5.2: Overview of the methodology used to control the turbulent sheet and main results arising from each disk configuration.

occur. Compared to hydraulic nozzles, the used grooves have proven their ability to control the jet number and trajectories. Moreover, the droplet diameters are a function of the

film thickness h, the flow rate Q and the liquid volume entrapped in the gap $d1$ between two successive textures. When h and Q are constant, the smaller jet volume, the more reduced droplet diameter. The quality of the produced spray is extremely coarse (V_{50} are around 650 - 700 μm) and the jet velocities are around 4 m.s^{-1}. The droplet size distribution is reduced and it is corroborated by low RSF values around 0.5. The current design offers more parameters to tune the V_{50} compared to hydraulic nozzles where the the V_{50} is only linked to the pressure. Also, one reduces the extent of the droplet spectrum by decreasing the RSF from 1 to 0.5. However, the flow speed is subjected to a continuous radial deceleration from the inlet.

As the jet number is low (72 jets over 360 °) and the quality of the spray is extremely coarse (V_{50} are around 650 - 700 μm), this configuration can be useful for the anti-drift application at low flow rates as for instance 0.5 l.min^{-1}. The reduced droplet size distribution can be a potential alternative to reduce the off-target proportion of big droplets of low drift nozzles (having the same V_{50}). In addition, the design could be also composed by two symmetric parts of splash nozzles (similar to mirror nozzles). Each part contains 30-35 jets depending on the spray angle opening.

The second strategy to tame the turbulent sheet is to insert N triangular prisms directly in the free sheet (Chapter 4). In this situation, the choice of X is a compromise between two main factors: one must firstly avoid the deceleration of the flow on the disk surface as much as possible. Secondly, the disk diameter is sufficient large to create a well developed Savart sheet (with a maximum expansion R) where N prisms are positioned at a distance R_p of the prisms from the jet impact. In practice, the parameter X was fixed to 2. Therefore, one have similar sheet conditions to those obtained with hydraulic nozzles since the flow velocity is less subjected to surface frictions and the sheet is almost prone to air shear. The sheet thickness evolves in the air as $\frac{a}{2r}$. The larger distance, the thinner sheet thickness. In addition, R increases with the increase of the flow rate Q. By the insertion of N prisms in the sheet, one can generate a stable jet number n over a wide flow rate Q ranges where $n = N$ (see Figure 4.15 in Chapter 4). As R increases with the increase of Q, this result is quite interesting to increase the number of jets n and reduce the droplet size in the case of prisms. This original configuration offers more flexibility to tune the number of jets n as it depends on R' and R and the geometry of the prism. At a given distance R_p of the prisms from the jet impact, the jet number is increased by decreasing the base a_p of the

prism. However, a_p should be not too small in order to resist to the flow impact and also to avoid jet coalescences. The R_p must be inferior to R'. The larger distance R_p in the free sheet, the higher jet number n and the lower V_{50}. With the current configuration (the base a_p = 1 mm and b = 250 μm as a gap between two successive prisms), one can generate around 140 jets over 360 °. The V_{50} are around 500 μm and the droplets velocities are around 5 m.s^{-1}. These spray characteristics are closer to that of hydraulic nozzles and in particular low drift nozzles. The current configuration may be used at either low or high flow rates rates Q by adjusting the right number of jets through the design of mirror nozzles. Additional experiments investigating the influence of H and X on the droplet size should be performed to validate the nozzle for further application.

The number of jets n and their homogeneities (individual jets without coalescences) within the spray is commonly issued for the agricultural nozzles. The CDA technology is able to deliver a sufficient jet number because of its large disk diameter. For example, the Micromax 120 (Micron) with a 120 ° spray angle opening presents a disk diameter of 120 mm. The rotating serrated disk has deep grooves with a 1 mm of width leading to 126 individual jets ejected by teeth from the 120° opening (Figure 5.1a). However, other CDA atomizers as for instance the Girojet (Tecnoma) experienced problems related to the uniformity of the jets at the the border of its serrated disk. The jets are not ejected from the gap between two successive teeth for all tested flow rates (Figure 5.1b) what may affect the number of jets and the droplet size distribution. In the present study, grooves and prisms have proven their performance and robustness (phase diagram) to control the number of jets n over a wide flow rate ranges.

Furthermore, droplets are emitted in the air and their shapes are not stable since they interact with the air. If droplets adopt a spherical shape, the surface forces must exceed the air friction. This can be written dimensionally as follows [59]:

$$\rho_a U_D^2 R_D^2 < \sigma R_D \tag{5.1}$$

with ρ_a is the air density, U_D is the droplet velocity, R_D is the droplet radius and σ is the surface tension of the liquid. Based on 5.1, the critical value of R_D for which droplets are

subject to deformations is as follows:

$$R_D = \frac{\sigma}{\rho_a U_D^2} \tag{5.2}$$

For example, in the case droplets are emitted with a velocity U_D of 4 m.s^{-1}, the critical value of R_D is around 5 mm and hence droplet diameters of 10 mm. However, our droplet diameters are too small and they never exceed 1 mm. Therefore, droplets are spherical and surface forces dominate.

To conclude, the current designs (grooves and prisms) permit to overcome difficulties encountered in the CDA technology (see Chapter 1). Indeed, these new designs are simple as the configuration is composed of a jet impacting on a disk without integrating centrifugal forces (rotating disk) what may reduce their costs. They are also easy to manufacture using 3D printers. Then, their weight is not too heavy that is close to that of current hydraulic nozzles. Moreover, they are easy to mount on a spray boom using nozzle holders. In practice, these designs may initially adopt a spray opening of 360° (similar to the case of CDA devices as for instance micromax 3s) and are mounted on the boom 0.5 m above the crop. The generated droplets are emitted with an horizontal speed of maximum U_D = 4 m.s^{-1}. Hence, considering a parabolic trajectory for the droplet, at maximum, the produced droplets covered a space up to 1.25 m from each side of the nozzle. Several designs may be mounted on the boom by spacing them by a distance inferior to 1.25 m in order to ensure a good overlapping of nozzles. Finally, these designs offer several parameters to control droplet sizes and velocities (that depend on design configuration) in addition to the flow rate Q.

An overview including the methodology followed to tame the turbulent sheet and main results of each scenario discussed in this chapter are presented in the Figure 5.2.

6

Conclusion and perspectives

Chapter 6

Conclusion and perspectives

The actual hydraulic nozzles do not meet the challenges facing the PPP application with respect to the efficiency and the environmental requirements. More sophisticated nozzles with more precision in droplet sizes, velocities and trajectories are required. I started from the statement that the configuration of Savart namely the impact of a jet on disk is the ideal candidate that meets the agricultural nozzle requirements. As high flow rates Q are needed, the jet impact is turbulent by nature and so is the Savart sheet. Indeed, the liquid flows radially and leads to a turbulent sheet evolving in the air. The challenge is to tame the turbulent sheet into droplets. The methodology consists in splitting the sheet into individual jets using textured disks by acting on the semi-free film or by inserting triangular prisms directly in the free sheet. The sheet ideally breaks up according to the Plateau-Rayleigh mechanism. This process leads to a narrower droplet size distribution.

The previous methodology is directly linked to the value of the ratio $X = \frac{D}{d}$ (D is the disk diameter and d is the jet diameter). If $X >> 1$, the flow is subjected to a quick deceleration from the jet impact. The larger distance on the disk, the greater deceleration of the film what promotes the formation of the hydraulic jump. Therefore, the configuration $X >> 1$ is not interesting for the intended methodology. When $X \sim 1$, the film flows radially on the disk and leads to a free Savart sheet. Hence, $X \sim 1$ is the appropriate configuration to apply both disturbance techniques. Outside the disk, the free Savart liquid sheet is characterized by holes at a radial distance R' (due to the turbulent regime). The resulted

droplets presents a wide size distribution characterized by a high RSF fluctuating around 1 that is similar to the case of hydraulic nozzles. By the insertion of N radial grooves on the disk circumference ($X = 10$), one controls the turbulent flow and the film is split into jets before reaching the disk border. The number of jets n depends on h, Q and the gap between two grooves $d1$. According to the phase diagram, the jet number n can be either stable where $n = N$ or $n = 2N$ or unstable where jets may merge elastically. Stable jets are generated over a wide range of flow rates. The $n = 2N$ presents two jets emitted in two different planes what may help to avoid the jet merging. The reduction of the groove width generates a large number of jets but it results in elastic jet coalescences. The difficulty level is extremely high to reach the desired jet numbers (f(Q)) since we are limited by the size of the groove and the quick deceleration of the film on the surface. Only 72 jets are generated over 360°. The quality of droplets are extremely coarse, one finds that the V_{50} is around 650 - 750 μm.

Using N triangular prisms positioned directly in the sheet, one also controlled the turbulent Savart sheet. This configuration presents much flexibility to tune the jet number n. This number of jets n depends on the size of the prism and the distance R_p relative to the natural destabilization of the sheet at R'. The number of jets n can be either stable where $n = N$ or unstable where jets may merge. The V_{50} is reduced by either decreasing the base of the prism a_p at a radial R_p or by increasing R_p. In the present study, one reaches 140 jets over 360° and a V_{50} around 558 μm. These spray characteristics are close to that of low drift nozzles. Additional trials must be conducted to investigate the influence of H on the droplet diameter as it has been shown that the decrease of H induce a decrease of h. Furthermore, the technical solution adopted by Clanet and Villermaux [10] that allows to generate a laminar flow through the injector exit even at high Q values could be an alternative solution to increase downstream the position of prisms in the sheet (by avoiding the appearance of holes). Therefore, the height of the sheet will decrease and results in smaller droplet sizes.

Perspectives

This experimental research explores original ways to split a turbulent liquid sheet into individual and homogeneous jets with respect to the PPP application field. This has opened new perspectives as follows:

1. Spray formulation

Additional experiments investigating the influence of properties of the spray mixture on the formation of jets and droplets from both disk configurations are needed. In particular, the distance R_p of prisms in the sheet should be checked. For instance, one can change both the surface tension and the viscoelasticity of the spray mixture by adding the surfactant Break Thru S240 (Evonik Industries AG, Essen, Germany). One can also investigate some anti-drift adjuvants such as Li700 (Agridyne) that acts also on the surface tension or polymers as for instance the guar gum that acts on the spray mixture viscosity.

2. To find the optimum parameter for application

The reduced droplet size distribution of sprays produced by both disk configurations could be investigated in term of drift reduction and retention efficiency. At the laboratory scale, one can investigate outcomes of droplet impacts on different surface targets (surface properties and orientations) using a dynamic spray application bench at Gembloux Agro-Bio Tech. Then, their spray retention efficiency is to be compared to standard hydraulic nozzles with the same spray class. In the drift side, one can perform drift trials in a wind tunnel. The potential drift of sprays is investigated at 2 m from the nozzle at 2 $m.s^{-1}$ of wind speed. Their drift reduction performance is compared to standard anti drift nozzles. Afterwards, by adjusting the appropriate parameters of these configuration in droplet characteristics, they could be used in the field as for instance in the application of herbicides of contact.

3. Development of nozzle design for precision agricultures

The design including prisms and grooves may opens new perspectives in term of potential nozzle design. For instance, prisms may be investigated in the case of flat fan nozzles i.e. They can be positioned in the sheet produced through the calibrated pore of a flat fan nozzle. We check then the breakup of the sheet into jets and the uniformity of droplets. Moreover, similar configurations namely the impact of a droplet on a surface with a specific geometry could improve the efficiency of the spot spraying technology in term of droplet sizes. It has proven that the droplet impact may result in a numerous and individual jets (depending on the impactor geometry and the spray mixture) that break up into droplets according to the Rayleigh-Plateau [57].

7

Appendix: Dewetting

Chapter 7

Appendix: Dewetting

We propose to study the response of a turbulent liquid film, that results from the impact of a turbulent round jet on the impactor, to an asymmetric disturbance using a thin pin. The disturbance is applied locally across the film at a radial distance from the jet axis. The disturbance process can be either rapid or progressive i.e the film is perturbed from the free film surface towards the impactor surface and conversely. Here, the film dynamics on the disk and on the air downstream the disturbance are studied.

7.1 Experimental setup and used techniques

7.1.1 Setup description

The glass injector generated a jet with a diameter $d = 2R = 3$ mm was set vertically to the centre of a motionless disk. The jet is characterized by a Reynolds number $Re = \frac{U_0 d}{\nu}$ (ν is the kinematic viscosity). The gap H between the injector tip and the disk was tuned by a three axis precision displacement tool and H was set 550 μm. Much interest was devoted to the finish of the injector exit that was carefully sanded to homogenize its surface regularity and flatness and hence, to homogenize the flow thickness close to the injector exit. The disk under consideration was fixed on a support that was in the middle of a 200 mm

side cubic plexiglass tank (figure 1). The used liquid was tap water at 20 °C (surface tension $\sigma = 72$ mN.m^{-1}, density $\rho = 1000$ kg.m^{-3} and kinematic viscosity $\nu = 10^{-6}$ m^2.s^{-1}). The tap water was injected and recirculated using a gear pump (Ismatec BVP-Z) combined with a pump head to deliver steady flows. The flow was measured by weighing the liquid poured into a graduated tank during 30 s and three repetitions were performed for each flow measurement. Flow rates were linked to the pump rotation speeds. The highest flow rate can be reached was 9.7 10^{-5}m^3. s^{-1} corresponding to a $Re = 41182$. The Re were calculated to range between 4258 and 24772 which corresponded to a turbulent impact on the disk.

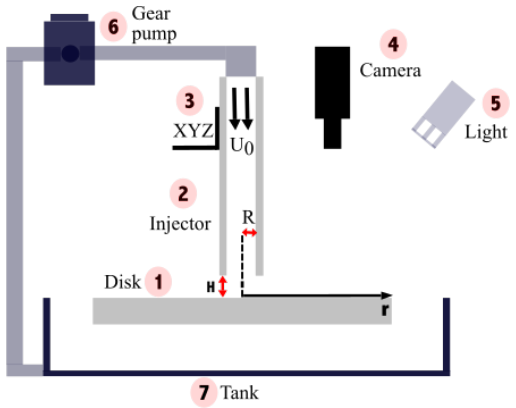

Figure 7.1: The experimental setup is constituted of a glass injector (2) that generated a round jet $d = 2R = 3$ mm and impacted with a velocity U_0 the center of an impactor (disk) (1). The disk was placed in the middle of a 200 mm side cubic tank (7). The gap H between the injector tip and the disk was tuned using a precision displacement tool XYZ (3). A high-speed camera (4) was mounted vertically to the disk to record images of liquid sheet. In the the plexiglass disk, a mirror was tilted by 45° to the camera optic axis in order to reflect the light (5) towards the disk. Otherwise, the light device was used to illuminate the opaque disk surface. The liquid was injected by the gear pump (6) connecting the tank to the injector.

7.1.2 Technique of the flow disturbance

Here we used a simple pin to disturb locally the radial thin film. The pin diameter would be in the order of magnitude of the film thickness and it was arbitrarily set 300 μm. The pin was placed downstream the radial flow emanating from the injector exit. Since the velocity profile in the thin film changes from the disk surface to the free surface, one proceeds to

a progressive disturbance of the film with two manners: One excites the slowest part of the film by moving the pin from the disk surface towards the free surface of the liquid and conversely. The two previous disturbances manners influenced the setup complexity (properties of the disk and the pin).

In the case of a local disturbance performed from the disk surface towards the film free surface, two configurations were established. Firstly, the first disk was made of a plexiglass cut using a laser cutter (Trotec). The disk contained a calibrated hole with a diameter of 330 μm $\pm$ 20 μm through which the pin slid freely. The pin was a simple needle and it had a diameter of 300 μm and a flat tip. The displacement of the thin needle was carefully ensured by a three axis precision displacement tool that could achieve a displacement of 10 μm (figure 2, a). The second disk configuration presented a unique piece that gathered both the disk and the pin and it was performed using a 3D printer (Stratasys). The disk surface is opaque and it is constituted of a complex polymer (Veroblue RGD840). The integrated pin had also a diameter of 300 μm and different heights. As a consequence, one requires more than one disk to explore the whole flow thickness with small displacement steps (figure 2, c). On the other hand, in the case of a disturbance performed from the upper part of the thin film towards the disk surface, only the technique based on the movable needle was used (figure 2, b). The static wetting of the tap water on the two disk surfaces was characterized by a measured contact angle using an optical contact angle meter (CAM 200 KSV). The obtained contact angles on the plexiglass and opaque disks were respectively 74° and 25 °.

7.1.3 Image acquisation

A high speed camera Y4 (IDT motion) recorded the fluid motion from the top. In the case the disk was opaque, a light device was used to illuminate the disk surface and we used a black dye to have a good contrast. When the disk surface was a plexiglass, a mirror was tilted by 45° to the camera optic axis and it reflected the light set perpendicularly to the mirror. The images were acquired at a frequency of 2000 Hz and treated with an image analysis code developed in Matlab.

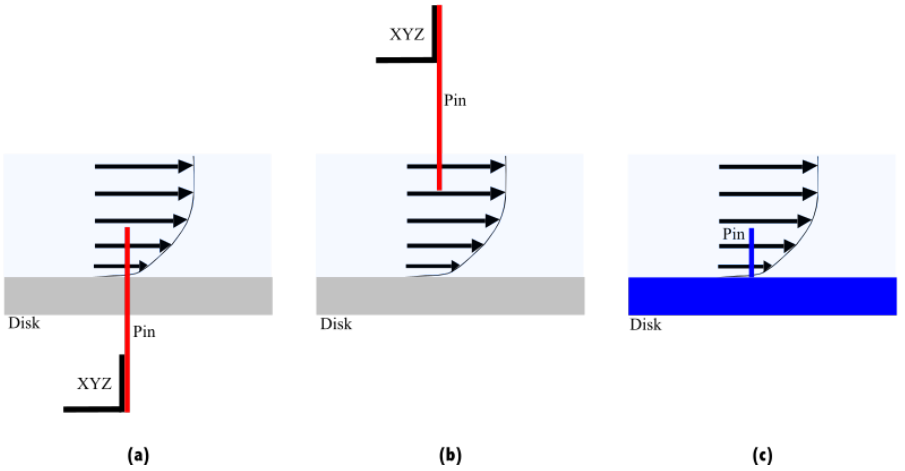

Figure 7.2: In the case of a local disturbance of the film performed from the disk surface towards the film free surface, (a) the disk is a plexiglass cut and a sliding thin needle through a calibrated hole is used. The thin needle started its calibrated vertical displacement from the surface disk towards the film free surface, (c) The disk and the pin are an entire piece and made by a 3D printer. Different heights of the pin are performed regarding the film thickness. Within a disturbance in the other direction, (b) only the sliding thin needle through the hole in the plexiglass disk was used.

7.1.4 Film mean velocity

The film mean velocity $U(r)$ at a given radial distance from the injector exit was obtained through the local measurement of the liquid film thickness. The film mean velocity is therefore: $U(r) = \frac{Q}{2\pi rh}$ (with U: film mean velocity, Q: injected flow rate, r: flow radial distance and h: film thickness). The thickness was measured experimentally using a simple technique described by Azuma and Toshino [50]. A thin needle in the order of magnitude of the film thickness was lowered down using a three axis precision displacement tool (XYZ) towards the liquid surface. As a result, a droplet was rapidly formed on the needle tip. Then, the liquid flow was stopped and the needle was lowered down towards the disk surface. Hence, the difference between both heights gives the film thickness. The measurement process was eye-guided using the images from the high-speed camera Y4 optic axis which was set perpendicularly to the needle axis, on the same plane as the disk surface.

7.2 Film behavior on the disk downstream the disturbance

7.2.1 Qualitative view and experimental measurements

7.2.1.1 Case of a pin with a big (infinite) length across the film

When the turbulent jet impacted the plexiglass disk with a big diameter (= 500 mm), as expected, the flow spread out radially and ended up being decelerated and hence, leading to an hydraulic jump. Firstly, one simply proceeded by disturbing locally the radial flow using a thin needle with a diameter of 300 μm and a big length (= 40 mm). The needle crossed vertically the whole flow at a radial distance prior the hydraulic jump. As a result, a wake was firstly observed close to the needle. Then, downstream the wake, a steady opening in the film, that reflected a steady recession of the edge of the film, lead to a de-wetting of the surface prior the hydraulic jump. However, the decelerated liquid resulting from the hydraulic jump was accumulated and hence, it filled quickly the de-wetted surface. One found a method to simply evacuate the decelerated liquid and to keep the stability of the de-wetting. The impactor was limited to a rectangular surface with a length of 100 mm and a width of 20 mm that took into consideration the diameter of the jet (d = 3 mm). There were certainly boundary effects of the rectangle edges on the flow but they didn't influenced the formation of the de-wetting (figure 3).

Moreover, one investigated the radial distance r at which the de-wetting of the surface occured. Figure 4 illustrated the evolution of r for different pin positions from the jet axis as a function of the flow rate Q. The pin positions were 5 mm, 10 mm, 15 mm and 20 mm from the jet axis and the radial distance corresponding to each pin position are respectively $r_{Pin\ position:\ 5\ mm}$, $r_{Pin\ position:\ 10\ mm}$, $r_{Pin\ position:\ 15\ mm}$ and $r_{Pin\ position:\ 20\ mm}$. One also measured the radius of the hydraulic jump designed by $r_{hydraulic\ jump}$ as a function of Q. This latter was computed using a spatial measurement based on one image for a given Q. It corresponds to the mean value of 10 measurements of the radius curvature sampling the entire radius of the hydraulic jump. All the radii were taken at the same angular coordinates as in the first measurement with the increase of Q.

All curves can be divided in two parts. The first part showed that all curves were superimposed and had the same slope where radii increased as Q increased. The de-wetting

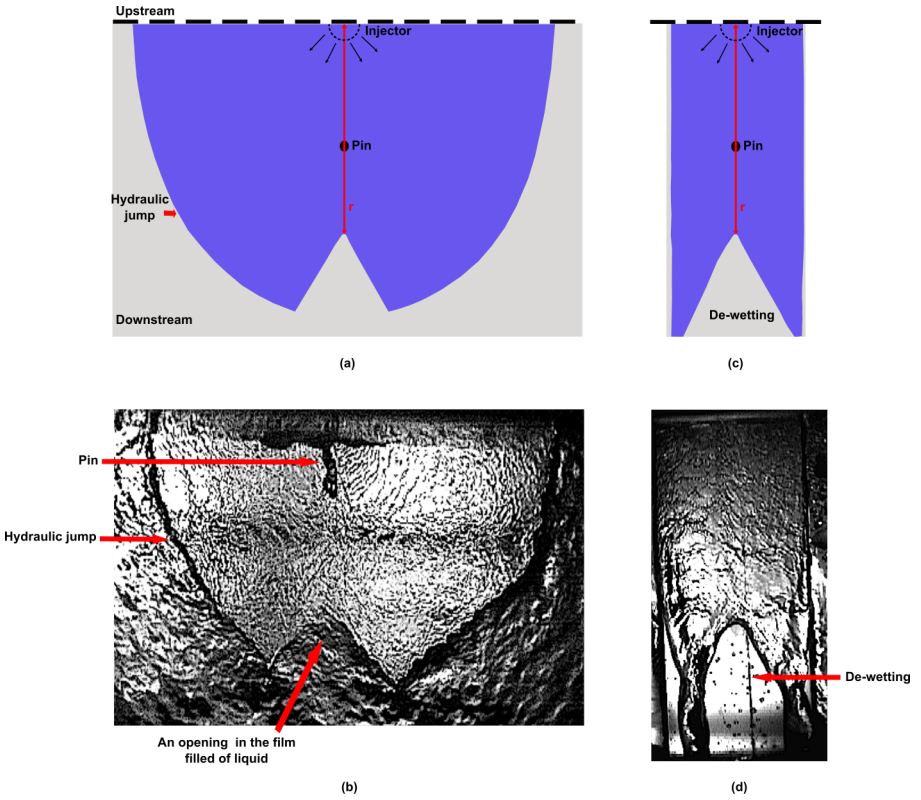

Figure 7.3: Illustration of a local disturbance of a radial film using a pin: (a) A sketch of a steady opening in the film downstream the wake (close to the needle) and prior the hydraulic jump. This opening lead to a de-wetted surface that was quickly filled of the neighboring accumulated liquid resulting from the hydraulic jump. The de-wetting occured at a radial distance r downstream the pin. (c) A sketch of new configuration of the impactor: By adopting a rectangular shape of the impactor, the decelerated liquid from the hydraulic jump was easily evacuated and the de-wetting of the surface downstream the needle was maintained. (b) and (d) represented the experimental figures corresponding respectively to (a) and (c).

in the wake downstream the needle was either absent or was occured and absorbed by the hydraulic jump regardless the pin position in the radial film. Indeed, the applied Q was low that lead to a low mean film velocity U and hence, the disturbance was so small that we failed to induce the de-wetting downstream. From a threshold value of $Q = 2\ 10^{-5}\mathrm{m}^3.\mathrm{s}^{-1}$, the opening in the wake that lead to a de-wetted surface appeared and remained steady i.e it moved away from the hydraulic jump inwards and hence, r decreased compared to that of the hydraulic jump. Here, thanks to the increase of U for a given radial position, the disturbance was sufficient to induce the de-wetting downstream. Also, r increased with

the increase of Q but it remained inferior to that of the hydraulic jump. In case the pin was put 5 mm from the jet axis, r presented the lowest values with the increase of Q i.e the de-wetting appeared rapidly downstream the pin. Here, at 5 mm from the jet, U had the greatest values that corresponded to a greater disturbance because of the radial decrease of U for a given Q. Therefore, the closer pin to the jet axis, the greater disturbance downstream the pin and the reducer r.

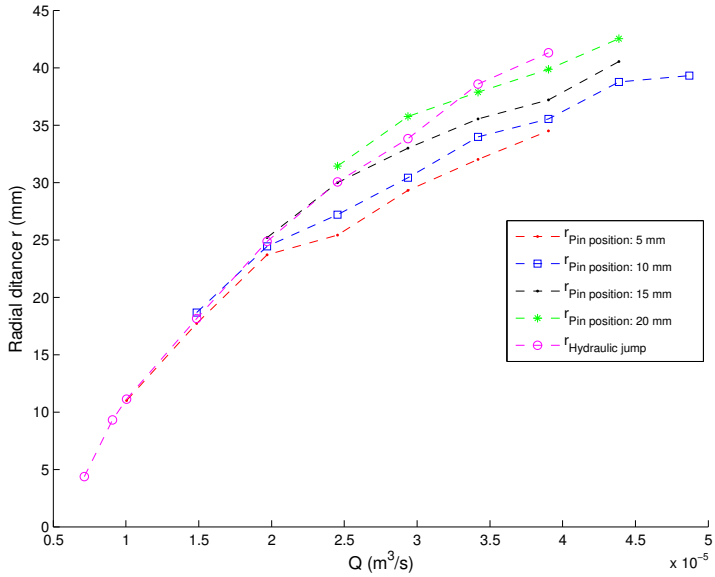

Figure 7.4: Evolution of the radial distance of the de-wetting r for different pin positions from the jet axis as a function of the flow rate Q. The pin was put 5 mm, 10 mm, 15 mm and 20 mm downstream the jet axis. The radial distance corresponding to each pin position were respectively $r_{Pin\ position:\ 5\ mm}$, $r_{Pin\ position:\ 10\ mm}$, $r_{Pin\ position:\ 15\ mm}$ and $r_{Pin\ position:\ 20\ mm}$. The radius of the hydraulic jump is measured and indicated by $r_{hydraulic\ jump}$.

7.2.1.2 Case of a pin with a finite length

One performed a progressive disturbance across the radial film at 10 mm from the jet axis. Firstly, one interested to the disturbance that occurs from the impactor surface inwards the film. The figure 5 presented the evolution of the radial distance r as a function of the pin height P_h for two flow rates Q_1 and Q_2 which are respectively 2.94 10^{-5}m^3.s^{-1} and 3.9 10^{-5}m^3.s^{-1}. In the case the disk was opaque, the de-wetting only appeared from a critical P_{hc} = 50 μm and r presented the greatest value (r = 52 mm) since the slowest part

of the flow was only disturbed that lead to a small disturbance. The more one attacked the film inwards the more r decreased. Once the pin exceeded the film height corresponding to P_h = 300 - 400 μm, the r value was around 30 mm. Then, it remained almost constant with the increase of P_h that was close to the value of r measured within the case of a pin with a big length for the same Q_1 (figure 4). When Q increased and $Q = Q_2$, the de-wetting occured at the same radial distance r and P_{hc} as in Q_1. Then, the radial decrease of r was similar as in $Q1$. When P_h = 300 - 400 μm, r oscillated between 35 mm and 40 mm that was close to that measured within the case of a pin with a big length for the same Q_2 (figure 4).

On the other hand, in the case the disk was plexiglass and $Q = Q_1$, the de-wetting was always observed even the pin was absent i.e P_h = 0 and the pore of 300 μm disturbed the film. The curve presented three parts as follow: The first one was characterized by an almost constant value of r around 38 μm as P_h increased. The constant r value corresponded to the combined effet of the pin and the pore. Then, a slight decrease of r was observed corresponding to P_h values between 600 μm and 800 μm that corresponded to a transitional stage. When the P_h exceeded 800 μm, r = 30 mm and it remained constant as P_h increased. Hence, one fond the same case as the pin with a big length for the same Q_1 (figure 4). When $Q = Q_2$, the curve had kept the same shape as that in Q_1 and r was slightly increased as expected.

In the case the disturbance occured from the free film surface towards the impactor surface, one also performed a progressive disturbance across the radial film at 10 mm from the jet axis. The figure 6 presented the evolution of the radial distance r as a function of the pin height P_h for two flow rates Q_1 and Q_2. In this configuration, P_h indicated the distance between the needle tip and the impactor surface. When $Q = Q_1$, r remained almost constant with the progressive increase of the pin towards the impactor. This could be explained by the fact one started disturbing the accelerated part of the film and hence, the value of r was close to that obtained with a pin with a big length. When $Q = Q_2$, the curve had kept the same shape and r increased as expected et its value was slightly above to that measured with a pin with a big length at Q_2.

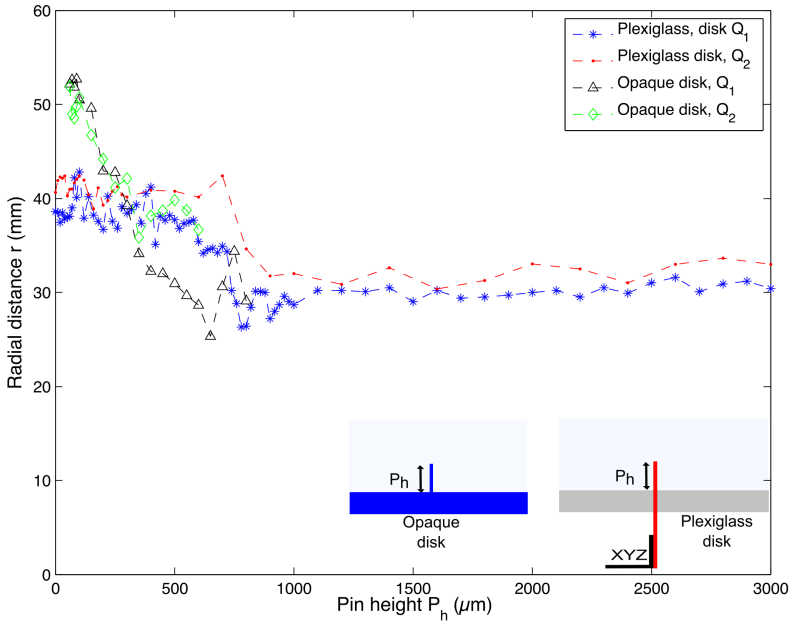

Figure 7.5: Investigation of the radial distance of the de-wetting r as a function of the pin height P_h for a given flow rate. The disturbance was performed from the impactor surface (P_h = 0) towards the liquid free surface. Two types of surface impactors (Plexiglass and opaque) were tested under two flow rates Q_1 and Q_2 which were respectively 3 10^{-5} $m^3.s^{-1}$ and 4 10^{-5} $m^3.s^{-1}$.

7.3 Conclusion

This study is still under investigation.

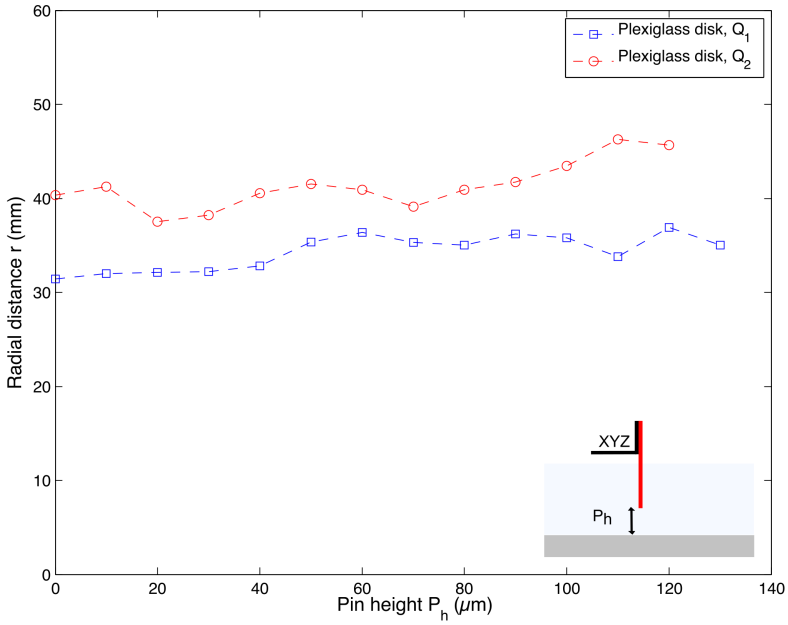

Figure 7.6: Investigation of the radial distance of the de-wetting r as a function of the pin height P_h for a given flow rate. The disturbance was performed from the impactor surface towards the liquid free surface. Two types of surface impactors (Plexiglass and opaque) were tested under two flow rates Q_1 and Q_2 which were respectively 3 10^{-5} $m^3.s^{-1}$ and 4 10^{-5} $m^3.s^{-1}$.

Bibliography

[1] Bastian Bonhoeffer, Arno Kwade, and Michael Juhnke. Impact of formulation properties and process parameters on the dispensing and depositioning of drug nanosuspensions using micro-valve technology. *Journal of pharmaceutical sciences*, 106(4):1102–1110, 2017.

[2] Nicolas De Cock. *Design of a hydraulic nozzle with a narrow droplet size distribution*. PhD thesis, 2017.

[3] JCP Huang. The break-up of axisymmetric liquid sheets. *Journal of Fluid Mechanics*, 43(2):305–319, 1970.

[4] Emilie Dressaire, Laurent Courbin, Adrian Delancy, Marcus Roper, and Howard A Stone. Study of polygonal water bells: inertia-dominated thin-film flows over microtextured surfaces. *Journal of Fluid Mechanics*, 721:46–57, 2013.

[5] Emilie Dressaire, Laurent Courbin, Jérome Crest, and Howard A Stone. Inertia dominated thin-film flows over microdecorated surfaces. *Physics of Fluids*, 22(7): 073602, 2010.

[6] Baptiste Néel and Emmanuel Villermaux. The spontaneous puncture of thick liquid films. *Journal of Fluid Mechanics*, 838:192–221, 2018.

[7] Henri Lhuissier, Philippe Brunet, and Stéphane Dorbolo. Blowing a liquid curtain. *Journal of Fluid Mechanics*, 795:784–807, 2016.

[8] Jose Manuel Gordillo, Henri Lhuissier, and Emmanuel Villermaux. On the cusps bordering liquid sheets. *Journal of Fluid Mechanics*, 754:R1, 2014.

[9] Christophe Clanet and Emmanuel Villermaux. Life of a smooth liquid sheet. *Journal of fluid mechanics*, 462:307–340, 2002.

[10] Emmanuel Villermaux and Christophe Clanet. Life of a flapping liquid sheet. *Journal of fluid mechanics*, 462:341–363, 2002.

[11] Taylor. The dynamics of thin-sheets of fluid. i. water bells. 253(1274):289–295, 1959.

[12] Graham Matthews. *Pesticide application methods*. John Wiley & Sons, 2008.

[13] ESE Southcombe, PCH Miller, H Ganzelmeier, JC Van de Zande, A Miralles, and AJ Hewitt. The international (bcpc) spray classification system including a drift potential factor. In *Proceedings of the Brighton Crop Protection Conference-Weeds*, pages 371–380, 1997.

[14] D Nuyttens, WA Taylor, M De Schampheleire, P Verboven, and D Dekeyser. Influence of nozzle type and size on drift potential by means of different wind tunnel evaluation methods. *Biosystems engineering*, 103(3):271–280, 2009.

[15] Sofiene Ouled Taleb Salah, Mathieu Massinon, Nicolas De Cock, Bruno Schiffers, and Frédéric Lebeau. Drift potential of tilted shielded rotary atomisers based on wind tunnel measurements. In *67th International Symposium on Crop Protection*, 2015.

[16] HH Boukhalfa, M Massinon, M Belhamra, and F Lebeau. Contribution of spray droplet pinning fragmentation to canopy retention. *Crop Protection*, 56:91–97, 2014.

[17] Mathieu Massinon, Benjamin Dumont, Nicolas De Cock, Sofiene Ouled Taleb Salah, and Frédéric Lebeau. Study of retention variability on an early growth stage herbaceous plant using a 3d virtual spraying model. *Crop Protection*, 78:63–71, 2015.

[18] Nicolas De Cock, Mathieu Massinon, Sofiene OT Salah, and Frédéric Lebeau. Investigation on optimal spray properties for ground based agricultural applications using deposition and retention models. *Biosystems Engineering*, 162:99–111, 2017.

[19] H Elbanna, MII Rashed, and MA Ghazi. Droplets from liquid sheets in an airstream. *Transactions of the ASAE*, 27(3):677–0679, 1984.

[20] Lijun Qi, PCH Miller, and Zetian Fu. The classification of the drift risk of sprays produced by spinning discs based on wind tunnel measurements. *Biosystems engineering*, 100(1):38–43, 2008.

[21] Sofiene Ouled Taleb Salah, Mathieu Massinon, Bruno Schiffers, Frédéric Lebeau, et al. Use of rotary atomiser to optimize retention on barley leaves while reducing driftable droplets. *International Advances in Pesticide Application, Aspects of Applied Biology 122*, 2014.

[22] HE Ozkan, Andre Miralles, Carole Sinfort, Heping Zhu, and RD Fox. Shields to reduce spray drift. *Journal of agricultural engineering research*, 67(4):311–322, 1997.

[23] J Tsay, HE Ozkan, RD Brazee, and RD Fox. Cfd simulation of moving spray shields. *Transactions of the ASAE*, 45(1):21, 2002.

[24] Yu Chen, Heping Zhu, H Erdal Ozkan, Richard C Derksen, and Charles R Krause. Spray drift and off-target loss reductions with a precision air-assisted sprayer. *Transactions of the ASABE*, 56(6):1273–1281, 2013.

[25] AR Frost. Rotary atomization in the ligament formation mode. *Journal of Agricultural Engineering Research*, 26(1):63–78, 1981.

[26] RC Derksen and LE Bode. Droplet size comparisons from rotary atomizers. *Transactions of the ASAE*, 29(5):1204–1207, 1986.

[27] WH Walton and WC Prewett. The production of sprays and mists of uniform drop size by means of spinning disc type sprayers. *Proceedings of the Physical Society. Section B*, 62(6):341, 1949.

[28] LE Bode, BJ Butler, SL Pearson, and LF Bouse. Characteristics of the micromax rotary atomizer. *Transactions of the ASAE*, 26(4):999–1005, 1983.

[29] J Clayton. A new generation hand held spinning disc sprayer: the micron ulva+ for small farmer crop protection. In *Proceedings of the IRCT cotton conference, February 1992, NDjamena, Chad*, 1992.

[30] JS Clayton, TE Bals, and GS Povey. A new generation hand-held ulva sprayer. In *Proceedings of the 2nd International symposium on pesticide application techniques, 22-24 September 1993, Strasbourg, France*, 1993.

[31] JM Holland, PC Jepson, EC Jones, and C Turner. A comparison of spinning disc atomisers and flat fan pressure nozzles in terms of pesticide deposition and biological efficacy within cereal crops. *Crop protection*, 16(2):179–185, 1997.

[32] Emilia Hilz, Arnoldus WP Vermeer, MA Cohen Stuart, and FAM Leermakers. Mechanism of perforation based on spreading properties of emulsified oils. *Atomization and Sprays*, 22(12), 2012.

[33] Robson S Sasaki, Mauri Martins Teixeira, Cleyton Batista Alvarenga, Humberto Santiago, and Christiam FS Maciel. Spectrum of droplets produced by use of adjuvants. *Idesia*, 31(1):27–34, 2013.

[34] Fabiano Griesang, Ricardo Augusto Decaro, Cícero Antônio Mariano dos Santos, Eduardo Souza Santos, Nelson Henrique de Lima Roque, and Marcelo da Costa Ferreira. How much do adjuvant and nozzles models reduce the spraying drift? drift in agricultural spraying. *American Journal of Plant Sciences*, 8(11): 2785, 2017.

[35] Emilia Hilz and Arnoldus WP Vermeer. Spray drift review: The extent to which a formulation can contribute to spray drift reduction. *Crop Protection*, 44:75–83, 2013.

[36] Félix Savart. Mémoire sur la constitution des veines liquides lancées par des orifices circulaires en mince paroi. *Ann. Chim. Phys*, 53(337):1833, 1833.

[37] Félix Savart. Mémoire sur le choc d'une veine liquide lancée contre un plan circulaire. *Ann. chim*, 54(56):1833, 1833.

[38] Christophe Clanet. Les nappes d'eau de félix savart. *Bulletin National de la SFP*, 125:11–15, 2000.

[39] Joseph Antoine Ferdinand Plateau. *Statique expérimentale et théorique des liquides soumis aux seules forces moléculaires*, volume 2. Gauthier-Villars, 1873.

[40] Lord Rayleigh. On the capillary phenomena of jets. In *Proc. R. Soc. London*, volume 29, pages 71–97, 1879.

[41] Christophe Dumouchel. On the experimental investigation on primary atomization of liquid streams. *Experiments in fluids*, 45(3):371–422, 2008.

[42] EJ Watson. The radial spread of a liquid jet over a horizontal plane. *Journal of Fluid Mechanics*, 20(03):481–499, 1964.

[43] Nicolas De Cock, Mathieu Massinon, Sofyen Ouled Taleb Salah, Benoit Mercatoris, Maria Rosaria Vetrano, and Frédéric Lebeau. Dynamics of a thin radial liquid flow. *Fire Safety Journal*, 83:1–6, 2016.

[44] Tomas Bohr, Peter Dimon, and Vakhtang Putkaradze. Shallow-water approach to the circular hydraulic jump. *Journal of Fluid Mechanics*, 254:635–648, 1993.

[45] Alexis Duchesne, Luc Lebon, and Laurent Limat. Constant froude number in a circular hydraulic jump and its implication on the jump radius selection. *EPL (Europhysics Letters)*, 107(5):54002, 2014.

[46] Christophe Clanet. Dynamics and stability of water bells. *Journal of Fluid Mechanics*, 430:111–147, 2001.

[47] Geoffrey Taylor. The dynamics of thin sheets of fluid. iii. disintegration of fluid sheets. In *Proceedings of the Royal Society of London A: Mathematical, Physical and Engineering Sciences*, volume 253, pages 313–321. The Royal Society, 1959.

[48] Geoffrey Taylor. The dynamics of thin sheets of fluid. ii. waves on fluid sheets. *Proceedings of the Royal Society of London. Series A, Mathematical and Physical Sciences*, pages 296–312, 1959.

[49] Nicolas De Cock, Mathieu Massinon, David Nuyttens, Donald Dekeyser, and Frédéric Lebeau. Measurements of reference iso nozzles by high-speed imaging. *Crop Protection*, 89:105–115, 2016.

[50] Tsuneo Azuma and Tatsuroh Hoshino. The radial flow of a thin liquid film: 2nd report, liquid film thickness. *Bulletin of JSME*, 27(234):2747–2754, 1984.

[51] G Thunivumani and Hrishikesh Gadgil. Dynamics of liquid sheet breakup in splash plate atomization. *Journal of Fluids Engineering*, 140(1):011205, 2018.

[52] Jens Eggers and Emmanuel Villermaux. Physics of liquid jets. *Reports on Progress in Physics*, 71(3):036601.

[53] Jens Eggers and Emmanuel Villermaux. Physics of liquid jets. *Reports on progress in physics*, 71(3):036601, 2008.

[54] Kuide Qin, Holger Tank, SA Wilson, Brandon Downer, and Lei Liu. Controlling droplet-size distribution using oil emulsions in agricultural sprays. *Atomization and Sprays*, 20(3), 2010.

[55] Vance Bergeron. Designing intelligent fluids for controlling spray applications. *Comptes Rendus Physique*, 4(2):211–219, 2003.

[56] Aleksey Rozhkov, Bernard Prunet-Foch, and Michèle Vignes-Adler. Dynamics and disintegration of drops of polymeric liquids. *Journal of non-newtonian fluid mechanics*, 134(1-3):44–55, 2006.

[57] Clara Vernay. *Destabilization of liquid sheets of dilute emulsions*. PhD thesis, Université de Montpellier, 2015.

[58] Jeffery C Thompson and Jonathan P Rothstein. The atomization of viscoelastic fluids in flat-fan and hollow-cone spray nozzles. *Journal of Non-Newtonian Fluid Mechanics*, 147(1-2):11–22, 2007.

[59] Étienne Reyssat, Frédéric Chevy, A-L Biance, Laurence Petitjean, and David Quéré. Shape and instability of free-falling liquid globules. *EPL (Europhysics Letters)*, 80 (3):34005, 2007.